MEASUREMENT OF THE RADIATIVE DECAY WIDTHS OF THE A_2^+ AND $K^{*+}(1430)$ MESONS

by

Selçuk Cihangir

Submitted in Partial Fulfillment

of the

Requirements for the Degree

DOCTOR OF PHILOSOPHY

Department of Physics and Astronomy

The University of Rochester

Rochester, New York.

1981

AAB-5144

VITAE

The author was born in Ankara, Turkey on January 27,1951. He was awarded the fellowship of The Scientific and Technical Research Council of Turkey during his high school and college education. He graduated with high honor from the Middle East Technical University, Ankara on June 1974. The author entered the University of Rochester in September 1975 for graduate study. During this study, the author has received teaching and research assistantship from the Department of Physics and Astronomy of the same university. The work presented in this thesis was carried out under the supervision of Professor Frederick Lobkowicz.

ACKNOWLEDGMENTS

The experiment reported in this thesis was supported in part by the National Science Foundation and the Department of Energy. It was performed with the collaboration of David Berg, Clark Chandlee, Tom Ferbel, Joey Huston, Terry Jensen, Fred Lobkowicz, Mike McLaughlin, Takayoshi Ohshima, Paul Slattery and Pat Thompson from the University of Rochester; Bruce Collick, Steve Heppelmann, Terry Joyce, Marvin Marshak, Earl Peterson, Keith Ruddick and Mike Shupe from the University of Minnesota; Joe Biel, Tom Droege, Alan Jonckheere, Peter Koehler and Charles Nelson from Fermilab.

I am sincerely grateful to Professor Fred Lobkowicz for his support and invaluable supervision throughout my graduate study. He also patiently read the manuscript of the thesis correcting both grammar and physics.

I thankfully acknowledge the assistance of Professors Tom Ferbel, Paul Slattery, Keith Ruddick, Marvin Marshak and Earl Peterson during the experimental run and data analysis.

I extend my special thanks to Doctors Terry Jensen, Charles Nelson, Takayoshi Ohshima, Pat Thompson, Alan Jonckheere and Peter Koehler for their numerous contributions and concerned attentions to the experiment.

It was great pleasure to work with my fellow graduate students David Berg, Clark Chandlee, Joey Huston, Mike McLaughlin, Bruce Collick and Steve Heppelmann.

I thank the staff members of the University of Rochester and Mrs. Betty Cook for the education, advice and guidance they have given to me during my studies.

I acknowledge the professional job done by Mr. John Sheedy in inking the figures for this thesis.

I thank my friend Dan Schaeffer for reading and correcting the English of the manuscript of this thesis.

My stay at Rochester has been made more pleasurable by the Charles family. I will treasure the friendship and memory of Gene, Jeanne, Nick and Callie Charles throughout my life.

Finally, I express my sincere thanks to my parents Nezihe and Adnan Cihangir, to my brother Serdar, my sisters Asuman, Handan and Arzu for their support, love and care which made this all possible.

ABSTRACT

We have investigated for the first time the coherent productions of the A_2^+ and $K^{*+}(1430)$ mesons in the nuclear Coulomb field of Pb and Cu. The experiment was performed at Fermilab using a high resolution forward spectrometer consisting of proportional and drift chambers plus a liquid argon photon calorimeter. The incident momentum was 200 Gev/c. We found that at this momentum strong production mechanisms give very small contributions. The data were analyzed allowing for a small amount of hadronic background to interfere with the dominant electromagnetic production of the A_2^+ and $K^{*+}(1430)$ mesons. The results were used to extract values for the radiative decay widths of these mesons.

TABLE OF CONTENT

	page
VITAE	ii
ACKNOWLEDGMENTS	iii
ABSTRACT	v
TABLE OF CONTENT	vi
LIST OF TABLES	viii
LIST OF FIGURES	ix
CHAPTER	
I. INTRODUCTION AND THEORY	1
A. Coherent Nuclear Processes	5
B. Coulomb Production	11
C. Hadronic Contribution	13
D. Theoretical Coherent Cross Section	15
II. EXPERIMENT AND EQUIPMENT	18
A. Purpose of the Experiment	18
B. The Beam	21
C. The Targets	32
D. Particle Detection	34
1) The Chambers	34
2) The Liquid Argon Calorimeter	38
E. The Magnet	47
F. The Experimental Trigger	47

G. On-Line Data Acquisition and Monitoring 59

III. DATA PROCESSING 62

A. Calibration and Alignment 62

1) Drift Chamber Calibration and Alignment 62

2) LAC Calibration and Alignment 68

B. Data Reconstruction 79

1) Charged tarck Reconstruction 79

2) Photon Reconstruction 83

C. Run to Run Consistency 85

IV. RESOLUTION AND MONTE CARLO MODEL 88

A. Monte Carlo Model 88

B. Spectrometer Resolution 91

1) K^+ Decays 91

2) Monte Carlo Comparisons 92

V. DATA NORMALIZATION 106

A. Corrections to Data 107

1) Spectrometer Related Corrections 108

2) Beam Related Corrections 109

3) Other Corrections 111

B. Normalization 112

VI. A_2^+ AND $K^{*+}(1430)$ DATA 116

A. A_2^+ Data 118

B. $K^{*+}(1430)$ Data 134

C. Mass Spectra 143

D. Fits to t-Distributions 153

E. Conclusions 166

REFERENCES 169

LIST OF TABLES

Table		page
I	Properties of the Targets	33
IIa	Spectrometer Related Corrections	114
IIb	Target Related Corrections	114
IIc	Beam Correction Factors	115
III	$K^{\pm}$-Decay Normalization Factors	115
IVa	Correction Factors for Process $\pi^+ A \rightarrow A \pi^+ \eta$	154
IVb	Correction Factors for Process $\pi^+ A \rightarrow A K^+ K^0_S$	155
IVc	Correction Factors for Process $K^+ A \rightarrow A K^+ \pi^0$	156
IVd	Correction Factors for Process $K^+ A \rightarrow A K^0_S \pi^+$	157
Va	Results of Parameterization of A_2^+ Data	164
Vb	Results of Parameterization of $K^{*+}(1430)$ Data	164

LIST OF FIGURES

1. a) Diagram for the photoproduction of a vector or a tensor meson from a nuclear target.

b) Diagram for the Primakoff production of a vector or a tensor meson in the Coulomb field off a nucleus of charge Z. (Page 4)

2. Diagram illustrating the kinematics for the coherent reaction $a + A \rightarrow A + a^*$. (Page 6).

3. a) Diagram for the Coulomb production reaction $\pi^+ A \rightarrow A\ A_2^+$ (or $K^+ A \rightarrow A\ K^{*+}(1430)$) in the rest frame of A_2^+ (or $K^{*+}(1430)$) (Gottfried-Jackson frame).

b) Gottfried-Jackson reference frame for the coherent process $\pi^+ A \rightarrow A\ A_2^+$ (or $K^+ A \rightarrow A\ K^{*+}(1430)$).

c) Helicity frame for the coherent process $\pi^+ A \rightarrow A\ A_2^+$ (or $K^+ A \rightarrow A\ K^{*+}(1430)$). (Page 10).

4. Schematic diagram of the spectrometer. (Page 19)

5. Schematic diagram of the beam transport system for the M-1 beam-line with ray traces of selected beam particles. The elements Q_i are quadrapole magnets, B_i are bending magnets. (Page 23).

6. Fractions of beam particles as a function of beryllium absorber length. (Page 26).

7. Fractions of beam particles as a function of production transverse momentum with no beryllium and with 2.2 m beryllium. (Page 27).

8. Pressure curve for the Cerenkov counter K1. (Page 29).

9. Pressure curve for the Cerenkov counter K2. (Page 30).

10. Pressure curve for the Cerenkov counter K3. (Page 31).

11. Drift chamber read-out and calibration system. (Page 37).

12. Schematic diagram for the assembly of the liquid argon detector. (Page 40).

13. Schematic top and side views of the liquid argon detector and cryostat assembly. (Page 41).

14. a) Block diagram of the electronics for one channel of the LAC.

b) Signal at point (a) of the above diagram.

c) Read-out system for the LAC amplifiers. (Page 44).

15. Schematic of the arrangement of scintillation counters used in the experiment. (Page 49).

16. Diagram of the Logic used to define the RHO, VEE and A1 triggers. (Page 50).

17. Diagram of the LAC Logic. (Page 57).

18. Schematic diagram of the on-line data acquisition system. (Page 60).

19. Plots of the calibration constants for two LRS 2770A TDC channels as a function of time. (Page 64).

20. Plots of TDC time versus projected beam position for upstream and downstream chambers. (Page 67).

21. Energy conversion factors for all strips in the front half of the LAC. (Page 72).

22. a) Energy measured by the LAC versus momentum measured by the drift chambers and the analyzing magnet for electrons from Ke3 decay process.

b) Energy resolution of the LAC (standart deviation squared) as a function of electron momentum. (Page 74).

23. a) Histogram of the difference between the X position of the electron measured by the LAC and the drift chambers for electrons from Ke3 decays.

b) Distribution of two photon mass for $K^+ \rightarrow \pi^+\pi^0$ decay events. (Page 75).

24. Electromagnetic and hadronic shower shapes of the LAC. (Page 77).

25. a) Plot of the fraction of hadrons versus the ratio of energy measured by the LAC to momentum measured by the drift chambers and the analyzing magnet of hadrons.

b) Plot of the fraction of electrons and hadrons versus the ratio of energy at the back of the LAC to total LAC energy for electrons and hadrons. (Page 78).

26. Distribution of the difference between the X position of hadron measured by the LAC and the drift chambers. (Page 80).

27. Average value of the reconstructed two photon mass of π^0's from $K^+ \rightarrow \pi^+\pi^0$ decays as a function of time. (Page 87).

28. a) Decay vertex distribution and Monte Carlo model prediction for $K^+ \rightarrow \pi^+\pi^0$ decay events.

b) Decay vertex distribution and Monte Carlo model prediction for $K^+ \rightarrow \pi^+\pi^+\pi^-$ decay events. (Page 93).

29. a) Distribution and Monte Carlo model prediction of the total energy of $\pi^+\pi^0$ system from $K^+ \rightarrow \pi^+\pi^0$ decays. The events in the shaded region are removed by a $\pi^+\pi^0$ mass cut between 0.46 - 0.54 Mev/c^2.

b) Distribution and Monte Carlo model prediction of the total energy of $\pi^+\pi^+\pi^-$ system from $K^+ \rightarrow \pi^+\pi^+\pi^-$ decays. The events in the shaded region are removed by a $\pi^+\pi^+\pi^-$ mass cut between 0.46 - 0.54 Mev/c^2. (Page 94)

30. Distribution and Monte Carlo model prediction of two photon (π^0) mass for $K^+ \rightarrow \pi^+\pi^0$ decays. (Page 96).

31. a) Distribution and Monte Carlo model prediction of $\pi^+\pi^0$ mass for $K^+ \rightarrow \pi^+\pi^0$ decays.

b) Distribution and Monte Carlo model prediction of $\pi^+\pi^+\pi^-$ mass for $K^+ \rightarrow \pi^+\pi^+\pi^-$ decays. (Page 97).

32. a) Distribution and Monte Carlo model prediction of the square of the transverse distance of the π^+ from beam center for $K^+ \rightarrow \pi^+\pi^0$ decays.

b) Decay angle distribution and Monte Carlo model prediction in the helicity frame for $K^+ \rightarrow \pi^+\pi^0$ decays. (Page 99).

33. a) Dalitz plot of real $K^+ \rightarrow \pi^+\pi^+\pi^-$ decay events. "Pion 3" is π^- and "Pion 2" is the lower energy π^+.

b) Dalitz plot of Monte Carlo $K^+ \rightarrow \pi^+\pi^+\pi^-$ decay events. "Pion 3" is π^- and "Pion 2" is the lower energy π^+. (Page 100).

34. a) Distribution and Monte Carlo prediction of the energy asymmetry for the two photons from π^0 decays resulting from $K^+ \to \pi^+\pi^0$ decays.

b) Distribution and Monte Carlo prediction of the separation between the π^+ and the nearest photon, calculated at the position of the LAC for $K^+ \to \pi^+\pi^0$ decays. (Page 102).

35. t-distribution for $K^+ \to \pi^+\pi^0$ events accumulated with copper, lead targets and with no target in place (MT). The solid curves are Monte Carlo model predictions. (Page 104).

36. t-distribution for $K^+ \to \pi^+\pi^+\pi^-$ events accumulated with copper, lead targets and with no target in place (MT). The solid curves are Monte Carlo model predictions. (Page 105).

37. $\pi^+\eta$ mass distibutions for the coherent processes $\pi^+ A \to A\pi^+\eta$ ($\eta \to \gamma\gamma$) for lead and copper targets. (Page 119).

38. $\pi^+\eta$ energy distibutions for the coherent processes $\pi^+ A \to A\pi^+\eta$ ($\eta \to \gamma\gamma$) for lead and copper targets. (Page 120).

39. a) Interaction vertex distribution and Monte Carlo model prediction of the coherent process $\pi^+ Pb \to Pb\pi^+\eta$ ($\eta \to \gamma\gamma$).

b) Decay angle distribution and Monte Carlo model prediction in the Gottfried-Jackson frame of the

coherent process $\pi^+ Pb \rightarrow Pb\pi^+\eta$ ($\eta \rightarrow \gamma\gamma$). (Page 122).

40. Distribution and Monte Carlo prediction of two photon mass resulting from η decay of the coherent process $\pi^+ Pb \rightarrow Pb\pi^+\eta$ ($\eta \rightarrow \gamma\gamma$). For comparison, same distribution is shown for the process $\pi^+Pb \rightarrow Pb\pi^+\pi^0$. (Page 123).

41. a) $\pi^+\eta$ mass distibutions for the coherent processes $\pi^+A \rightarrow A\pi^+\eta$ ($\eta \rightarrow \pi^+\pi^-\pi^0$) for lead and copper targets.

b) $\pi^+\eta$ energy distibutions for the coherent processes $\pi^+A \rightarrow A\pi^+\eta$ ($\eta \rightarrow \pi^+\pi^-\pi^0$) for lead and copper targets. (Page 125).

42. a) Interaction vertex distribution and Monte Carlo model prediction of the coherent process $\pi^+A \rightarrow A\pi^+\eta$ ($\eta \rightarrow \pi^+\pi^-\pi^0$) for lead and copper targets.

b) Decay angle distribution and Monte Carlo model prediction in the Gottfried-Jackson frame of the coherent process $\pi^+A \rightarrow A\pi^+\eta$ ($\eta \rightarrow \pi^+\pi^-\pi^0$) for lead and copper targets.

c) Distribution and Monte Carlo prediction of two photon mass resulting from π^0 decay of the coherent process $\pi^+A \rightarrow A\pi^+\eta$ ($\eta \rightarrow \pi^+\pi^-\pi^0$) for lead and copper targets. (Page 126).

43. Distribution and Monte Carlo prediction of $\pi^+\pi^-\pi^0$ mass for the coherent process $\pi^+A \rightarrow A\pi^+\pi^+\pi^-\pi^0$ with lead and copper targets. (Page 127).

44. $K^+K_s^0$ mass distibutions for the coherent processes $\pi^+A \rightarrow A\ K^+K_s^0$ ($K_s^0 \rightarrow \pi^+\pi^-$) for lead and copper targets. (Page 129).

45. $K^+K_s^0$ energy distibutions for the coherent processes $\pi^+A \rightarrow A\ K^+K_s^0$ ($K_s^0 \rightarrow \pi^+\pi^-$) for lead and copper targets. (Page 130).

46. a) Interaction vertex distribution and Monte Carlo model prediction of the coherent process $\pi^+Pb \rightarrow Pb\ K^+K_s^0$ ($K_s^0 \rightarrow \pi^+\pi^-$).

b) Decay angle distribution and Monte Carlo model prediction in the Gottfried-Jackson frame of the coherent process $\pi^+Pb \rightarrow Pb\ K^+K_s^0$ ($K_s^0 \rightarrow \pi^+\pi^-$).

c) Distribution and Monte Carlo prediction of two pion mass resulting from K_s^0 decay of the coherent process $\pi^+Pb \rightarrow Pb\ K^+K_s^0$ ($K_s^0 \rightarrow \pi^+\pi^-$). (Page 132).

47. $K^+\pi^0$ mass distibutions for the coherent processes $K^+A \rightarrow A\ K^+\pi^0$ ($\pi^0 \rightarrow \gamma\gamma$) for lead and copper targets. (Page 135).

48. a,b) $K^+\pi^0$ energy distibutions for the coherent processes $K^+A \rightarrow A\ K^+\pi^0$ ($\pi^0 \rightarrow \gamma\gamma$) for lead and copper targets.

c) Interaction vertex distribution and Monte Carlo model prediction of the coherent process $K^+Pb \rightarrow Pb\ K^+\pi^0$ ($\pi^0 \rightarrow \gamma\gamma$). (Page 136).

49. a) Decay angle distribution and Monte Carlo model prediction in the Gottfried-Jackson frame of the coherent process $K^+Pb \rightarrow Pb\ K^+\pi^0$ ($\pi^0 \rightarrow \gamma\gamma$).

b) Distribution and Monte Carlo prediction of two photon mass resulting from π^0 decay of the coherent process $K^+ Pb \rightarrow Pb\ K^+ \pi^0$ ($\pi^0 \rightarrow \gamma\gamma$). (Page 138).

50. $K_S^0 \pi^+$ mass distibutions for the coherent processes $K^+ A \rightarrow A\ K_S^0 \pi^+ (K_S^0 \rightarrow \pi^+\pi^-)$ for lead and copper targets. (Page 139).

51. a,b) $K_S^0 \pi^+$ energy distibutions for the coherent processes $K^+ A \rightarrow A\ K_S^0 \pi^+$ $(K_S^0 \rightarrow \pi^+\pi^-)$ for lead and copper targets.

c) Interaction vertex distribution and Monte Carlo model prediction of the coherent process $K^+ Pb \rightarrow Pb\ K_S^0 \pi^+$ $(K_S^0 \rightarrow \pi^+\pi^-)$. (Page 140).

52. a) Decay angle distribution and Monte Carlo model prediction in the Gottfried-Jackson frame of the coherent process $K^+ Pb \rightarrow Pb\ K_S^0 \pi^+$ $(K_S^0 \rightarrow \pi^+\pi^-)$.

b) Distribution and Monte Carlo prediction of two pion mass resulting from K_S^0 decay of the coherent process $K^+ Pb \rightarrow Pb\ K_S^0 \pi^+$ $(K_S^0 \rightarrow \pi^+\pi^-)$. (Page 142).

53. Acceptance corrected $\pi^+\eta$ mass spectrum for the precess $\pi^+ A \rightarrow A \pi^+ \eta$ $(\eta \rightarrow \gamma\gamma)$, with lead and copper targets, at small t. The solid curve above the distribution shows the mass acceptance of the apparatus for a $\sin^2\theta \cos^2\theta \sin^2\phi$ decay of A_2^+. The solid curve is fit of the data to the Breit-Wigner shapes described in the text. The dashed line is the backgrond given by the fit. (Page 148).

54. Acceptance corrected $\pi^+\eta$ mass spectrum for the precess $\pi^+A \rightarrow A\pi^+\eta$ ($\eta \rightarrow \pi^+\pi^-\pi^0$), with lead and copper targets, at small t. The solid curve above the distribution shows the mass acceptance of the apparatus for a $\sin^2\theta \cos^2\theta \sin^2\phi$ decay of A_2^+. The solid curve is fit of the data to the Breit-Wigner shapes described in the text. The dashed line is the backgrond given by the fit. (Page 149).

55. Acceptance corrected $K^+K_S^0$ mass spectrum for the precess $\pi^+A \rightarrow A\,K^+K_S^0$ ($K_S^0 \rightarrow \pi^+\pi^-$), with lead and copper targets, at small t. The solid curve above the distribution shows the mass acceptance of the apparatus for a $\sin^2\theta \cos^2\theta \sin^2\phi$ decay of A_2^+. The solid curves are fits of the data to the Breit-Wigner shapes described in the text. The dashed line is the backgrond given by the fit. (Page 150).

56. Acceptance corrected $K^+\pi^0$ mass spectrum for the precess $K^+A \rightarrow A\,K^+\pi^0$ ($\pi^0 \rightarrow \gamma\gamma$), with lead and copper targets, at small t. The solid curve above the distribution shows the mass acceptance of the apparatus for a $\sin^2\theta \cos^2\theta \sin^2\phi$ decay of $K^{*+}(1430)$. The solid curve is fit of the data to the Breit-Wigner shapes described in the text. The dashed line is the backgrond given by the fit. (Page 151).

57. Acceptance corrected $K_S^0\pi^+$ mass spectrum for the precess $K^+A \rightarrow A\,K_S^0\pi^+$ ($K_S^0 \rightarrow \pi^+\pi^-$), with lead and copper

targets, at small t. The solid curve above the distribution shows the mass acceptance of the apparatus for a $\sin^2\theta \cos^2\theta \sin^2\phi$ decay of $K^{*+}(1430)$. The solid curve is fit of the data to the Breit-Wigner shapes described in the text. The dashed line is the backgrond given by the fit. (Page 152).

58. t-distributions for the process $\pi^+ A \rightarrow A \pi^+ \eta$ ($\eta \rightarrow \gamma\gamma$) for lead and copper targets. The dashed lines are fits of the data to the model, including Coulomb and strong production of A_2^+, as described in the text. (Page 160).

59. t-distributions for the process $\pi^+ A \rightarrow A K^+ K_S^0$ for lead and copper targets. The dashed lines are fits of the data to the model, including Coulomb and strong production of A_2^+, as described in the text. (Page 161).

60. t-distributions for the process $K^+ A \rightarrow A K^+ \pi^0$ ($\pi^0 \rightarrow \gamma\gamma$) for lead and copper targets. The dashed lines are fits of the data to the model, including Coulomb and strong production of $K^{*+}(1430)$, as described in the text. (Page 162).

61. t-distributions for the process $K^+ A \rightarrow A K_S^0 \pi^+$ ($K_S^0 \rightarrow \pi^+\pi^-$) for lead and copper targets. The dashed lines are fits of the data to the model, including Coulomb and strong production of $K^{*+}(1430)$, as described in the text. (Page 163).

CHAPTER I

INTRODUCTION AND THEORY

Electromagnetic interactions have been and are powerfull tools for studying the structure of hadrons since they probe the hadronic characteristics, but do not determine them. In addition, the photon is the best understood elementary particle and this makes it easier to implement experimental techniques in reactions involving photons.

One such interaction is the radiative decay process of mesons. Any theory that describes the hadrons as composed of point like constituents should be able to predict the width for this process as does the quark model[1]. The predictions for the radiative decay of vector mesons (L=0, S=1) to pseudoscaler mesons (L=0, S=0) and a photon[2][3], $V \rightarrow P\gamma$, have been a main source of difficulty for the model based on single quark transition[4]. New measurements on the radiative decays of ρ^- and $K^{*-}(890)$ improved the situation considerably[5].

There have been attempts to predict the same decay widths, along with the strong decay widths, for tensor mesons (L=1, S=1, $J^P=2^+$) by combining the single quark

transition and vector dominance assumptions[6]. In particular, using the decay width value $\Gamma(A_2 \to \rho\pi) = 72$ Mev as input, the partial widths $\Gamma(A_2 \to \pi\gamma)$ and $\Gamma(K^*(1430) \to K\gamma)$ have been predicted to be 348 Kev and 312 Kev, respectively[7].

These mesons tend to have large hadronic widths, therefore their electromagnetic branching ratios are small. There are certain experiments sensitive to the electromagnetic processes. One of them is the coherent exitation of pions and kaons into vector and tensor mesons in the Coulomb field of a nucleus[8], that is, the Primakoff effect. This thesis reports the first measurements of the radiative decay widths of $A_2^+(1310)$ and $K^{*+}(1430)$ via this effect, specifically through the reactions

$$\pi^+ A \to A\, A_2^+(1310) \qquad (1)$$

followed by

$$A_2^+(1310) \to \pi^+\eta \quad \text{or} \quad K^+K_s^0$$

and

$$K^+A \to A\, K^{*+}(1430) \qquad (2)$$

followed by

$$K^{*+}(1430) \to K^+\pi^0 \quad \text{or} \quad K_s^0\pi^+$$

where A represents targets of different nuclear charge.

Another way of measuring the radiative decay width $\Gamma(a \to b\gamma)$ is by direct measurement. But this is

feasible only if a sufficiently pure parent sample can be prepared in production experiments, if the branching ratio $\Gamma(a \to b\gamma)/\Gamma(a)$ is not too small and if the decay $a \to b\pi^0$ (or $b\eta$) is forbidden. Since separating radiative decays from background events with π^0 (or η) decaying into two photons is experimentally very difficult, only the widths of ω and ϕ mesons have been measured in this direct way.

A third way is the photoproduction of the vector and tensor mesons through the exchange of a virtual pseudoscaler meson between a nuclear target and an incident photon, as shown in Figure 1a. However, various hadronic exchange processes can contribute to this production process considerably and the extraction of the radiative decay width from the measurements becomes model dependent.

The coherent Primakoff (or Coulomb) production, as shown in Figure 1b, of the vector and the tensor mesons is by far the best method of studying the radiative decay widths of these mesons. The theoretical basis to describe this production mechanism is discussed in this chapter. Section A is devoted to the characteristics of coherent productions on nuclear targets. In Section B, the Primakoff process is outlined and the hadronic (strong) background to this process is discussed in Section C.

a) Photoproduction

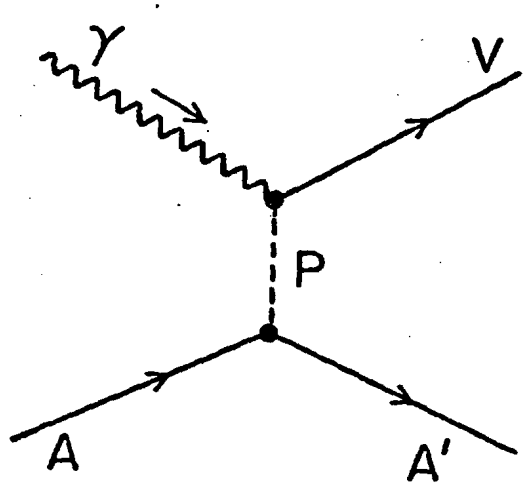

b) Primakoff effect

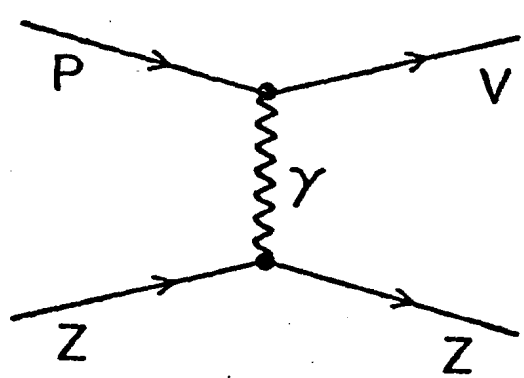

Figure 1

The experimental apparatus is explained in Chapter II. The calibration of the different components of the experiment and the data processing are presented in Chapter III. In Chapter IV, the resolution of the experiment and its Monte Carlo model are explained. The normalization of the cross sections is described in Chapter V, and in Chapter VI the analysis of the data for the reactions above and the extraction of $\Gamma(A_2^+ \to \pi^+\gamma)$ and $\Gamma(K^{*+}(1430) \to K^+\gamma)$ values are presented.

A. COHERENT NUCLEAR PROCESSES

A process like

$$a + A \to a^* + A$$

where A represents a nucleus with atomic number A, is called coherent if the nucleus stays in its ground state or in some well defined, low-lying exited state after the interaction[9][10]. The production amplitude is then the coherent superposition of the amplitudes from individual nucleons. Due to this superposition, the total yield of coherent processes is enhanced.

The kinematics of such a process is illustrated in Figure 2. Defining the invariant four-momentum transfer square as $-t=q^2=(p_{a'}-p_a)^2=(p_A'-p_A)^2$, one obtains the exact relations

a) Laboratory System

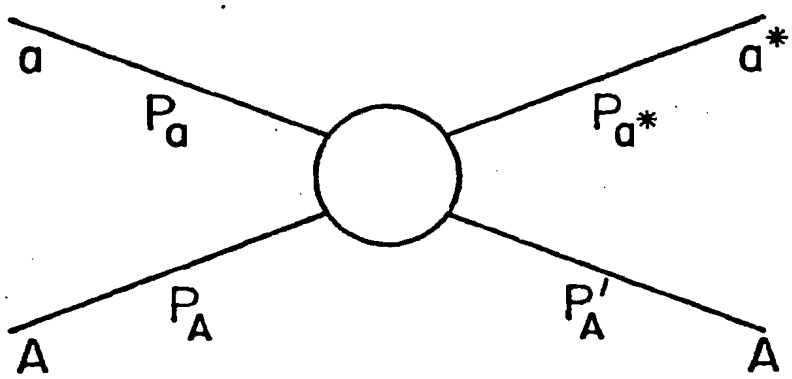

$P_a = (\vec{P}_a, E_a)$ $\qquad$ $P_A = (\vec{0}, M_A)$

$P_{a^*} = (\vec{P}_{a^*}, E_{a^*})$ $\qquad$ $P_A' = (\vec{q}, E_A)$

$$q = (\vec{q}, E_A - M_A)$$

b)

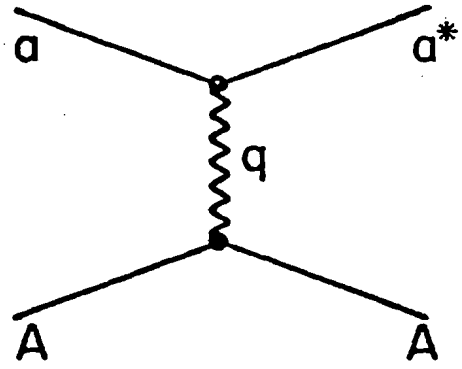

Figure 2

$$q_0 = E_A - M_A = \vec{q}^{\,2}/2M_A$$
$$q_z = \frac{m_{a^*}^2 - m_a^2 + \vec{q}^{\,2}(1 + E_A/M_A)}{2|\vec{P}_a|} \qquad (3)$$

where $q_0 = E_A - M_A$, the kinetic energy of the recoiling nucleus and $\vec{q} = \vec{q}_z + \vec{q}_T$ with q_z and q_T being the components of the three-vector momentum transfer in parallel and perpendicular to the beam direction, respectively. If the coherence takes place within the nuclear radius $R=1.12A^{1/3}$ fm, the uncertainty principle yields an order of magnitute estimate $|\vec{q}| \lesssim \hbar/1.12A^{1/3} = 0.2/A^{1/3}$ Gev/c, which is ~0.035 Gev/c for a lead target. It follows from Equation (3) that q_0 is of the order of couple of Kev and $q_z \simeq (m_{a^*}^2 - m_a^2)/2|\vec{P}_a|$ =constant.

On the other hand, the minimum possible four momentum transfer occurs for production at 0°, where $q_T=0$ and therefore it is defined that

$$q_z \simeq \frac{m_{a^*}^2 - m_a^2}{2|\vec{P}_a|} = q_{min} \qquad \text{(minimum possible q)}$$

This quantity is almost equal to 5 Mev/c for A_2^+ and $K^{*+}(1430)$ production by 200 Gev/c incoming π^+ and K^+. From the above equation it follows that

$$-t_{min} = q_{min}^2 = \frac{(m_{a^*}^2 - m_a^2)^2}{4|\vec{P}_a|^2}$$

$$t = q_{min}^2 + q_T^2$$

Some selection rules apply to the processes that take place on a nucleus target coherently if the nucleus is to remain in its ground state. This can be used to suppress some of the exchange mechanisms and that is why nuclear targets are preferable to hydrogen targets for special purposes.

For instance, for pion and kaon ($J^P=0^-$) induced coherent reactions on a spin zero nucleus, parity and angular momentum conservation require that in the forward direction only states with $J^P=0^-$, 1^+, 2^-, ... can be produced since the production amplitude has parity of $P=(-1)^J$ and thus $P_{0+}=(-1)^J P_0$ [11]. This process is called "diffraction dissociation" and can be considered to be taking place via "vacuum" or "Pomeron" exchange. Away from the forward direction, additional amplitude with opposite parity can contribute and the states $J^P=1^-$, 2^+, 3^-, ... can be produced as well. (0^+ is forbidden at all angles because $0^- \rightarrow 0^+$ implies no spin exchange but parity exchange, i.e exchange of a pseudoscaler particle. But the absorption of a pseudoscaler by a nucleon must imply spin flip and so the final nuclear state must be different from the initial one). For small t ($t<0.002$), the contribution from this opposite parity term is small in comparison to other and hence the latter states are less abundant since usually an extra factor t is involved.

For a nucleus with isospin I=0 additional restrictions apply. The cross section is proportional to (N+Z) for I=0 exchange and to (N-Z) for I=1 exchange (N=nucleon number, Z=proton number of the target nucleus). If isospin of the target is zero, which implies that N=Z, then I=1 exchange is strictly forbidden. Photon exchange therefore contributes with its I=0 component only, ω-exchange (I=0) mechanism dominates the A_2-exchange (I=1) mechanism, and the isospin change in the process is zero. However, A_2-exchange contribution can become appreciable compared to the ω-exchange for heavy nuclei since there the neutron and proton numbers are not the same and in the coherent sum of these nucleons the isospins do not cancel each other totally. But, this I=1 exchange is still greatly suppressed because the cross section is proportional to N-Z=A-2Z which is much less than A=N+Z, to which the I=0 exchange cross section is proportional. Consequently, the $J^P=2^+$ particles A_2^+ and $K^{*+}(1430)$ can be produced coherently on a nucleus target via photon exchange (Coulomb production) or ω and A_2-exchange (strong production) from a pion and a kaon, respectively.

The Reactions (1) and (2) are shown in Figure 3a as they are seen in the rest frame of the produced $J^P=2^+$ particles, A_2^+ and $K^{*+}(1430)$. Only the photons with helicity states +/- 1, but not 0 (approximately), can contribute to these

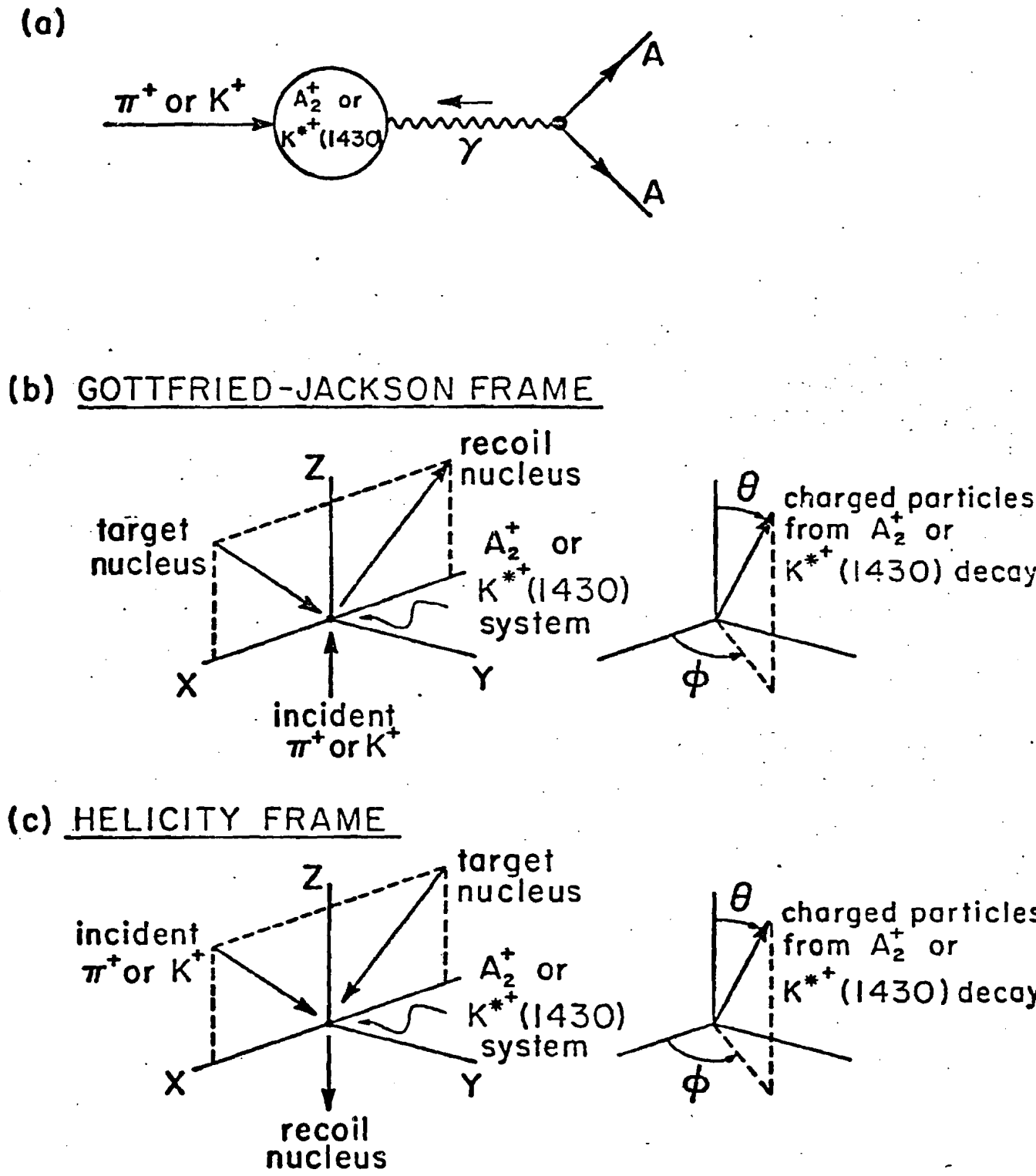
(a)
π+ or K+
A2+ or
K*+(1430)
γ
A
A
(b) GOTTFRIED-JACKSON FRAME
Z
recoil
nucleus
target
nucleus
A2+ or
K*+(1430)
system
X
Y
incident
π+ or K+
θ
charged particles
from A2+ or
K*+(1430) decay
φ
(c) HELICITY FRAME
Z
target
nucleus
incident
π+ or K+
A2+ or
K*+(1430)
system
X
Y
recoil
nucleus
θ
charged particles
from A2+ or
K*+(1430) decay
φ

Figure 3

reactions[12]. The incident particle can be regarded as a plane wave and be represented by spherical harmonic wave functions Y_L^0 , L in +/-1 unit of $\hbar$ and $L_z=0$. Then, the produced particle should have $L_z=1$ in the same or opposite direction as the spin of the incident photon in the Gottfried-Jackson frame (Figure 3b). Therefore the angular distribution of the charged particle produced by the decays of A_2^+ and $K^{*+}(1430)$ should have an angular distribution of $|Y_2^1(\theta,\phi)+Y_2^{-1}(\theta,\phi)|^2 \sim \sin^2\theta.\cos^2\theta.\sin^2\phi$. In Figure 3c we show the s-channel helicity frame that can also be used to describe particle decays. These two reference frames are nearly the same for high energy Coulomb production because of the small angles involved in the production process.

B. COULOMB PRODUCTION

Primakoff first suggested that the electromagnetic field of a nucleus could be used to produce and measure the life-time of the π^0 meson[13]. This method was extended to investigate the radiative decay widths of vector and tensor mesons by various authors[8].

The derivation of the formula for cross section to the Reactions (1) or (2) is discussed in the literature[14]. It can be written as

$$\frac{d\sigma_c}{dt}=|T_c|^2=8\pi\alpha Z^2\frac{(2S_{a^*}+1)}{(2S_a+1)}\Gamma(a^*\to a\gamma)\left(\frac{M_{a^*}}{M_{a^*}^2-M_a^2}\right)^3\frac{t-t_{min}}{t^2}|F_{EM}(t)|^2 \quad (4)$$

where α is the fine structure constant, Z is the atomic number of the nuclear target, S_{a^*} and S_a are the spins, M_{a^*} and M_a are the masses of produced and incoming particles, respectively, $\Gamma(a^* \to a\gamma)$ is the radiative decay width of particle a^*, t is the four-momentum transfer and $F_{EM}(t)$ is the nuclear form factor,

$$F_{EM}(q) = \int d^3\vec{r}\, \exp(i\vec{q}.\vec{r})\, \rho(r)$$

with $\rho(r)$ being the nuclear charge density.

Some characteristics of the production mechanism are noted from Equation (4) as follows:

1) The cross section vanishes at $t=t_{min}$ ($\theta = 0^\circ$); but reaches its maximum at $t=2t_{min}$, and then falls as 1/t.

2) The peak position is almost independent of the target nucleus, however it becomes smaller for higher values of incoming particle momentum, $|\vec{P}_a|$.

3) The height of the peak is proportional to $Z^2 |\vec{P}_a|^2$. The Z^2 dependence of the cross section makes the use of a heavy nucleus preferable to lighter ones, since the hadronic exchange mechanisms have contributions proportional to some power of A less than 1.5 (see the next section).

4) The integrated cross section increases as

$Z^2 \log(|\vec{P}_a|)$. Since the pomeron exchange stays roughly constant and ω-exchange decrease as $1/|\vec{P}_a|$ [15], the Coulomb production dominates the other coherent processes for higher incoming momenta, especially in the small t region. Even for pomeron exchange, the fraction under the Primakoff peak decreases with incoming momenta, because the t-distribution for the Primakoff effect becomes sharper.

C. HADRONIC CONTRIBUTION

The hadronic contribution to the $J^P=2^+$ meson production is dominated by ω-exchange, as discussed earlier. The cross section for it can be written as[16]

$$\frac{d\sigma_s}{dt} = |T_s|^2 = A^2 C_s (t-t_{min}) |F_H(t)|^2 \qquad (5)$$

where A is the atomic weight number of the nuclear target, C_s is the energy dependent normalization factor for the production and $F_H(t)$ is the absorption corrected hadronic form factor of the nucleus. Unlike the case of Coulomb production, the form factor $F_H(t)$ affects, due to absorption, the total cross section and yields a total cross section proportional to A. In the forward direction, the square of the form factor behaves like $\exp(-R^2 t/4)$ with R being the nuclear radius, therefore the cross section peaks

at $t \sim 4/R^2$. This value is almost independent of energy, therefore it is easier to separate the hadronic contribution from the Coulombic one at higher values of incoming energy. On the other hand, the integrated cross section falls with energy as $1/|\vec{P}_a|$ and consequently, it is more advantagous to study the Coulomb production at high energies.

In Equation (5), C_s is taken to be A-independent. This is equivalent to the assumption that the hadronic production is dominated by ω-exchange (see Section A) and A_2-exchange can be neglected. This is certainly true for a nucleus with equal numbers of protons and neutrons (I=0). It was suggested[17] that for heavy nucleus with non-vanishing (Z-N), C_s in Equation (5) should be replaced by

$$C_s(Z, N) = C_s(Z=N) \left| 1 - \delta (Z-N)/A \right|^2$$

where δ measured the amount of interference, and (Z-N) dependence was due to the A_2-exchange with I=1, $J^P = 2^+$. Whatever the nucler target is, at an energy of 200 Gev the Coulomb production dominates at small angles, as discussed before, and it is practically impossible to see any I=1 exchange even if it is present.

D. THEORETICAL COHERENT CROSS SECTION

The theoretical differential cross section is written as

$$\frac{d\sigma}{dt} = |T_c + e^{i\phi} T_s|^2 + \frac{d\sigma}{dt}\Big|_{inc} \qquad (6)$$

where $d\sigma/dt(inc)$ is due to incoherent production and ϕ is the relative phase of the Coulomb production and the hadronic production. The incoherent production cross section is small compared to the coherent one. In addition, the trigger of the experiment was arranged to supress events with nuclear excitation. Therefore the incoherent term is not considered in further discussions.

In Equation (6), writing

$$T_c = [\Gamma(a^* \rightarrow a\gamma)]^{1/2} f_c(t)$$

$$T_s = C_s^{1/2} f_s(t)$$

yields the expression

$$\frac{d\sigma}{dt} = \Gamma(a^* \rightarrow a\gamma)\,|f_c(t)|^2 + C_s\,|f_s(t)|^2 +$$

$$2\left[\Gamma(a^* \rightarrow a\gamma)\right]^{1/2}\Big[\left\{Re[f_c(t)]\,Re[f_s(t)] + Im[f_c(t)]\,Im[f_s(t)]\right\}\cos\phi$$

$$+ \left\{Im[f_c(t)]\,Re[f_s(t)] - Re[f_c(t)]\,Im[f_s(t)]\right\}\sin\phi\Big] \qquad (7)$$

The terms $f_c(t)$ and $f_s(t)$ account for the nuclear shape and also for the absorption of incoming and outgoing states within the nucleus. Their explicit forms are[18]

$$f_c(t) = \left[8\pi\alpha Z^2 \frac{(2S_{a^*}+1)}{(2S_a+1)} \left(\frac{M_{a^*}}{M_{a^*}^2 - M_a^2}\right)^3\right]^{1/2} \hat{q}_T \cdot \vec{F}_{EM}(t)$$

with $\hat{q}_T = \dfrac{\vec{q}_T}{|\vec{q}_T|}$, $\vec{q}_T^{\,2} = t - t_{min}$

$$\vec{F}_{EM}(t) = \frac{1}{4\pi i} \int d^3r \exp\left[i\vec{q}\cdot\vec{r} + i\chi_c(b)\right] \exp\left[-\sigma' T(b)/2\right] \vec{E}(r)$$

and

$$f_s(t) = A \int d^3r \exp\left[i\vec{q}\cdot\vec{r} + i\chi_c(b)\right] \exp\left[-\sigma' T(b)/2\right] \hat{q}_T \cdot \vec{\nabla} \rho(r)$$

Here, $\vec{E}(r)$ is the electric field of the nucleus, $\sigma' = (1-ix)\sigma$ where σ is the total "a-nucleon" cross section and x is the ratio of the real to imaginary part of the forward scattering amplitude for "a-nucleon" collision, T (b) is the nuclear thickness as a function of impact parameter b and written as

$$T(b) = A\int_{-\infty}^{\infty} dz\, \rho(b,z)$$

with ρ being the nuclear density. σ and x are assumed to be the same for incoming and outgoing states[19]. χ_c is the Coulomb phase created by the distortion of the wave functions of the incoming and outgoing sates by the Coulomb field of the nuclear target, and given by

$$\chi_c(b) = -\frac{Ze^2}{\hbar c} \int_{-\infty}^{\infty} dz\, \psi(b,z)$$

where

$$\psi(\vec{r}) = \int d^3r' \frac{\rho(r')}{|\vec{r}-\vec{r}'|}$$

is the Coulomb potential of the nucleus.

Since the Coulomb production takes place predominantly outside of the nucleus, the form of the nuclear density does not affect the calculations for f_c seriously. Therefore it was assumed that the density distribution was uniform within radius $R=[C^2+\frac{7}{3}(\pi a)]$ where $C=1.12A^{1/2}$ fm and $a=0.545$ fm [20]. These parameters yield the same average radius as the Woods-Saxon distribution,

$$\rho(r) = \frac{\rho_0}{1+\exp\left(\frac{r-C}{a}\right)}$$

Because of the strong absorption inside the nucleus, the outer layer of ~1 fm thick of the nucleus contribute to F_s. Therefore, the Woods-Saxon parametrization above is used to calculate $f_s(t)$.

The data was fit to Equation (7) with the components calculated as explained above. The details of the fitting procedure are presented in Chapter VI.

CHAPTER II

EXPERIMENT AND EQUIPMENT

In this chapter we describe the experiment and its goals, components, construction and implementation. The performance of the equipment is discussed in Chapter IV. A schematic layout of the experiment is shown in Figure 4.

A. PURPOSE OF THE EXPERIMENT

The main objective of the experiment was to extract the radiative decay widths of various vector and tensor mesons by producing them via Primakoff process coherently on nuclear targets. The beam that was used for this purpose is described in Section B. The produced mesons, in particular the tensor mesons A_2^+ and $K^{*+}(1430)$, were studied through their decay modes that contained charged mesons and photons. Specifically, the decays

$$A_2^+ \rightarrow \pi^+ \eta \tag{8}$$

followed by

$$\eta \rightarrow \gamma\gamma \qquad \text{or} \qquad \eta \rightarrow \pi^+ \pi^- \pi^0$$

or

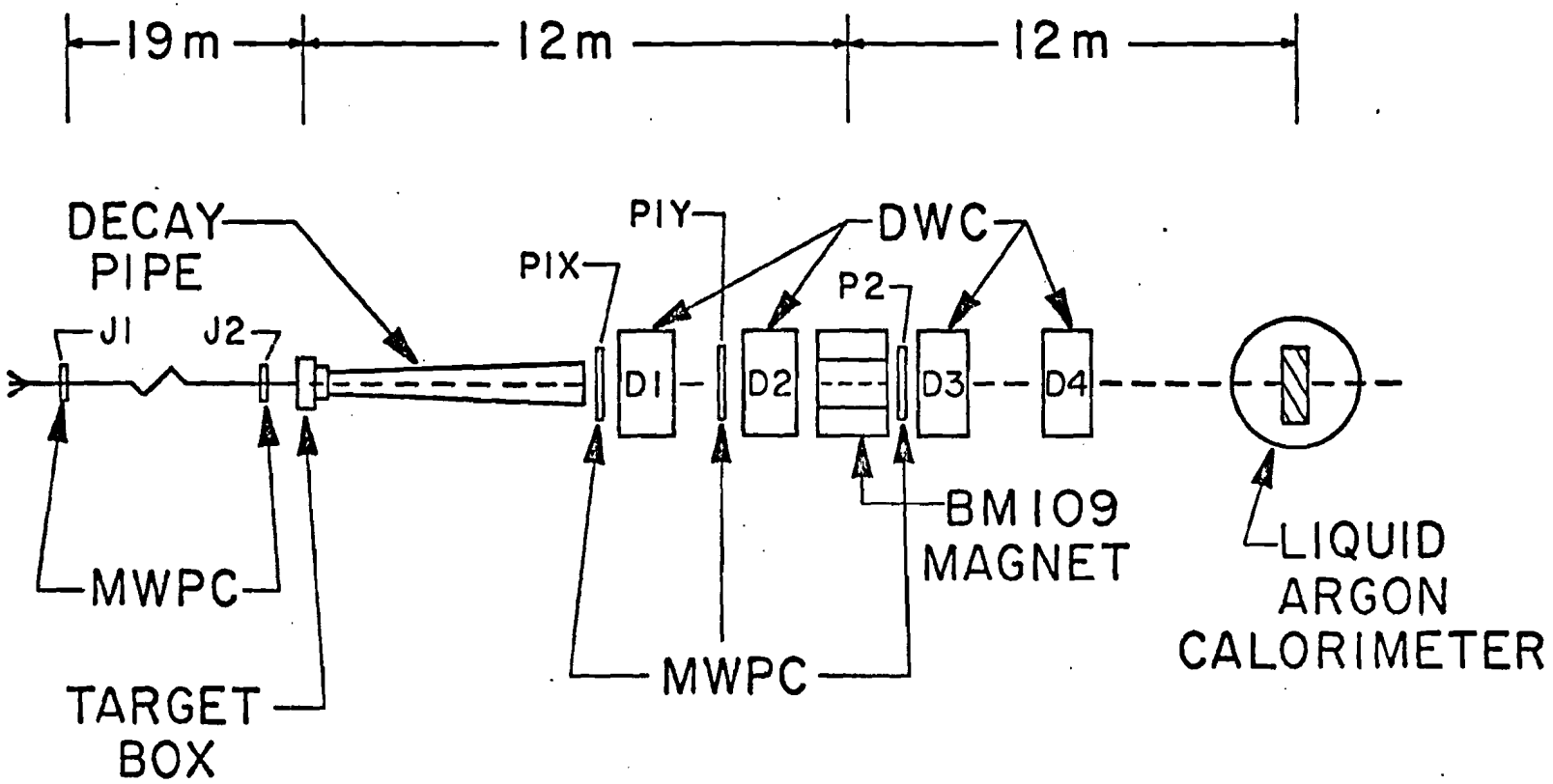
19m
12m
12m
DECAY
PIPE
J1
J2
PIX
PIY
DWC
P2
D1
D2
D3
D4
BM109
MAGNET
LIQUID
ARGON
CALORIMETER
MWPC
TARGET
BOX
MWPC

Figure 4

$$A_2^+ \dashrightarrow K^+ K_S^0 \tag{9}$$

followed by

$$K_S^0 \dashrightarrow \pi^+ \pi^-$$

and;

$$K^{*+}(1430) \dashrightarrow K^+ \pi^0 \tag{10}$$

followed by

$$\pi^0 \dashrightarrow \gamma\gamma$$

or

$$K^{*+}(1430) \dashrightarrow \pi^+ K_S^0 \tag{11}$$

followed by

$$K_S^0 \dashrightarrow \pi^+ \pi^-$$

are the subject of this thesis.

Along with the reactions listed above, the kaon decays

$$K^+ \dashrightarrow \pi^+ \pi^0$$

$$K^+ \dashrightarrow \pi^+ \pi^+ \pi^-$$

$$K^+ \dashrightarrow \pi^0 e^+ \nu$$

were used as test to our analysis and calibration procedures. They were topologically similar to the decays (8) - (11) and helpful to investigate the behaviour of the spectrometer. This subject is discussed in detail in Chapter IV.

A high resolution forward spectrometer was build to detect the final state charged particles and photons. The radiative decay widths were then determined by fits of Equation (7) to the t-distribution of these events.

The charged particles were not tagged, i.e not identified as pions, kaons etc., but momentum analized by drift chambers (D1-D4) and a BM109 magnet. These chambers and multi wire proportional chambers (MWPC) were used to determine particle momentum vectors. Energies and positions of photons were measured by a Liquid Argon Calorimeter (LAC). Section D discusses these detectors. The experimental trigger, sensitive to the above decay modes, is explained in Section F.

B. THE BEAM

The spectrometer was set up in the M-1 East beam line of the Meson Laboratory of Fermilab. The beam originated in the interaction of 400 Gev/c primary protons of the main ring with a 38 cm long (1.25 collision length) beryllium target. The production angle, which varied from 3.6 mrad to 1.9 mrad, was about 2.5 mrad during most of the data taking period.

The M-1 beam is a three stage beam[21]. The first stage provides dispersion for momentum selection. In this stage the particles are focused at 137 m downstream of the production target and a collimator positioned there can be used to define the range of momenta transmitted to the experimental area. The second stage recombines the momenta

and the beam is refocused at 244 m. The third stage provides a 50 meter long parallel region for particle tagging by Cerenkov counters. Ray traces of selected beam particles along with a schematic of the beam line are shown in Figure 5.

The M-1 beam, when operated at 200 Gev/c and produced by 400 Gev/c primary protons, is composed at its nominal 3.6 mrad production angle of 2.5% K^+ , 14.0% π^+ and 83.5% p at about 400 meters downstream of the production target. The corresponding negative secondary beam contains 3.5% K^-, 95.7% π^- and 0.8% $\bar{p}$. The experiment required an incident kaon flux of greater than 10^5 per pulse. The nature of the final states and the spectrometer limited the incident beam flux to less than or equal to 10^6 particles per second. Therefore neither the positive nor the negative beam as they were was satisfactory for the purposes of the experiment, and a beryllium filter was used to enhance the kaon fraction of the beam[22]. Because of the difference in the total interaction cross section for pions, kaons and protons, such a filter produces a different attenuation to the components of a beam consisting of all three. In particular, since kaons have smaller total cross section, passage through such a filter yields a beam enriched in kaons.

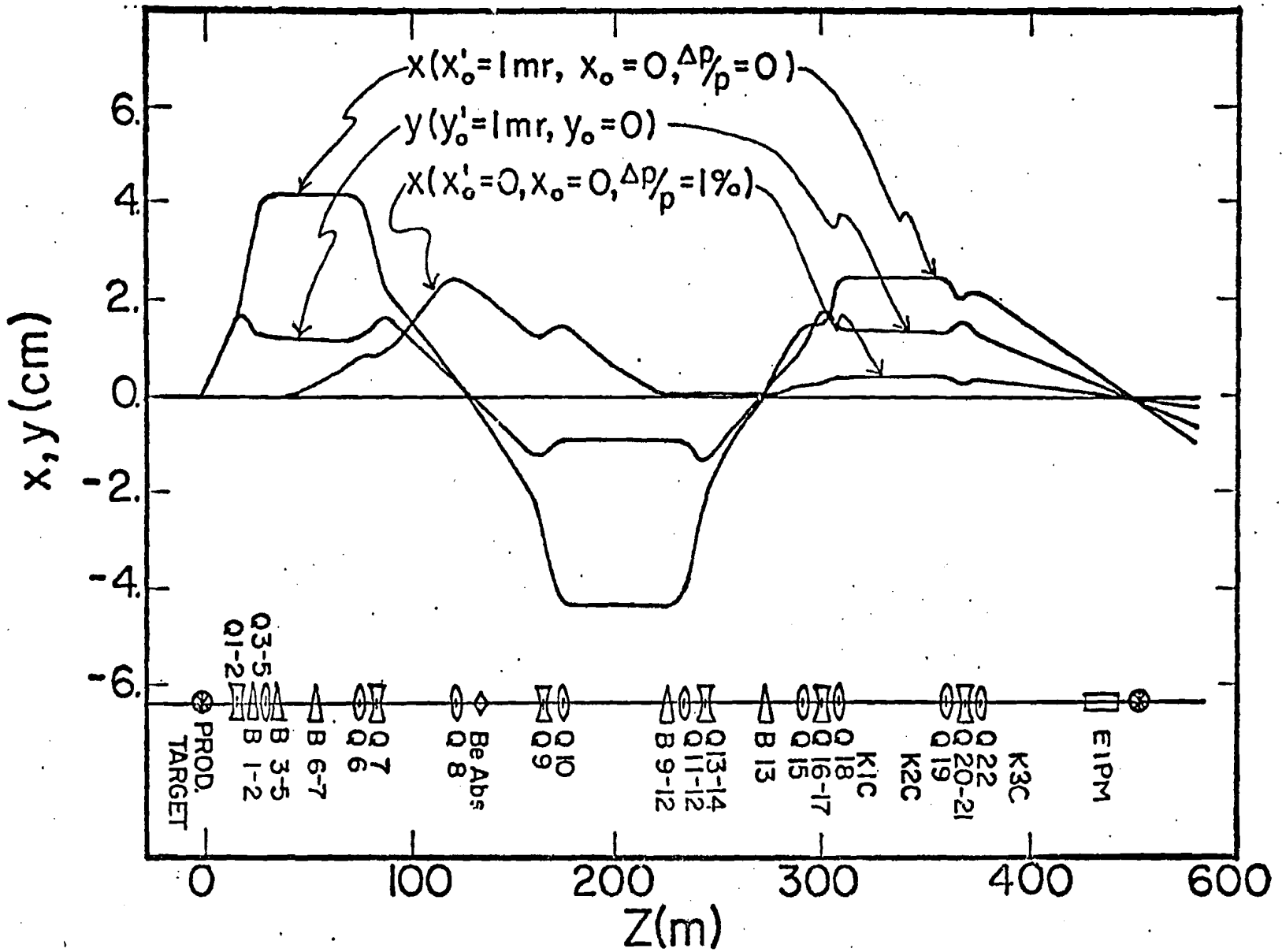
x(x'o=1mr, xo=0, Δp/p=0)
y(y'o=1mr, yo=0)
x(x'o=0, xo=0, Δp/p=1%)
x,y(cm)
6.
4.
2.
0.
-2.
-4.
-6.
0
100
200
300
400
600
Z(m)
PROD. TARGET
Q1-2
Q3-5
B 1-2
B 3-5
B 6-7
Q 6
Q 7
Q 8
Be Abs
Q 9
Q 10
B 9-12
Q 11-12
Q 13-14
B 13
Q 15
Q 16-17
Q 18
K1C
K2C
Q 19
Q 20-21
Q 22
K3C
E1PM

Figure 5

The K^- / π^- intensity ratio in the negative beam is less than the K^+ / π^+ ratio in the positive beam, but $K^+ / (\pi^+ + p)$ ratio is also smaller compared to $K^- / (\pi^- + \bar{p})$. However, the difference in the proton-kaon absorption cross sections is much larger than the difference in the pion-kaon absorption cross sections, therefore it is more efficient and easier to filter out the protons rather than the negative pions. Consequently, a positive beam was the choice for attaining an improved kaon beam fraction.

The beryllium absorber was made of four metal blocks. Each was 10 cm X 10 cm in cross section and ranging in length from 15 cm to 125 cm, the total being 221 cm. Any combination of these four blocks could be inserted into the beam remotely at a momentum dispersion focus, to minimize the effect of the multiple scattering, 130 meter downstream of the production target. There the vertical divergence was +/- 0.8 mrad and the horizontal divergence was +/- 0.4 mrad. Multiple scattering of the beam through two meters of beryllium contributed 0.2 mrad at 200 Gev/c. The effect of the multiple scattering could be seen from the response of the downstream Cerenkov counters. The beam had to be retuned when the length of the beryllium absorber was changed.

The beam fractions of the K^+, π^+ , p particles for a

production angle of 3.6 +/- 0.45 mrad (P_T=720 +/- 90 Mev/c) are shown in Figure 6 as a function of the absorber length. Figure 7 shows the beam particle fractions as a function of production transverse momentum with no beryllium and with 221 cm beryllium. Using 221 cm of beryllium filter, we could obtain a 14% K^+ fraction in a beam with a total flux of $5X10^5$ particles per second at our experimental target. The K^+/π^+ fraction in the beam was enhanced by about a factor of two. The kaon tagging efficiency, as it will be explained below, was maintained at greater than 97%[22].

The beam particles were tagged by two differential Cerenkov counters, K1 and K2, and one threshold Cerenkov counter K3. Counter K1, which is 32.3 m long, accepted light radiated at a 7.5 mrad angle. Counter K2, being 16.2 m long, had a Cerenkov angle of 15 mrad[23]. They had two rings of six phototubes each. The signals from adjacent phototubes of the inner ring were combined to obtain three signals and then the particles were tagged by requiring 2-fold or 3-fold coincidence of these three. The outer ring of phototubes which was available for vetoing was not used.

K3 accepted light radiated at an angle less than 5 mrad with one of its phototubes and light at angles greater than 5 mrad with the other[24]. Tagging the particles required

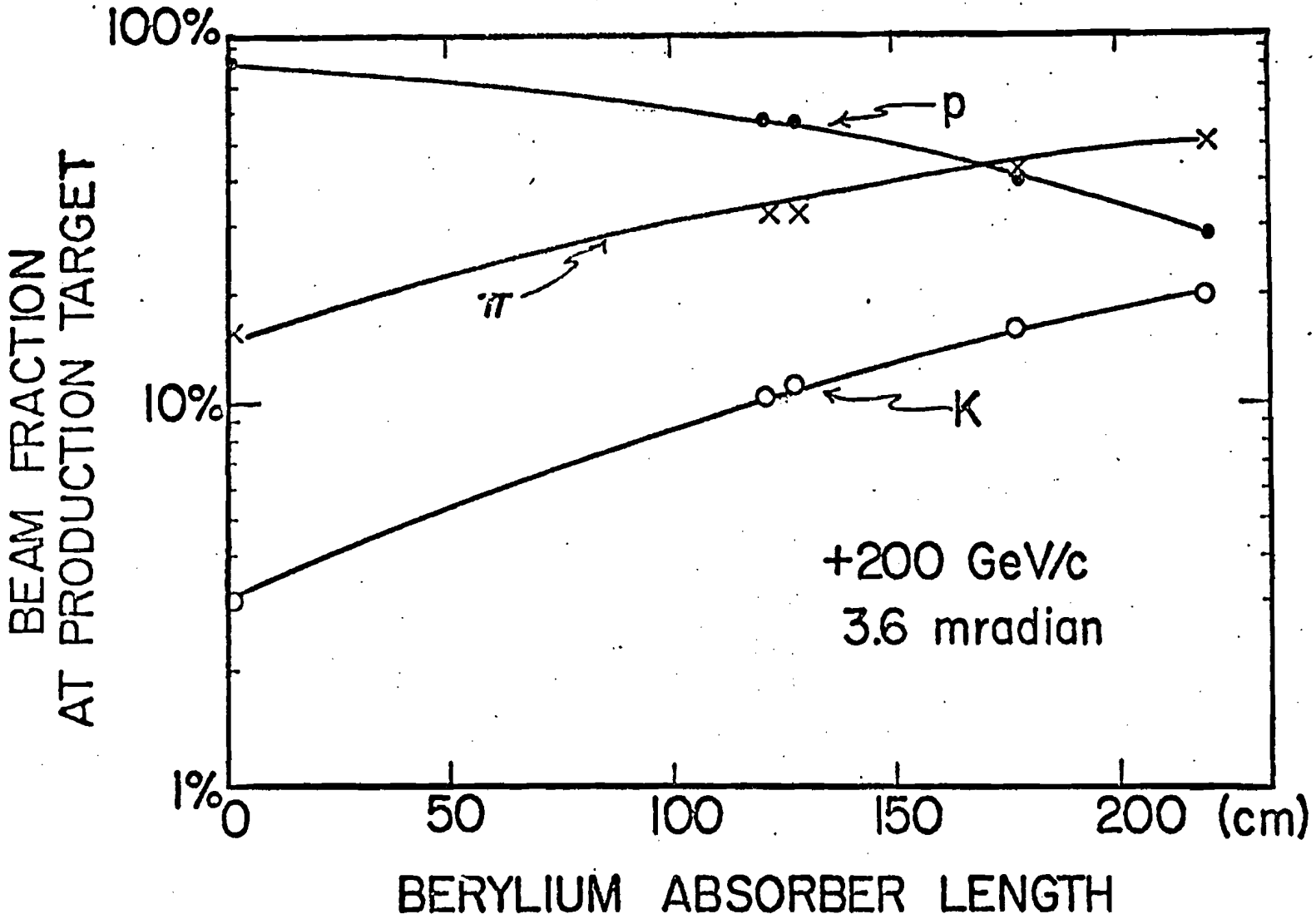
100%
10%
1%
BEAM FRACTION
AT PRODUCTION TARGET
p
π
K
+200 GeV/c
3.6 mradian
0
50
100
150
200
(cm)
BERYLIUM ABSORBER LENGTH

Figure 6

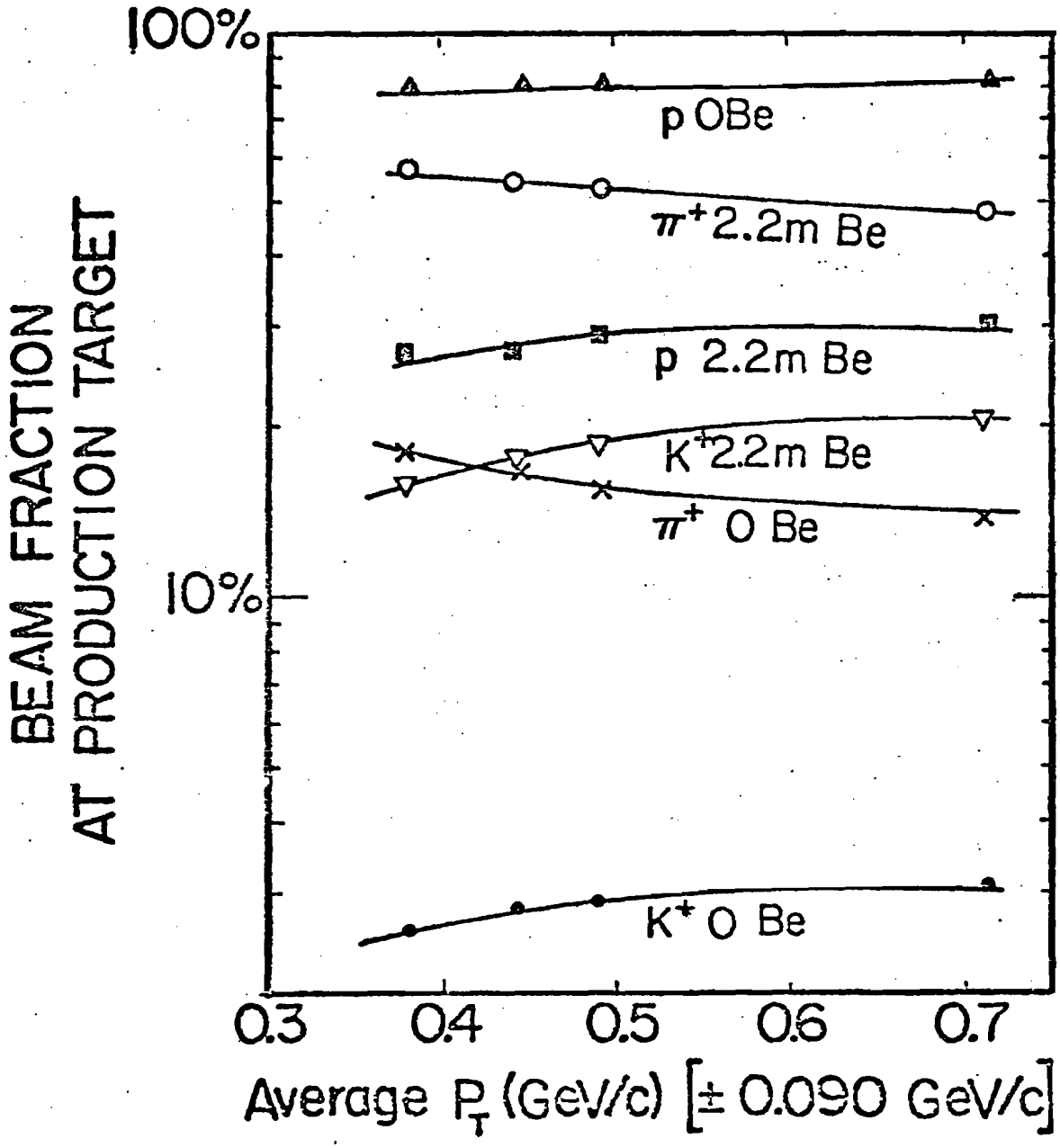
100%
10%
BEAM FRACTION
AT PRODUCTION TARGET
p OBe
π+2.2m Be
p 2.2m Be
K+2.2m Be
π+ O Be
K+ O Be
0.3
0.4
0.5
0.6
0.7
Average PT (GeV/c) [± 0.090 GeV/c]

Figure 7

signals from the inner phototube while vetoing on signals from the other one.

The Cerenkov counters were filled with helium. The pressures were adjusted for K1 to define kaons, K2 to define pions, K3 to define protons. The plots showing the particle fractions as a function of pressure are presented in Figures 8, 9, 10 with 1.2 m beryllium absorber present. On these figures, B stands for the beam count (see Section F).

In Figure 8 the pressure curve for K1 is shown for 2-fold and 3-fold coincidences. While tuning the beam, a compromise had to be made between sensitivity to scattering in the beryllium absorber and a good Cerenkov tagging. As a result, the counter was somewhat inefficient. The efficiency was ~97% for the 2-fold coincidence, almost independent of the absorber thickness. Requiring a 3-fold coincidence reduced the efficiency to ~80% with 2.1 meter of beryllium absorber, to ~90% without it. The pion contamination under the kaon peak was about 1.5% of the kaons even with the 2-fold coincidence; this was considered adequate for the experiment. The K2 counter was %98 efficient with 2.1 m beryllium absorber present. The kaon contamination under the pion peak is found to be less than 0.5%.

A direct control over various elements of the beam line

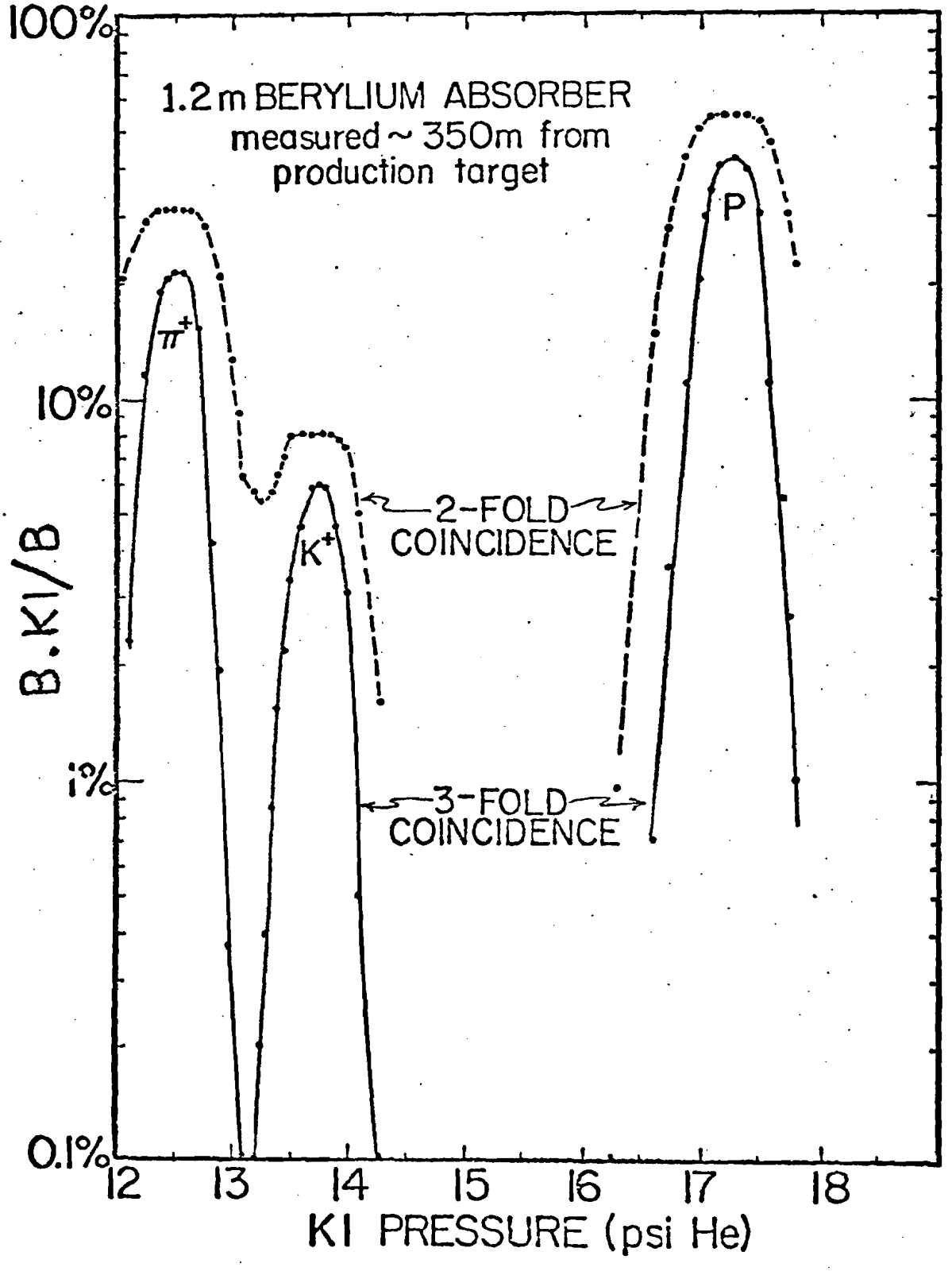
1.2 m BERYLIUM ABSORBER
measured ~ 350m from
production target
100%
10%
1%
0.1%
B.K1/B
π+
K+
P
2-FOLD
COINCIDENCE
3-FOLD
COINCIDENCE
12
13
14
15
16
17
18
K1 PRESSURE (psi He)

Figure 8

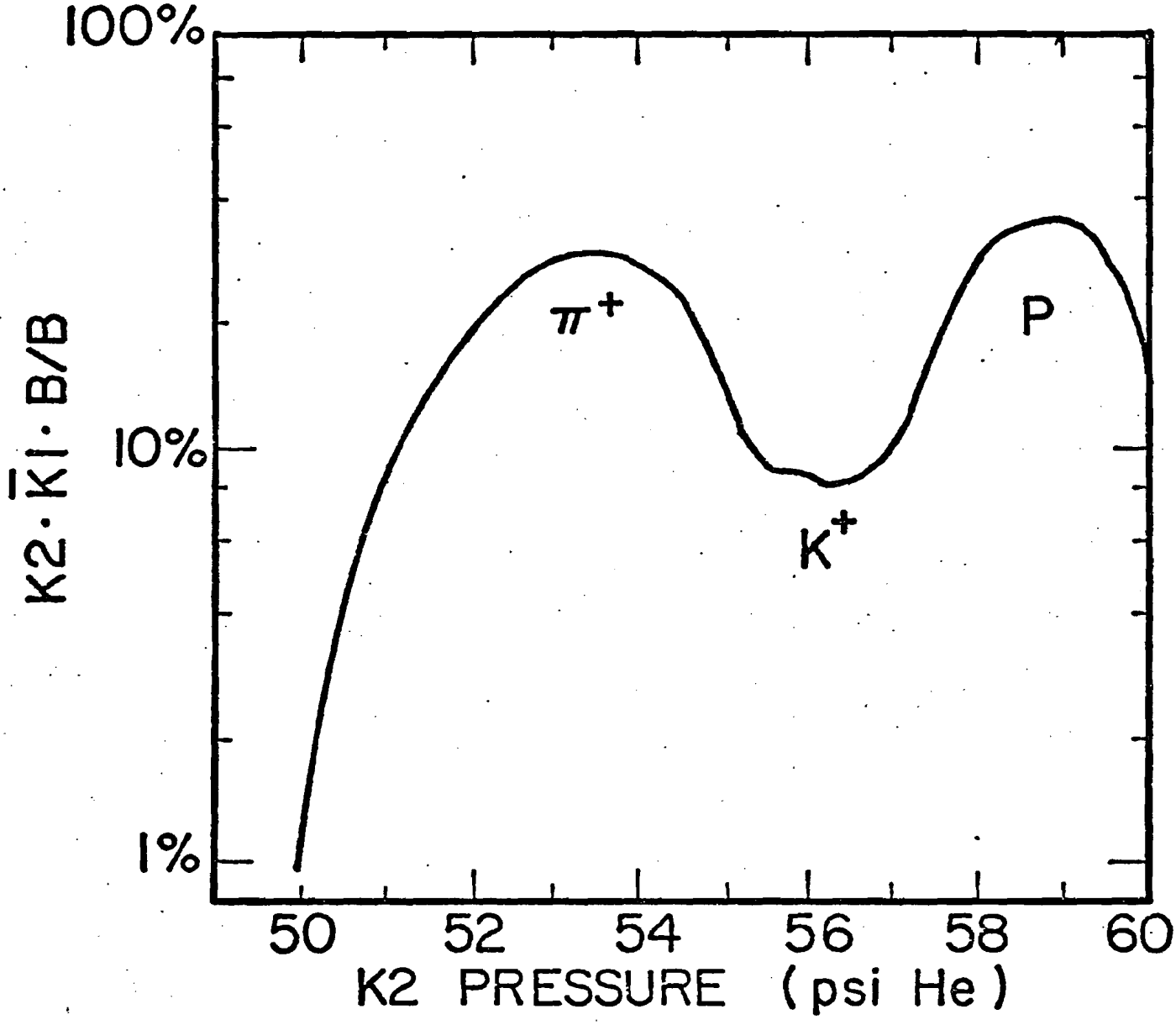

Figure 9

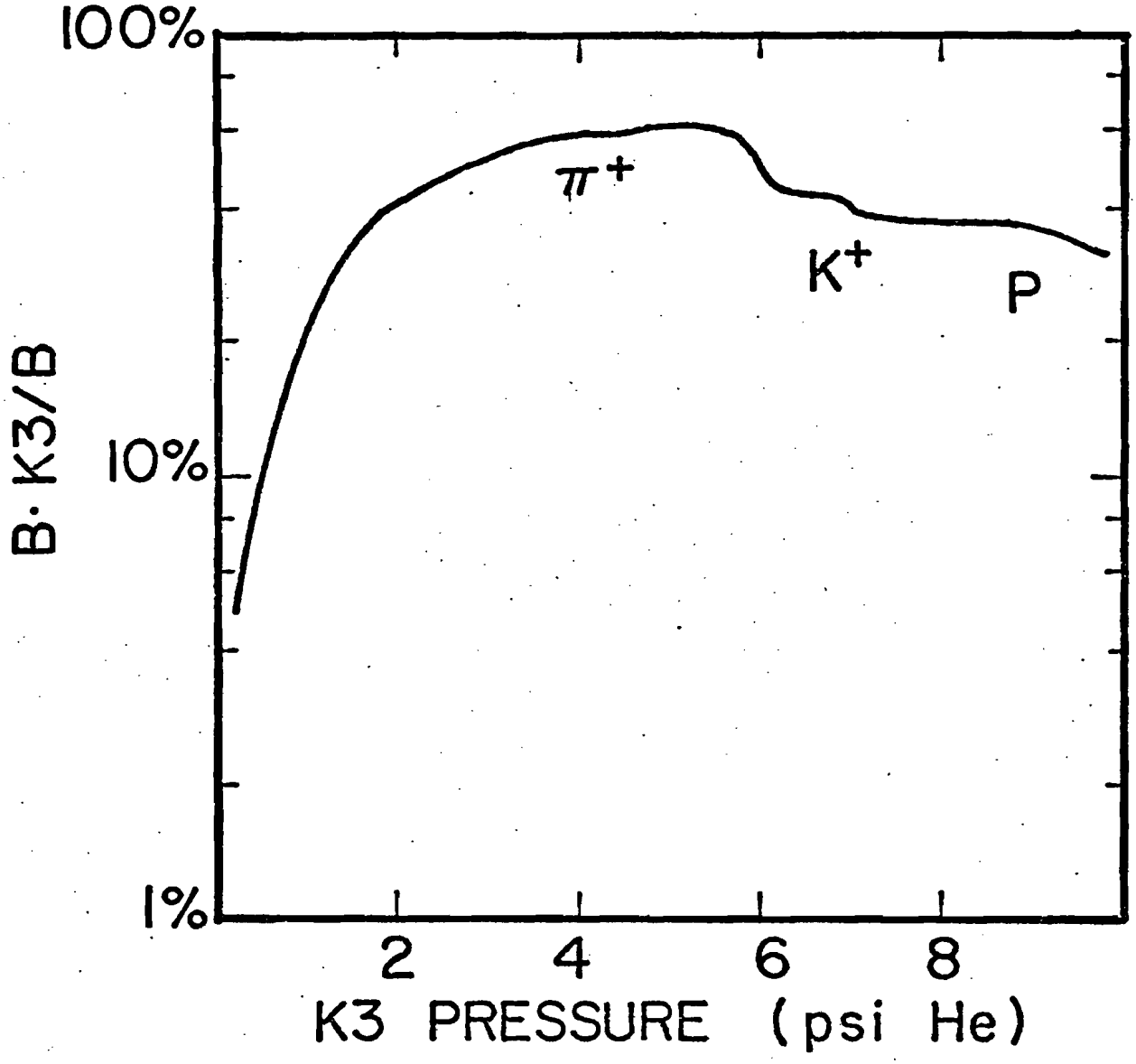

Figure 10

was available through a beam line computer. The beam spot size was monitored by the information provided by several integrating wire chambers located at certain positions along the beam line. The beam intensity was typically $2\text{-}5\times10^5$ particles per spill and this was adjustable by the collimators located at 50-270 m downstream of the production target. The main ring accelerator control provided a series of reference times to indicate the beginning and the ending of the main ring "flat-top", that is the time during which the beam was extracted from the main ring. These reference times were used for gating the electronics during the beam spill.

C. THE TARGETS

Two kinds of nuclear targets were used in the experiment. The properties of these targets are listed in Table I.

The targets, 3.75 cm x 3.43 cm in transverse dimensions, were placed and glued in a thin lucite box which was inserted inside the target-veto assembly (see Figure 15). The rate of the multiple Coulomb scattering was the criterion governing the choice of thicknesses of the individual targets. The multiple scattering limits the t-resolution (see Figure 35 for example) for the copper target, which was the thickest.

TABLE I. PROPERTIES OF THE TARGETS

Element	Atomic Number	Atomic Weight	Thickness (*) (cm)	Thickness (*) (gm/cm^2)	Number of Radiation length	Number of (†) Collision length	$A/N_o \rho t$ (barns)
Copper (Cu)	29	63.54	0.638±0.003	5.666±0.006	0.4406±0.0005	0.0682±0.0001	18.62±0.02
Lead (Pb)	82	207.19	0.124±0.003	1.378±0.002	0.2163±0.0003	0.0123±0.0001	249.68±0.36

(*) Area : 3.43 cm X 3.74 cm

(†) For proton

D. PARTICLE DETECTION

Charged kaons and pions as well as photons were to be detected in the final states of Reactions (8)-(11). Two sets of MWPC's, one set of drift chambers and the LAC were used for this purpose.

1. The Chambers

The spectrometer contained two sets of MWPC's and one set of drift chambers (see Figure 4). The proportional chambers just upstream of the experimental target, J1 and J2, were used to define the incident particle trajectory and in on line trigger logic explained in Section F. Each chamber had two X-planes and two Y-planes, with wire spacing of 1 mm. The X and Y-planes were staggered among themselves for an effective wire spacing of 0.5 mm. The angular resolution for the beam particle trajectory was +/- 0.015 mrad.

The proportional chambers P1X, P1Y and P2 were also composed of two staggered planes, each with 2.5 mm wire spacing, for an effective spacing of 1.25 mm. P1X and P2 measured the X-coordinates, P1Y measured the Y-coordinates of charged tracks. This information was used in track reconstruction and charged particle counting for trigger

logic (see Section F).

The drift chambers had a total of 24 planes and were arranged into four groups named D1, D2, D3, D4. The trajectories of charged tracks before and after the magnet BM109 were determined by these chambers.

System D1 contained two X-planes, two Y-planes and two U-planes, all in a common gas volume. U-planes were oriented at an angle of 30° with respect to the vertical. The system D2 was identical to D1 with one exception: the U-planes were replaced by V-planes which were oriented at -30° with respect to the vertical. These two systems had active areas of 20.3 cm vertically by 61.0 cm horizontally to match the aperture of the analyzing magnet.

The chambers D3 and D4 were identical. Each had six planes with separate gas volumes. In each system two planes were rotated +18.5° (U-planes), another two -18.5° (V-planes) with respect to the vertical. D3 had an active area of 45.7 cm x 111.8 cm, and D4 of 61.0 cm x 152.4 cm [25].

The maximum drift distance in these chambers was 1.0 cm. This corresponds to a ~200 nsec drift time. All planes had the same cell dimensions. One of the two planes in the

same coordinate was offset by one half of a cell relative to the other. This is the standard method to resolve the left/right ambiguity, i.e to determine at which side of a sense wire the particle passed through the chamber.

The signals from the sense wires were amplified and shaped by circuits mounted on the chambers. The outputs from these circuits were carried by 64 element flat cables to drift chamber digitizers. Each digitizer, LeCroy Research System (LRS) model 2770A, had 98 8-bit time-to-digital converters (TDC) in a triple width CAMAC module.

A block diagram of the system that was used to record the information from the drift chambers is shown in Figure 11.

The TDC units were enabled at the leading edge of the amplifier signal and halted at the leading edge of a stop pulse. The stop pulse was delayed by a programmable delay to assure the time distributions for real data to fall into the allowed range of the TDC units. Also, by varying this delay relative to calibration start pulses a calibration of the TDC's was obtained. Between spills, the on line program cycled the delay through four standard values for four calibration pulses and then reset it to the value used for real data. The four calibration data were used to determine the offsets and gains of the channels.

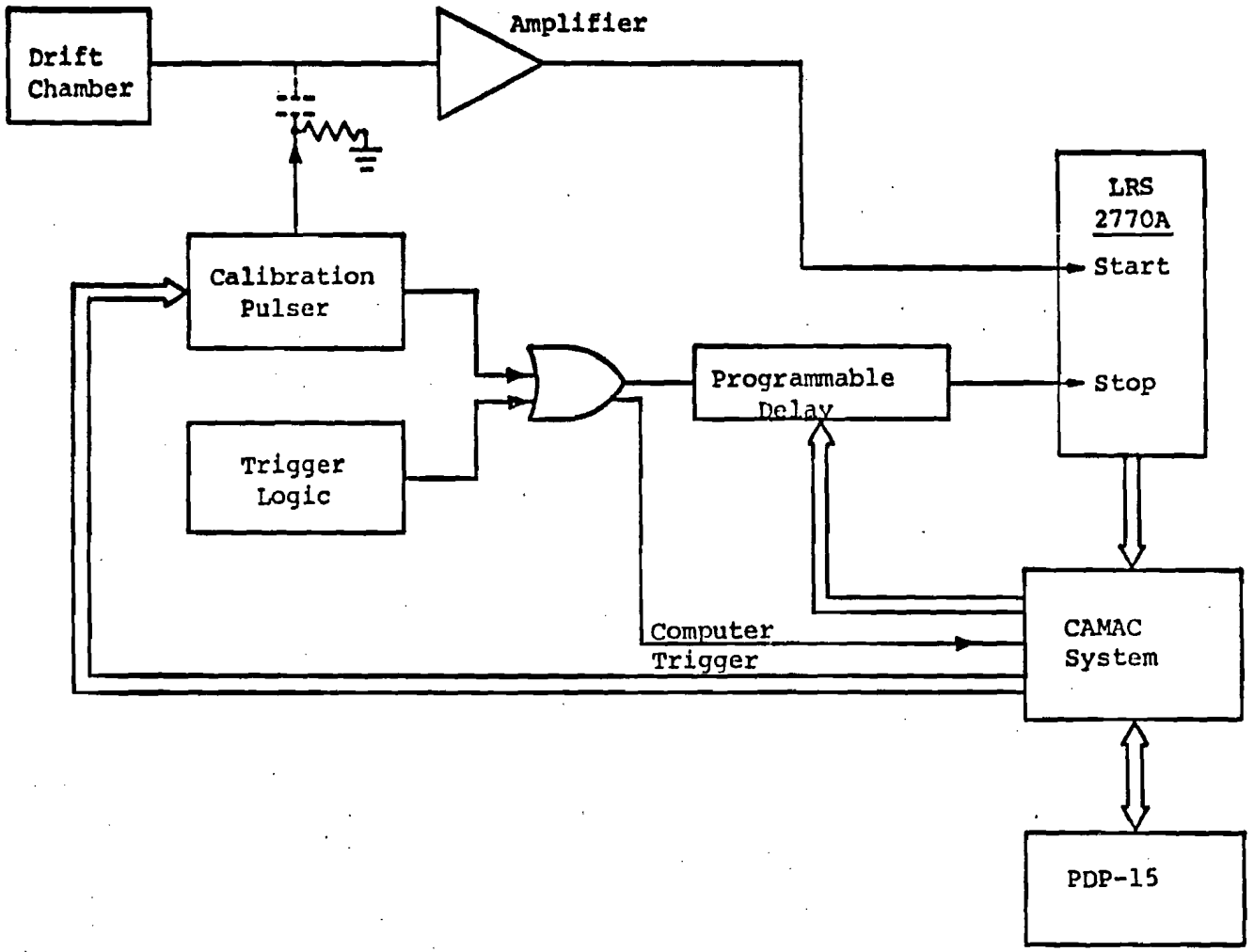
Drift Chamber
Amplifier
LRS 2770A
Start
Stop
Calibration Pulser
Trigger Logic
Programmable Delay
Computer Trigger
CAMAC System
PDP-15

Figure 11

There were six calibration pulsers (one shown in the Figure 11 with one of the 16 output lines). Each line from these pulsers was coupled to eight amplifier channels and the pulsers were triggered by the computer one at a time. The signals from these six modules were fanned in to generate one common stop for the TDC's which also was used to start the computer read-out.

2. The Liquid Argon Calorimeter

The energies and the positions of photons from π^0 and η decays were measured by using a liquid argon ionization calorimeter (LAC). The theory and design of such calorimeters are well documented[26], and they have proven to be very powerful and accurate instruments for detecting electrons, photons and even hadrons. This type of calorimeter has certain advantages over lead-glass or lead-scintillator systems. They are easy to segment and relatively inexpensive to build. Certain problems, like phototube instability, which is unavoidable in other types of photon detectors, do not exist. They have energy and position resolutions comparable to and sometimes better than those of other detectors. They are, however, somewhat complicated and sophisticated devices because of their cryogenics requirements. The one that was built for this experiment was composed of 61 lead plates and 62 copper-clad

G-10 boards. Figure 12 shows two cells of the detector.

The 2 mm thick lead sheets were separated on each side by a 2 mm wide liquid argon gap from 1.6 mm thick G-10 boards. The boards were clad with 0.025 mm thick copper. The gaps were defined by spacers along the edge of the detector; small button-like spacers scattered randomly over each G-10 board ensured homogeneity of each gap across the whole detector surface. All the plates, boards and spacers were held together and attached to a cradle by stainless steel bolts. The insert in Figure 12 shows this configuration. In this arrangement the detector was 24.5 radiation lengths and 1.6 proton-interaction lengths thick.

The G-10 boards were segmented into 1.27 cm wide strips which extended along the X and Y directions on alternate boards. Furthermore, the Y boards were divided into left and right sections, and the whole assembly was separated into front and back halves. Thus, there were six separate sections, X-front, X-back, Y-front right, Y-front left, Y-back right, Y-back left. Within each section, the strips on all boards reading out the same coordinate position were connected to a single amplifier. This way the detector was made up of 480 amplifier channels, 224 for X, 256 for Y coordinates.

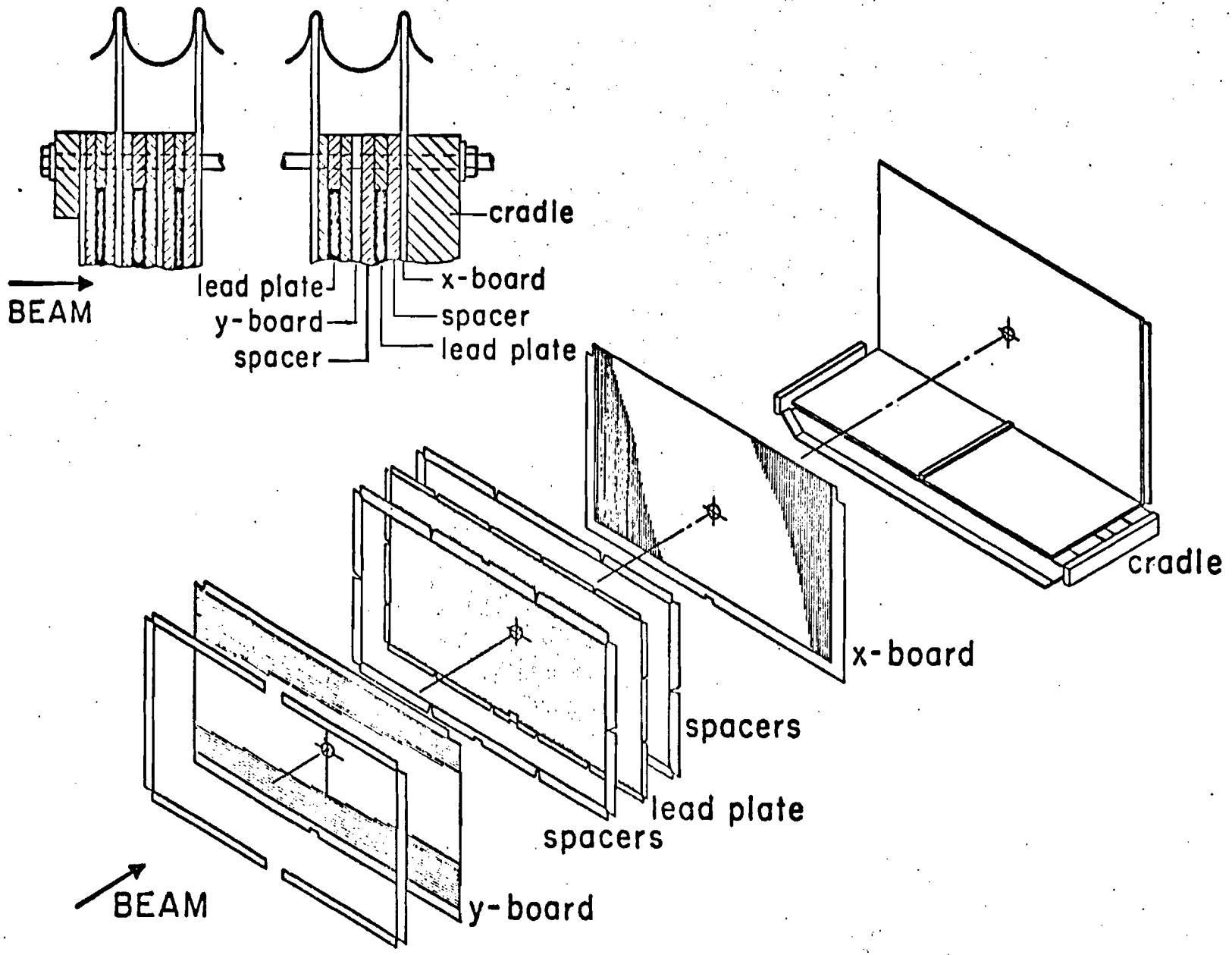
cradle
BEAM
lead plate
y-board
spacer
x-board
spacer
lead plate
cradle
x-board
spacers
lead plate
spacers
BEAM
y-board

Figure 12

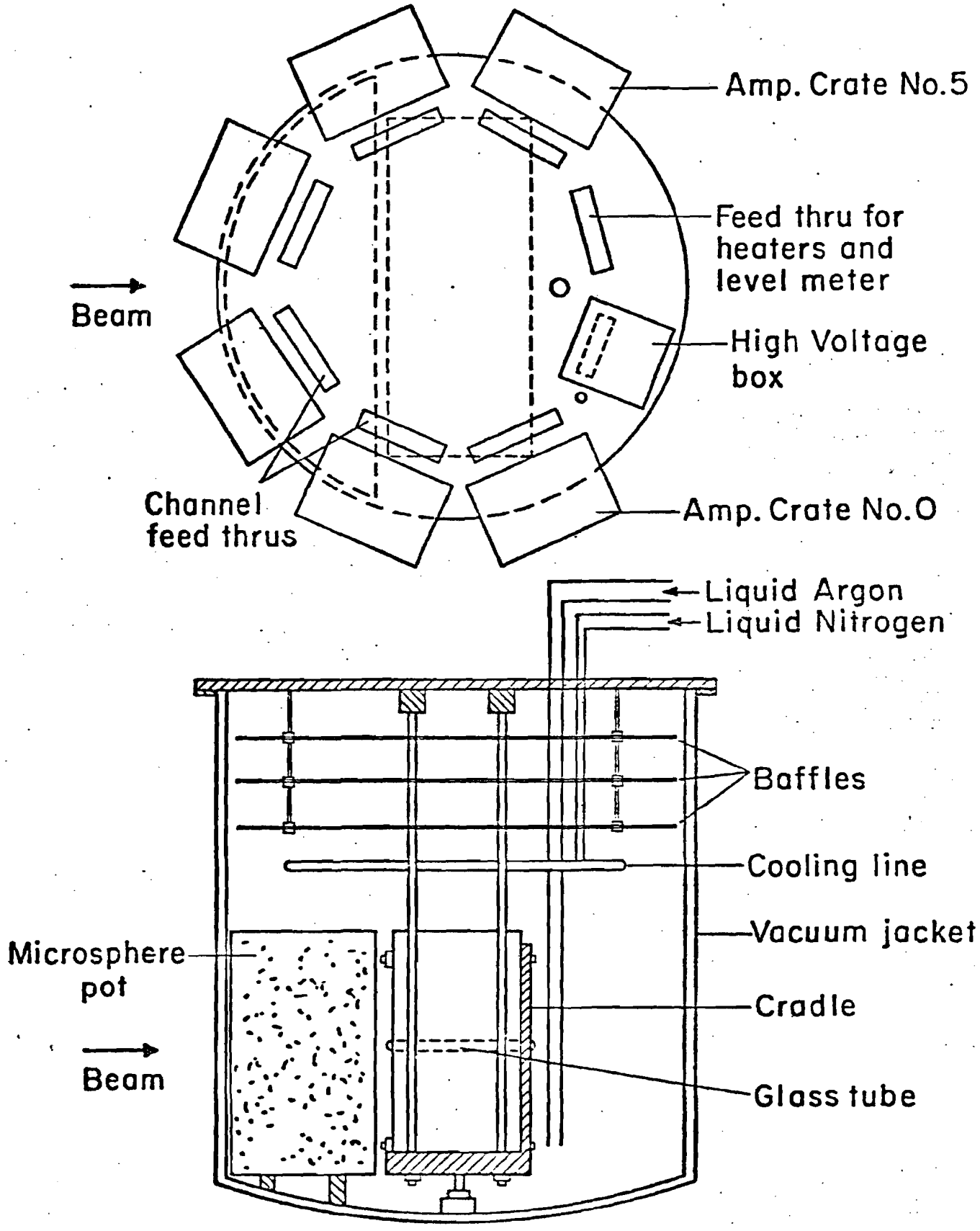
Amp. Crate No.5
Feed thru for heaters and level meter
High Voltage box
Beam
Channel feed thrus
Amp. Crate No.O
Liquid Argon
Liquid Nitrogen
Baffles
Cooling line
Vacuum jacket
Microsphere pot
Cradle
Beam
Glass tube

Figure 13

The sensitive area of the whole detector was 140 cm horizontally and 81 cm vertically. Each plate and board had a 1.9 cm diameter hole at the center for the direct beam to pass through. This region was filled with an evacuated quartz tube in order to minimize the beam interaction inside the detector.

The whole detector was suspended from a steel cover plate inside a cylindrical cryostat. The top and side views of the cryostat-detector assembly are shown in Figure 13. The section of the cryostat in front of the detector was filled with a pot which contained hollow glass microspheres. The wall of the cryostat, the microsphere pot and about 3 cm of liquid argon between the detector and the pot contributed ~0.9 radiation length of material along the beam direction.

The detector channels were led to feed-thrus at the top plate and then to six amplifier crates by flat cables. These cables were two 0.025 mm thick copper layers separated by 0.13 mm thick mylar. The back layer was used for ground. The top layer was segmented into 0.64 cm wide strips, one for each channel. In this configuration the equivalent impedance of the cables was ~10 ohms and therefore, as a precaution, each cable was back terminated by 10 ohm resistors at the connection points to the detector strips.

There were six resistor-heaters attached to the cradle. They were also led to the top of the cryostat to a separate feed-thru. An argon level indicator, made from a 3 cm wide G-10 board with 16 temperature sensitive resistors attached to it, was monitored through cables that were led to the same feed-thru. Similar temperature sensitive resistors placed at six locations on the detector were used to monitor its temperature during cool-down and warm-up, and keep the temperature gradient 10°C across the detector.

About 3000 liters of liquid argon were required to submerge the detector. The argon could be transfered between the cryostat and a storage dewer through transfer lines. The amount of the argon inside the cryostat was monitored by the level indicator. A liquid nitrogen line circling inside the cryostat was used to cool the argon to liquid argon temperature. Commercially provided argon had to be purified to less than 0.1 part/million oxygen contamination, since studies showed that the presence of oxygen inside the argon reduced the charge collection and therefore pulse height drastically[27].

Figure 14a shows the block diagram of the electronics for a single channel in the LAC system[28]. The charge generated by the electromagnetic shower was integrated by amplifiers matched to the detector's capacitance of ~5000

a) Electronics for one channel of LAC

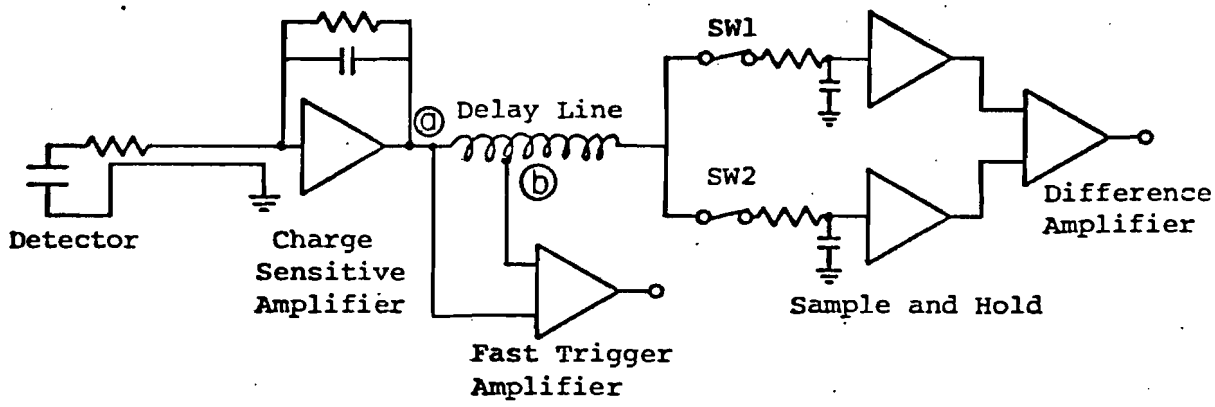

b) Signal at point ⓐ

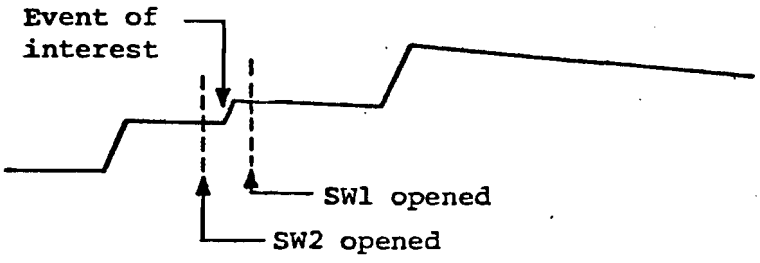

c) Read-out system

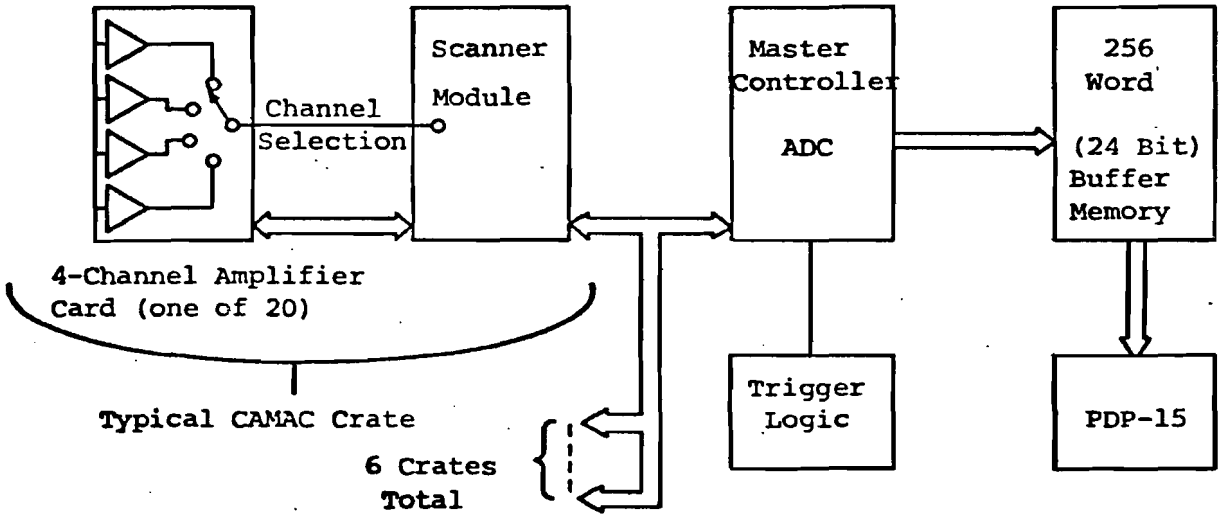

Figure 14

picofarads. The rise time of ~200 nsec was basically determined by the drift velocity of the electrons inside the liquid argon.

The inductance L and the capacitance C' of the lead cables were significant enough to contribute to the the rise time. Since any signal with rise time less than ~ LC, C=capacitance of the detector system, could not pass through without any distortion, the shape and the length of the cables were important. With the structure described above, the cables had an inductance of 25 nHy and a capacitance of 900 picofarads. For the detector with capacitance of 5000 picofarads this corresponded to a lower limit of ~120 nsec on rise time which was small enough not to worry about the limitation due to electron drift velocity in the argon. The decay time constant of the amplifiers was about 400 microsec. Thus the output of the amplifiers at point (a) in Figure 14a was a series of step pulses as shown in Figure 14b. Each step pulse corresponded to one interaction. For the event of interest, the levels of the step pulse just before and after its arrival were sampled and the difference of these levels, proportional to the energy deposited in the detector, was digitized. The amplifiers around the beam hole had a shorter decay time constant of 20 microsec to prevent saturation caused by a high interaction rate.

The signal at (a) was inverted and added to the same signal at (b) after a delay of 200 nsec to obtain a fast output. These signals, crudely proportional to the energy deposition, were used for the Y-channels in the trigger logic as explained in Section F.

Four amplifiers were placed on one card, and twenty cards, together with a crate scanner, were mounted on one CAMAC crate. Scanners in each of the six crates were connected to a master controller with a 24-bit analog-to-digital converter (ADC). When the trigger was set, the master controller scanned all the amplifiers through the crate scanners and digitized the levels of the channels if they were above the preset threshold of ~ 600 Mev. These values along with the channel information were transmitted to a camac buffer memory which the on-line computer could access. A schematic diagram of this read out system is shown in Figure 14c.

A system was implemented to check, test and calibrate the LAC channels, too. Between spills, the pedestals and the gains of the channels were determined for each data run. For the gains, a pulse with known amplitude was fed into the inputs of the amplifiers. For the pedestals, the threshold was set to zero and then the LAC was read. Because of the buffer memory size limitation, only one crate was read out at a time during calibration between spills.

E. THE MAGNET

The magnet BM109 was used to determine the momenta of charged particles. It had an aperture of 61 cm horizontally, 20 cm vertically. The length through which the charged particles were deflected was 187 cm. The data were taken with the magnet current set to 2900 amps. This corresponded to a integrated field length ($\int B.dl$) of 36.12 KGm or a transverse kick of 1.07 Gev/c. By determining the path of the charged particles before and after they were deflected by the magnet, the radius of the curvature of the particles and consequently their momenta could be calculated.

F. THE EXPERIMENTAL TRIGGER

Various trigger logic circuits sensitive to the interactions under study were designed. They were called RHO, A1, VEE and BEAM triggers. The basic requirements of these triggers could be listed as follows:

1) RHO: One charged particle leaving the target and one or more photons in the LAC.

2) A1 : Three charged particle leaving the target and

any number of photons in the LAC.

3) VEE: One charged particle leaving the target, two more charged particle counted downstream of the target.

4) BEAM: Series of hits registered by the counters along the beam trajectory.

The above requirements had to be complemented by the definition of the beam, existence of an interaction at the target, insurance that all the produced particles went through the magnet and the right number of charged tracks were counted downstream of the target, and finally indications that the energy in the LAC was due to photons (or electons) but not hadrons.

Figure 15 shows the schematic diagram of the counters used in the trigger, and Figure 16 shows the generalized diagram of the trigger logic.

The beam was defined in the vicinity of the target by a coincidence of two scintillator counters B2 (5 cm x 5 cm x 0.16 cm) and B3 (3.8 cm x 3.8 cm x 0.16 cm). The leading edge of the signal from B3 was used as the reference time for all coincidences. Two more counters, B0 and B1, located

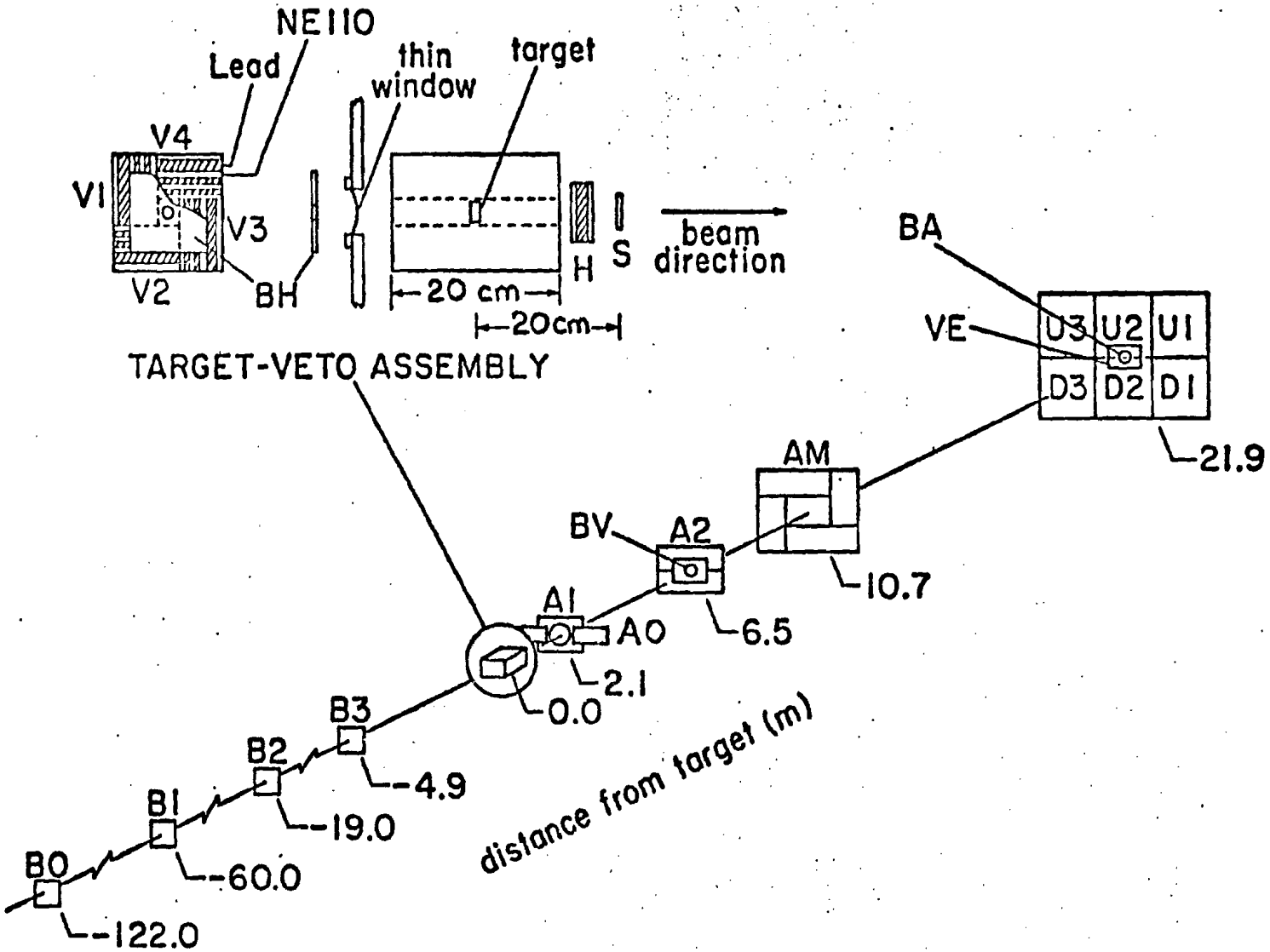
NE110
Lead
thin window
target
V4
V1
V3
V2
BH
H
S
beam direction
20 cm
20cm
TARGET-VETO ASSEMBLY
BA
VE
U3
U2
U1
D3
D2
D1
21.9
AM
10.7
BV
A2
6.5
A1
A0
2.1
0.0
B3
-4.9
B2
-19.0
B1
-60.0
B0
-122.0
distance from target (m)

Figure 15

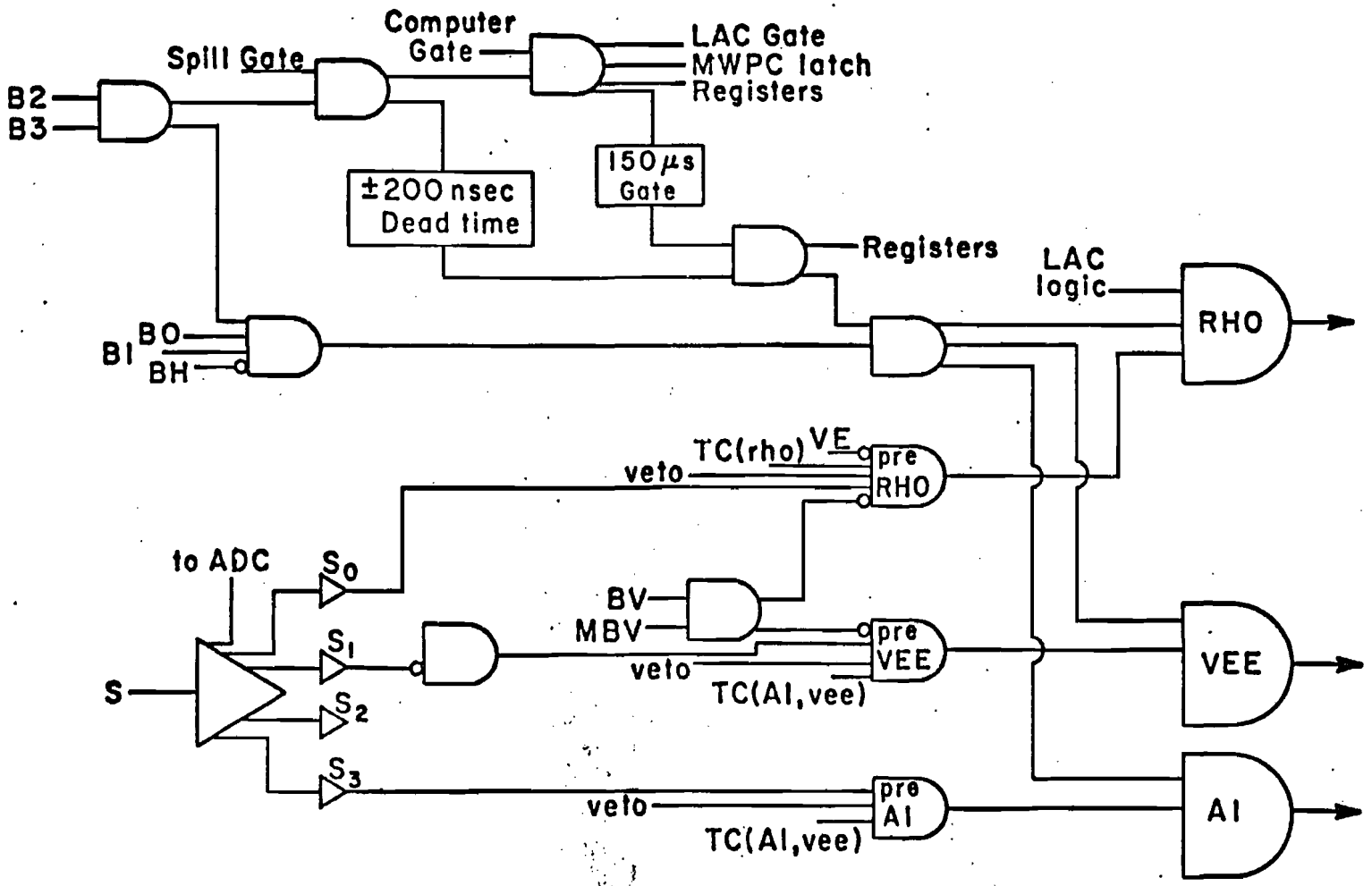
B2
B3
Spill Gate
Computer Gate
LAC Gate
MWPC latch
Registers
±200 nsec Dead time
150 μs Gate
Registers
LAC logic
RHO
B1
B0
BH
TC(rho)
VE
veto
pre RHO
to ADC
S0
S1
S2
S3
S
BV
MBV
pre VEE
veto
TC(Al,vee)
VEE
pre Al
veto
TC(Al,vee)
Al

Figure 16

at either end of the parallel section of the beam where the Cerenkov counters were located, were required to be in coincidence with B2.B3 to define the beam track. This track was, in addition, required to pass through a 1.6 cm diameter hole of a veto counter BH located 38 cm upstream of the target. Thus a beam particle was defined by the coincidence $B=B0.B1.B2.B3.\overline{BH}$. The coincidence of this signal with the signals from the Cerenkov counters determined the identity of the beam particles. For instance, B.K1 identified the kaons and B.K2 the pions. In order to eliminate the kaon contamination of the pion beam, an anticoincidence of the K1 signal was required and therefore the pion identification was made by the signal $B.K2.\overline{K1}$.

The system was capable of handling only one hit per drift wire per trigger. The drift time interval of 200 nsec after a hit had to be cleared from another hit in order to prevent any confusion during reconstruction of events. Therefore the beam particles were required to be separated in time by at least 200 nsec by implementing a dead-time of +/- 200 nsec using the B2.B3 coincidence. This caused about 10% dead-time in the trigger for B2.B3 intensities of $3x10^5$. Fast logic signals, obtained from B2.B3 and gated properly, were used to latch the proportional chamber signals, activate the LAC logic and strobe some of the scalers.

Various veto counters were utilized to reject noncoherent events, events producing particles outside of the physical acceptance region, elastic scattering events and events composed of uninteracted incoming particles (see Figure 15 for the counter locations).

For coherent interactions, the nuclei stay in their ground states and recoil with momenta of less than 100 Mev/c. Thus they do not leave the target. Four V-counters that surrounded the target were used to veto all interactions involving nuclear exitation as well as the interactions with multiparticle production. They were consisted of NE110 scitillator sheets interleaved with lead plates for a total thickness of 5.2 radiation length. The inner walls of this veto system were covered with 0.25 mm of copper to absorb the low energy delta-rays which might have been generated by the charged particles passing through the target.

The H-counter just downstream of the target was a sandwich of lead and scintillator sheets. It had a 3.2 cm diameter hole in the center for the beam pass through. Any interaction that produced particles spread wide enough to hit it was rejected by this counter. The signals from the V-counters and the H-counter were collected and transmitted to separate Amperex 56-AVP phototubes by plastic light guides.

The veto counters A0, A1, A2 and AM were used to reject events with charged or neutral particles outside of the geometrical acceptance which was limited by the aperture of the analyzing magnet. A1 and A2 were placed around the decay pipe at both ends. Two A0 counters were just in front of the pipe. The AM counters were located around the upstream aperture of the magnet. They were made of lead and scintillator layers and viewed by RCA 8575 phototubes. Each of these counters were about six radiation length thick.

Most of the beam particles passed through the targets without interacting. To avoid any confusion, events that had charged particles in the region of the beam were vetoed by the BA counter. It was a 2.9 cm diameter and 0.16 cm thick scintillator placed just in front of the LAC.

The signals from these veto counters were combined to form the signal

$$\text{VETO LOGIC}=B2.B3.\overline{BH}.\overline{BA}.(\overline{V1+V2+V3+V4}).(\overline{A0+A1+A2+AM+H})$$

which was common to all triggers. It basically defined an interaction in the target with all reaction products going through the magnet aperture and the target nucleus staying inside the target.

The number of charged particles leaving the target was determined by the S-counter located 20 cm downstream of the

target. Its scintillator had dimensions 3.8 cm x 3.8 cm x 0.16 cm. Various discriminator levels called S0, S1, S2, S3 were set to select events with one, two or more charged particles emerging from the target. The pulse height of the S-counter was also digitized for off-line studies of the discriminator levels.

The chambers and counters downstream of the target along the beam line presented 0.034 collision length of interacting material to a passing hadron. The BA counter and the veto logic alone could not have been sufficient to eliminate the events created by the beam particles interacting with this material. To suppress such events , a matrix between the signals from the chambers J1, J2 and P1X was formed. Signals from one of the X-planes in each of the J1 and J2 chambers and from the central 3 cm region of both planes of the P1X chamber were put in coincidence to form a Matrix Beam Veto (MBV). As it was set up, the matrix would be satisfied for any outgoing track that deviated by less than 0.3 mrad from the beam track defined by J1 and J2. Since MBV involved only X-chambers, it detected only the X-projection of the deviation angle. Therefore good events that contained charged tracks scattered straight up would also have been vetoed. To prevent this, a 2.5 cm diameter 0.6 cm thick counter, called BV, was placed downstream of the P1X chamber. The signal from this counter was put in

coincidence with the MBV signal and the resultant signal, MBV2=MBV.BV, was used as veto in event trigger. The efficiency of the MBV was about 90% and limited by the efficiency of the proportional chambers.

The number of charged tracks downstream of the target was determined by the track counting logic TC. This was formed by the signals from P1X, P1Y and P2 proportional chambers. A track was defined by the presence of signals on a continuous group of adjacent wires in any chamber, separated from other groups by at least one blank wire at both ends of the group. The signals from each chamber were analyzed individually by processors designed and built at Fermilab[29]. They provided logic levels, for up to five tracks, proportional to the number of groups seen in the chambers. These signals were also latched for off-line comparison with the MWPC information. They agreed at better than a 90% level. The logic signal TC(rho) required one or two tracks from the P1X-P1Y system and the P2 system; TC(al,vee) required two or three tracks from the P1X-P1Y system, three or four tracks from the P2 system. These requirements were choosen this loose because of the noise signals, delta-rays and ambiguities due to the large angle tracks in P2 which were the low momentum particles bent by the magnet.

The LAC was included in the trigger logic for the RHO trigger. Figure 17 shows the logic diagram associated with it.

Although the charged hadrons had totally different characteristics in terms of their energy deposition into the LAC (see Section A in Chapter III), they frequently interacted in the detector and caused serious background problems. For instance, elastically scattered beam particles interacting with the LAC could satisfy the RHO trigger logic and therefore had to be suppressed. For that, use of momentum conservation was made in decays like a --> b π^0 (or b η). As discussed in Chapter I, the Coulomb production of "a" was essentially along the beam direction. Therefore if the charged hadron "b" hit the LAC below the center plane of the spectrometer, the π^0 (or η) should have stayed above it, and vice versa. The active area of the LAC was covered with a wall of three UP (U1, U2, U3) and three DOWN (D1, D2, D3) counters to determine whether the charged particle hit above or below the center plane. The signals from the fast outputs of the LAC amplifiers for the upper and lower front Y-channels were added up to define the signals E(up) and E(down). The LAC logic was then satisfied for E(up) in anticoincidence with any one of the signals from UP counters or for E(down) in anticoincidence with any one of the signals from the DOWN counters. The logic was

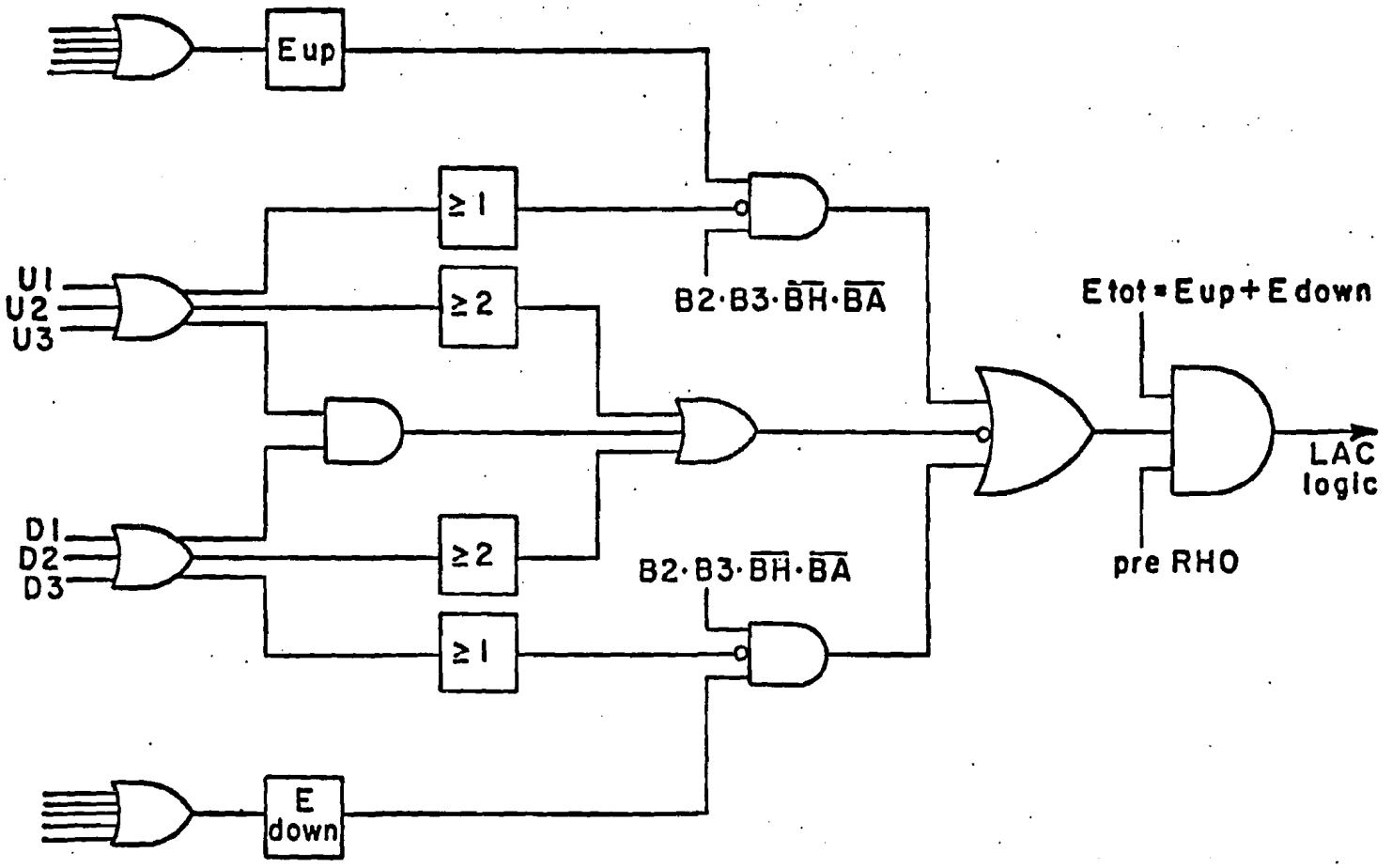
E up
≥1
≥2
U1
U2
U3
B2·B3·B̄H·B̄A
Etot = Eup + Edown
LAC
logic
D1
D2
D3
≥2
B2·B3·B̄H·B̄A
pre RHO
≥1
E
down

Figure 17

vetoed if more than one of all the UP or DOWN counters fired. Also, partly to eliminate various noise contributions, a minimum amount of total energy (E(tot)=E(up)+E(down)) was required to be registered by the LAC. E(up), E(down) and E(tot) were also digitized for off-line studies.

With the arrangement described above, charged particles hitting the LAC close to the median plane could trigger the logic because energy would be deposited both above and below the median plane. An attempt was made to eliminate this effect by the VE counter (5 cm vertically, 10 cm horizontally and 0. 16 cm thick) which was placed to cover the beam region near the median plane. Using the signal from VE as a veto caused only a small loss of good events, but eliminated most small angle elastic scattering events.

In summary, the RHO trigger was defined as:

$$RHO=B.(VETO\ LOGIC).S0.TC(rho).\overline{MBV2}.\overline{VE}.(LAC\ LOGIC)$$

the A1 trigger was defined as:

$$A1=B.(VETO\ LOGIC).S3.TC(a1,vee)$$

the VEE trigger was defined as:

$$VEE=B.(VETO\ LOGIC).(S0.\overline{S1}).TC(a1,vee).\overline{MBV2}$$

and the BEAM trigger was defined as:

$$BEAM=B.(VETO\ LOGIC).B2.B3.\overline{BH}.BA$$

with the magnet on and as:

$$BEAM=B.(VETO\ LOGIC)$$

with the magnet off.

The trigger logics were gated on during the beam spills and when the on-line computer was not busy reading.

G. ON-LINE DATA ACQUISITION AND MONITORING

Whenever the trigger was satisfied, the logic was gated off and the information was collected through the read-out and recording system shown in Figure 18.

The drift chamber signals were digitized by 11 TDC modules. The analog signals from various counters and the E(up), E(down) and E(tot) signals from the LAC system were converted and stored by two ADC units. The information from the MWPC's and the LAC were stored in two separate buffer memories. Six crates were used for this CAMAC read-out system and they were controlled by one branch driver. A PDP-15 computer, interfaced with the system, transfered the data to magnetic tapes and carried out limited on line checks on the apparatus performance.

There existed the possibility to transmit a sample of the events to the central CDC Cyber-175 computer through a special system called BISON-NET[30]. A PDP-11 computer

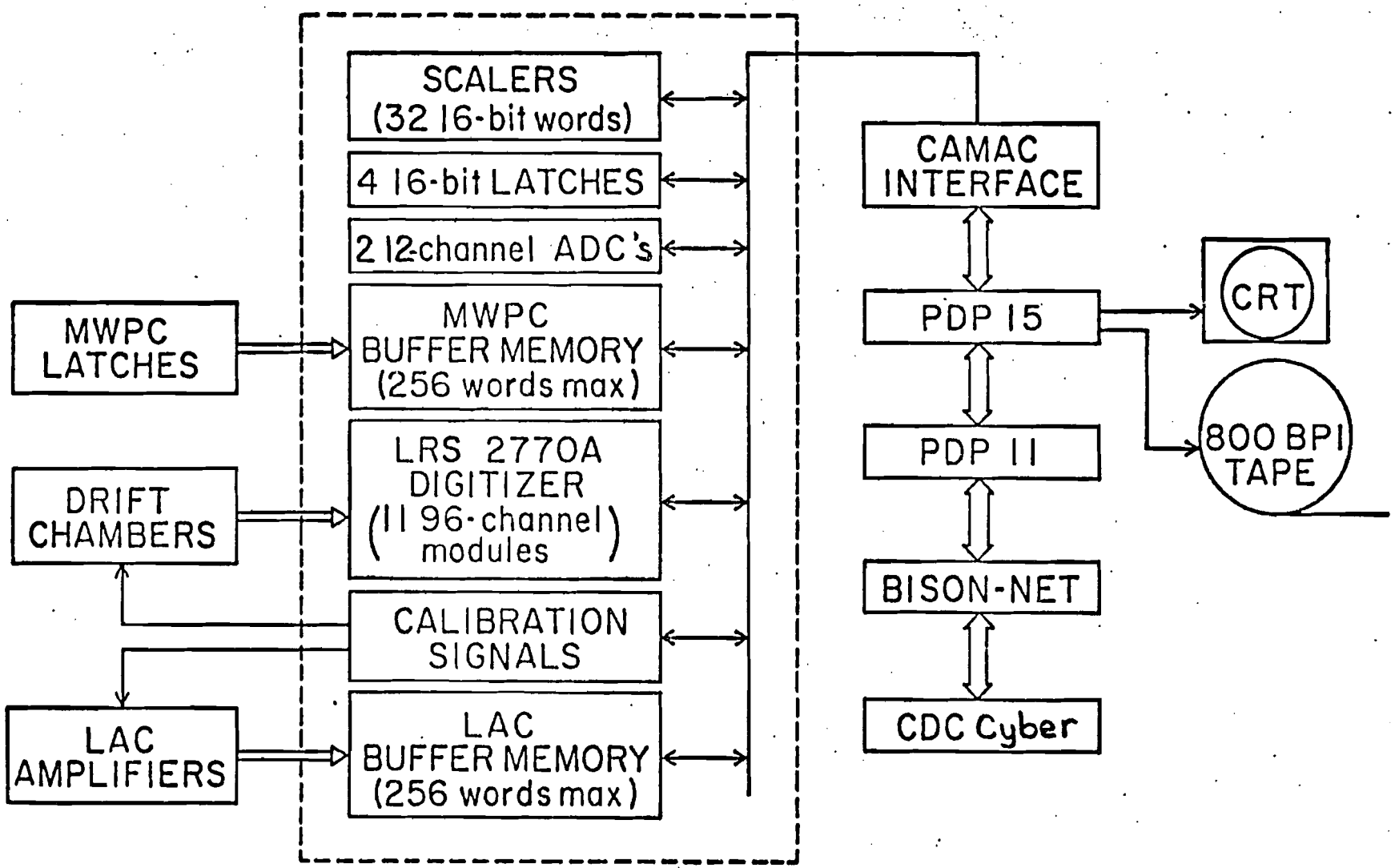
SCALERS
(32 16-bit words)
4 16-bit LATCHES
2 12-channel ADC's
MWPC
BUFFER MEMORY
(256 words max)
LRS 2770A
DIGITIZER
(11 96-channel
modules)
CALIBRATION
SIGNALS
LAC
BUFFER MEMORY
(256 words max)
MWPC
LATCHES
DRIFT
CHAMBERS
LAC
AMPLIFIERS
CAMAC
INTERFACE
PDP 15
PDP 11
BISON-NET
CDC Cyber
CRT
800 BPI
TAPE

Figure 18

controlled the transfer of the data just read out to BISON-NET. This feature enabled the off-line programs to be run on the data at all times and monitor details of the experiment, both hardware and software.

As stated before, calibration pulses were sent to the drift chamber and the LAC amplifiers between spills and the responses were read out for testing and calibration. These responses and a portion of the real data were analyzed by the on-line program and various quantities, such as pulse heights, number of hits, etc, could be displayed to monitor the equipment.

About 300 tapes were written during October and November of 1979. They included data taken with various targets and with no target present. Some straight-through beam data were also collected with the magnet on or off to align the chambers. A separate set of data with 50 Gev/c electrons was taken to calibrate the LAC. Alignment and calibration procedure and the results are presented in Chapter III.

CHAPTER III

DATA PROCESSING

In this chapter the calibration and data reconstruction procedures are described. The resolutions of the detectors obtained from these procedures are also discussed. Calibration and alignment of the drift chambers and the LAC are explained in Section A. The reconstruction of the data is presented in Section B. Run to run consistency of the data is discussed in Section C.

A. CALIBRATION AND ALIGNMENT

1. Drift Chamber Calibration and Alignment

The calibration and the alignment of the drift chambers[31] required determination of the parameters describing the electronics, drift velocities of electrons and the sense wire positions.

The calibration system for the electronics was described in Chapter II. The calibration data which were accumulated between spills and before each run were used to determine

the gain and the bias of each of the 1056 digitizer channels of LRS 2770A TDC units. The calibration involved recording the number of counts for four calibration pulses separated from each other by a known interval in time. The four points of time-count distribution were fit to a straight line. The slope of this line was called the gain and the time-axis intercept was called the bias. The mean deviation of these four points from the best fit straight line was less than 1 nsec; this corresponds to 0.05 mm in space. Therefore the contribution of calibration errors to chamber resolution was negligible.

The calibration constants mentioned above were determined separately for each data run. In Figure 19 their variation during the period of the entire run is shown for two typical channels.

In addition to these constants, the zero point in time scale, the position of each sense wire relative to a standard coordinate system and the drift velocity of the electrons in the chamber gas had to be known in order to convert the drift time intervals to coordinates in space. Beam particles were recorded with the target out and the analyzing magnet off, and their tracks were used for aligning the chambers relative to each other and the beam axis. It was assumed that all the planes were perpendicular

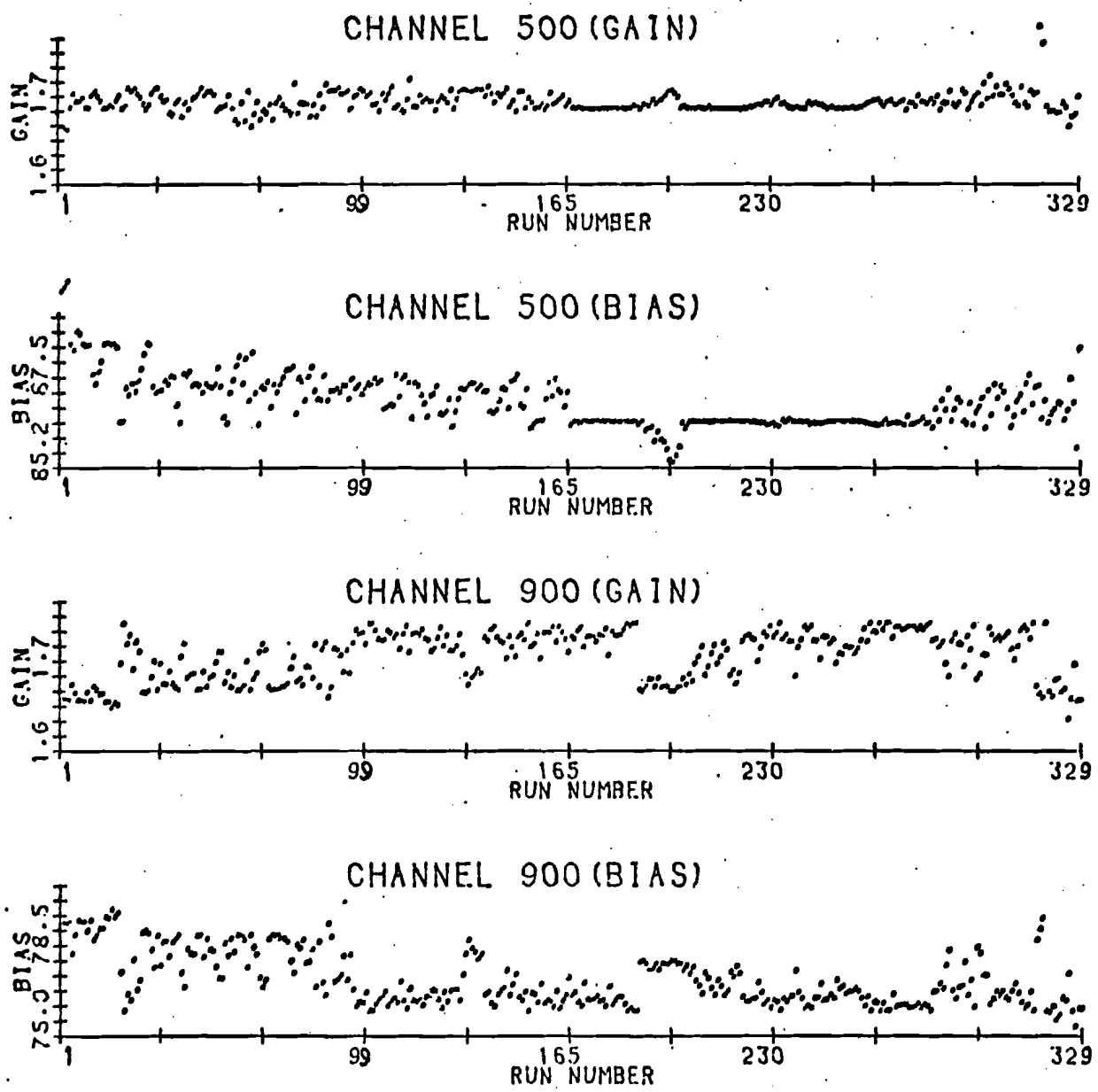
CHANNEL 500 (GAIN)
GAIN
1.6
1.7
1
99
165
230
329
RUN NUMBER
CHANNEL 500 (BIAS)
BIAS
85.2
67.5
1
99
165
230
329
RUN NUMBER
CHANNEL 900 (GAIN)
GAIN
1.6
1.7
1
99
165
230
329
RUN NUMBER
CHANNEL 900 (BIAS)
BIAS
75.0
78.5
1
99
165
230
329
RUN NUMBER

Figure 19

to the beam and the wire spacing was uniform over all planes. (During the construction and set-up of the chambers, necessary precautions were taken to validate these assumptions as well as possible. For instance, the wire spacing was accurate to +/- 0.03 mm). Therefore only one parameter, the transverse position, was necessary to know for each plane. The position of each chamber was determined temporarily with respect to a coordinate system established by the J1 and J2 chamber information. Initial estimates were made for drift velocities and time offsets from the widths and cut-off values of the time distributions.

In the next stage, the alignment parameters, drift velocities and time offsets were varied in an iterative procedure to optimize the chambers' resolutions. Finally, fixing the alignment parameters, the drift velocities and time offsets were redetermined by using the RHO trigger events. RHO trigger events covered larger area than the beam particles did and therefore the parameters determined this way were more realistic.

The results of the best fit indicated that the drift velocities were 5.13×10^{-3} cm/nsec for the chambers upstream of the analyzing magnet, and 4.90×10^{-3} cm/nsec for the downstream chambers. The small difference can be attributed partly to the fact that fewer field shaping wires were used in the downstream chambers.

The TDC times versus the positions as determined from the J1 and J2 chambers are shown in Figure 20 for upstream and downstream chambers separately. The dashed lines were obtained assuming a linear relationship between time and distance with the above velocities. Except near the edge of the drift cell, ~1 cm away from the sense wire, the linear approximation seems to be valid to within 0.2 mm.

Using the data for $K^+ \rightarrow \pi^+\pi^0$ the average resolution of the chambers were determined to be σ =0.18 mm (standard deviation per plane) for the tracks outside the beam region and σ =0.26 mm for the tracks in the beam region, a cylindrical region with radius 0.75 cm. The resolution was worse in the beam region because the larger space charges modified the electric field there. This was not a serious problem since in most of the data the charged tracks were located outside of the beam region (See Figure 32).

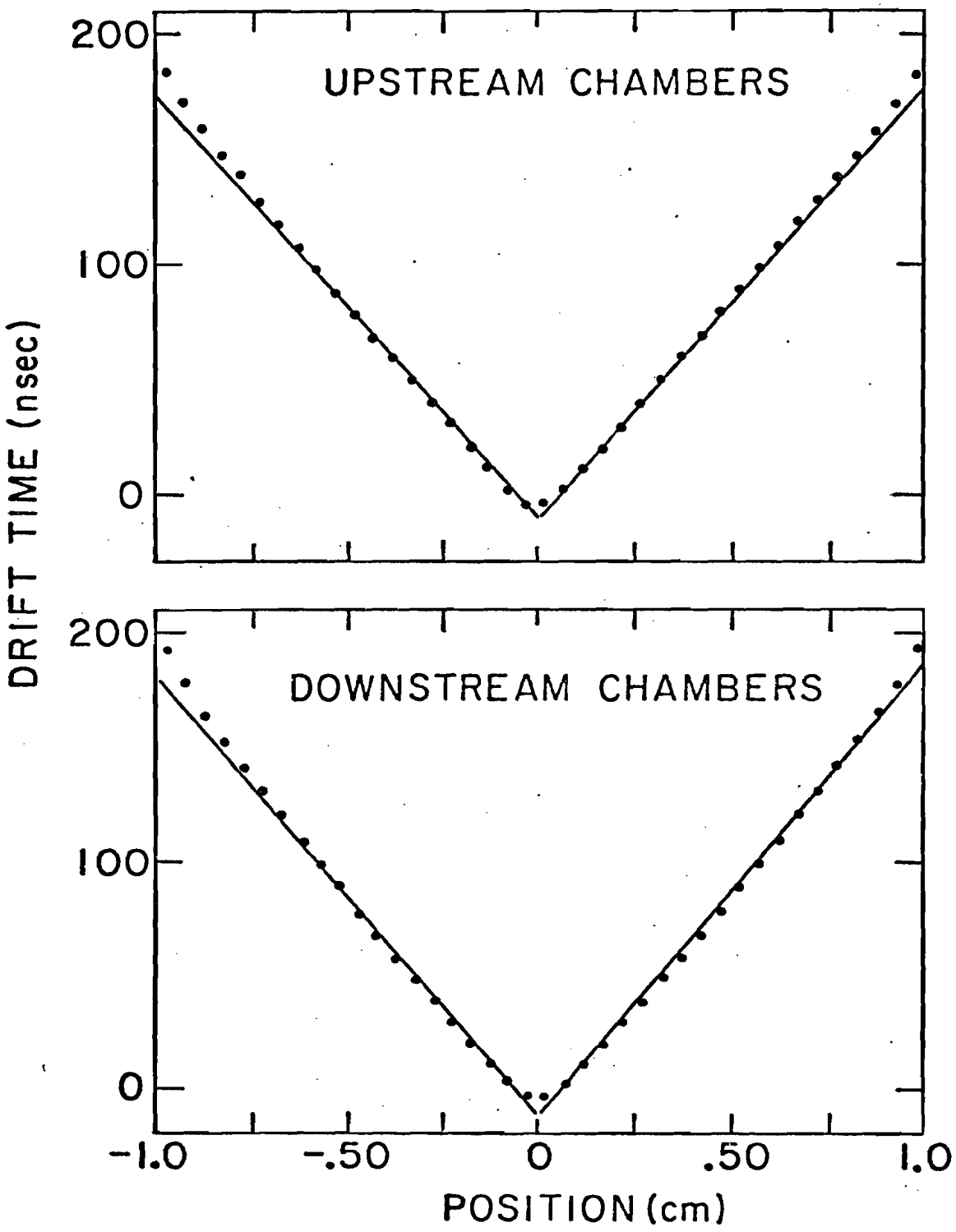
UPSTREAM CHAMBERS
DOWNSTREAM CHAMBERS
DRIFT TIME (nsec)
200
100
0
200
100
0
-1.0
-.50
0
.50
1.0
POSITION (cm)

Figure 20

2. LAC Calibration and Alignment

Calibration procedure of the LAC involved determining two types of constants. First, electronic pedestals and gains, as defined to the response of the amplifiers to the calibration pulses, had to be known for each run; second, factors that convert the digital counts to the energies for each channels had to be determined.

The pedestals and the gains were measured and recorded between spills during data taking. For every run, average values of the pedestals for each channel were determined from these records and subtracted from ADC counts. The pedestal levels varied with event rates. This variation amount was determined as a function of beam intensity and a correction for this effect was applied to the channels around the beam hole where the event rate was higher.

An attempt was made to apply a correction for time variation in amplifier gains. It was realized that the gains fluctuated by less than 2% over the course of the experiment and the attempt made very little if any difference. The run by run correction for π^0 mass (see Section C) which indicated the variation in the gain of the whole system, was more significant.

The conversion factors were dependent on physical characteristics of the channels such as their capacitances, equivalent resistances, the amplifiers connected to them, argon purity etc. A 50 Gev/c negative beam was used to determine these factors for each channel which represented the absolute gain of the LAC system. The electrons in the beam were tagged by the K1 Cerenkov counter. They were bent by the magnet BM109 to determine their energies which were then compared with the energy read out by the LAC. Several scans, both in X and Y directions, were done. The X-scans for two different Y coordinates were obtained by moving the detector on air pads along the X direction. The Y-scans for two different X coordinates in left and right portion of the detector were made possible by sweeping the beam vertically using the dipole magnet E1PM (see Figure 5).

The procedure to determine the conversion factors from these data can be outlined as follows:

First, the unwanted events, like pions that were misidentified as electrons by the Cerenkov counter and electrons that emitted a photon (Bremsstrahlung effect) before hitting the LAC, had to be eliminated. About 16% of the data were discarded this way. The rest of the data were used to minimize the quantity $\sum_i (E_i^0 - E_i)^2$, where the summation was over all events. In this expression E_i^0 was a

reference energy (see below) and E_i was the energy measured by the LAC for the ith event. E_i was taken to be

$$E_i = \sum_j a_j n_i^j$$

where a_j was the conversion factor for the jth channel, and n_i^j was the number of ADC counts recorded by that channel after pedestal correction.

This procedure could have been followed for X or Y views in the front or back portion of the detector. But, for the photon or electron events , the typical energy deposition at the back of the detector was about 13%. Therefore the factors for the back half of the LAC were neither crucial nor practical to determine on a channel by channel basis. A constant value a_j^B =13 Mev/count was assigned to the back factors. It was determined, by iteration and along with the calculation of the front factors, for the best overall energy resolution.

To determine the front factors, five channels around the shower maximum were added to calculate E_i. E_i^0 was taken to be $(P_i/2 - E_i^B)$ with P_i being the electron momentum and E_i^B being the energy at the back of the detector. E_i^B was calculated as E_i above, but the conversion factors a_i^B were taken to be the constant 13 Mev/count for the reasons explained before.

Determining the front factors took a number of iterations of the minimization. For the beginning, the back factor of 13 Mev/count was substituted for every front channel. Running the calibration program on the data for X, Y-right, Y-left scans individually replaced the old factors for the corresponding coordinate with the newly determined ones in the front half. The final conversion factors are shown in Figure 21. The central (beam region) factors were ~20% higher than the rest; the special amplifiers in the beam region were modified to have shorter decay time to prevent the saturation in this high rate region (see Chapter II.D). This modification changed their gains. The central back factors were also assumed to be larger by 20%.

The parameters in the energy and position algorithms used to reconstruct the real data events (Section B) were obtained by studying the 50 Gev/c electron data with these factors.

The response of the LAC to the electrons as a function of their momenta was studied by using Ke3 ($K^+ \rightarrow \pi^0 e \nu$) decay electrons. Figure 22a shows the energy registered by the LAC for electrons of various momenta. The electron momenta were measured by the drift chambers and the analyzing magnet. The linearity of the response is better

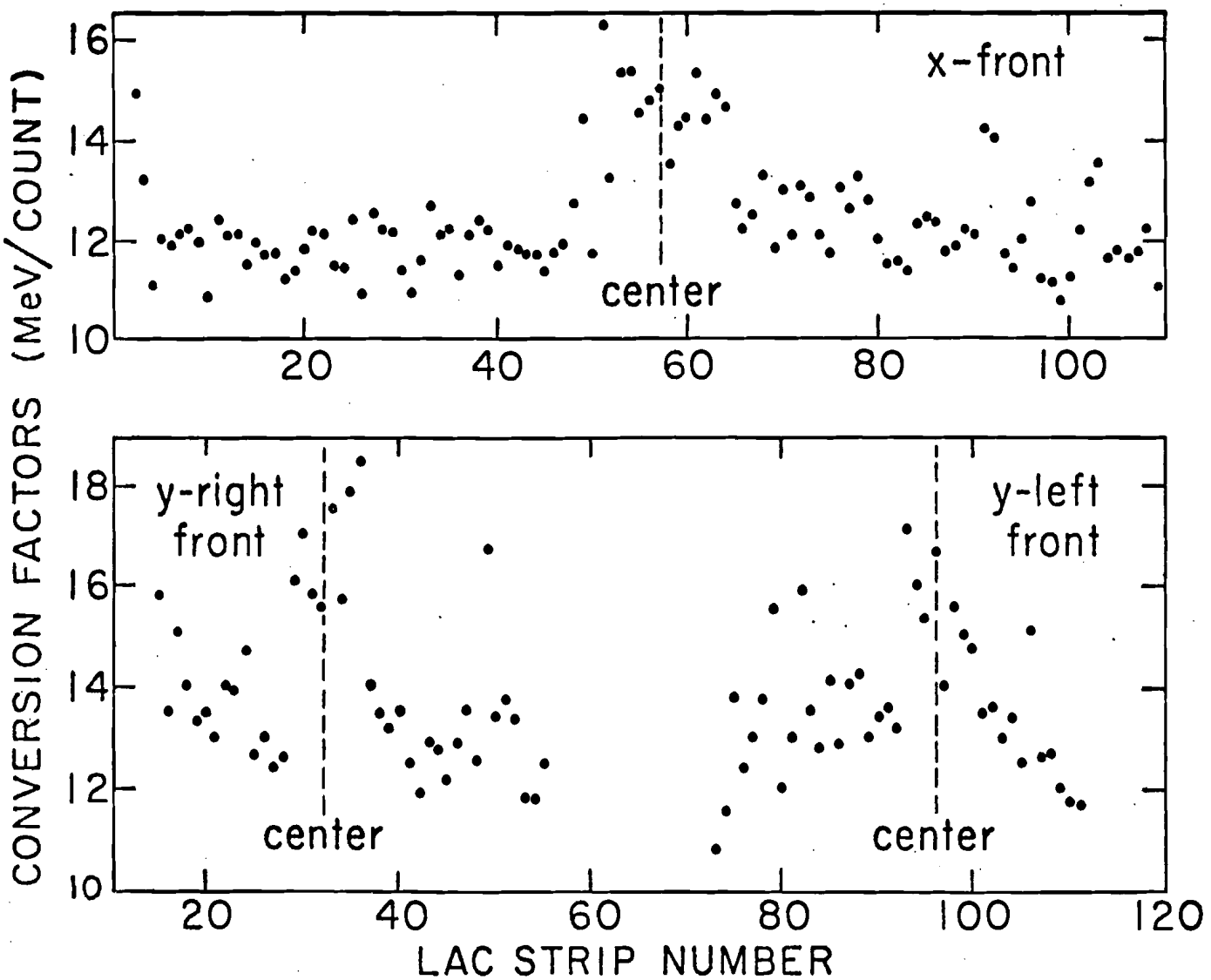
CONVERSION FACTORS (MeV/COUNT)
x-front
center
y-right front
y-left front
center
center
LAC STRIP NUMBER

Figure 21

than 5% over the momentum range from 20 Gev/c to 80 Gev/c. The energy resolution is presented in Figure 22b. The dashed line indicates a resolution relation of the form of $\sigma^2 = a + bE$ with a=0.2 Gev^2 and b=0.0196 Gev.

The same data were used to determine the position resolution and to align the detector with respect to the rest of the spectrometer. In Figure 23a we show the distribution of the difference between the centroid of the energy shower in the LAC and the position of the electron determined by extrapolation of the track from the drift chambers. Assuming the drift chamber position resolution to be +/- 0.2 mm, the data on Figure 23a indicated a position resolution in the LAC of better than 1 mm (standard deviation per projected coordinate). The centroid of the distribution gave the LAC position relative to the other equipment.

The π^o mass distribution from the decay $K^+ \rightarrow \pi^+\pi^o$ was another indicator to the LAC performance. Figure 23b shows the mass spectrum of two photons from the π^o meson of these events. The origin of the π^o was the vertex of the K^+ decay and determined as the point where the trasverse distance between the beam (incoming K^+) and the outgoing charged particle (π^+) trajectories was minimum. Each photon was required to have an energy greater than 5 Gev. A gaussian

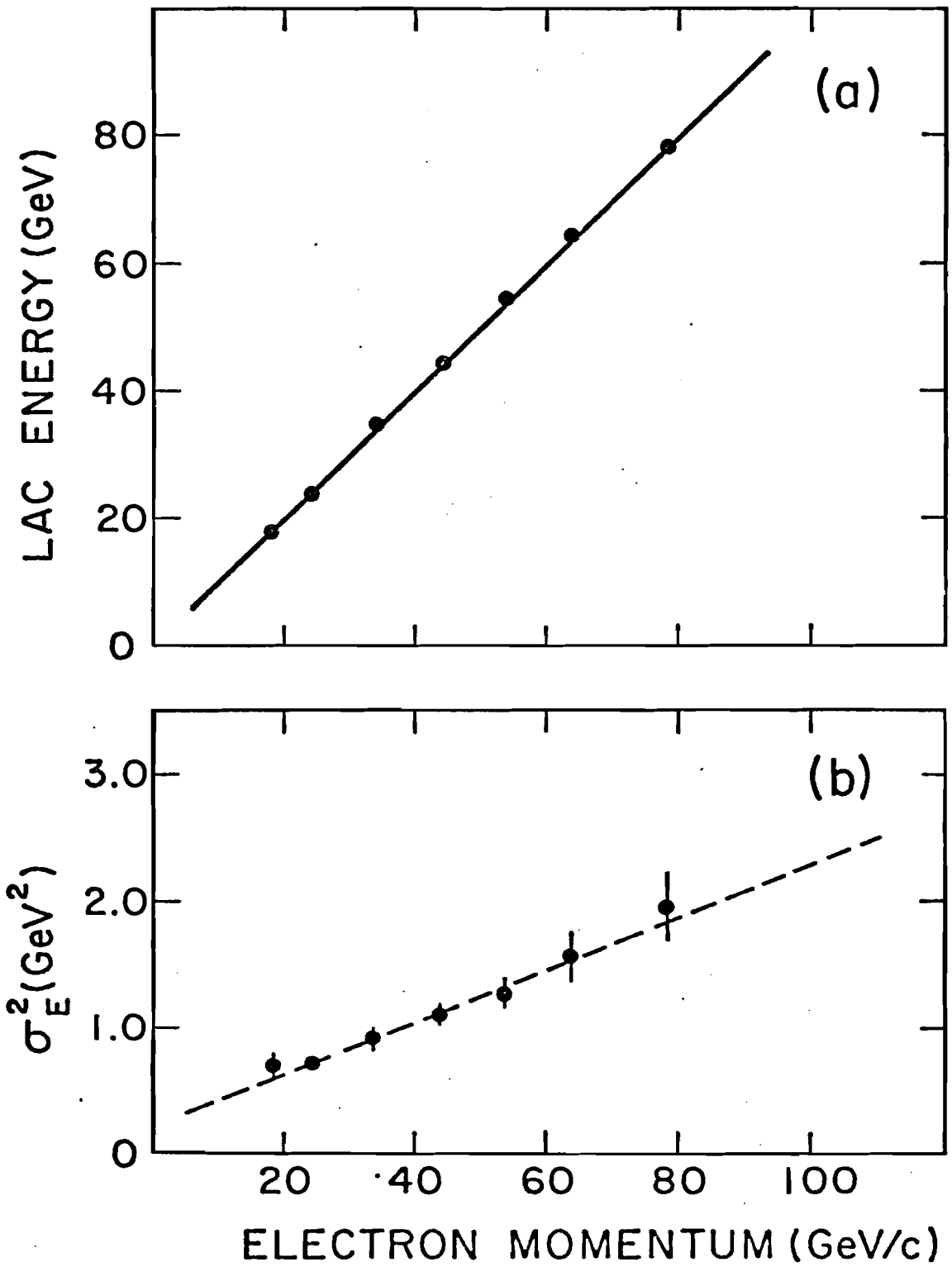
(a)
LAC ENERGY (GeV)
0
20
40
60
80
(b)
σ_E^2(GeV^2)
0
1.0
2.0
3.0
20
40
60
80
100
ELECTRON MOMENTUM (GeV/c)

Figure 22

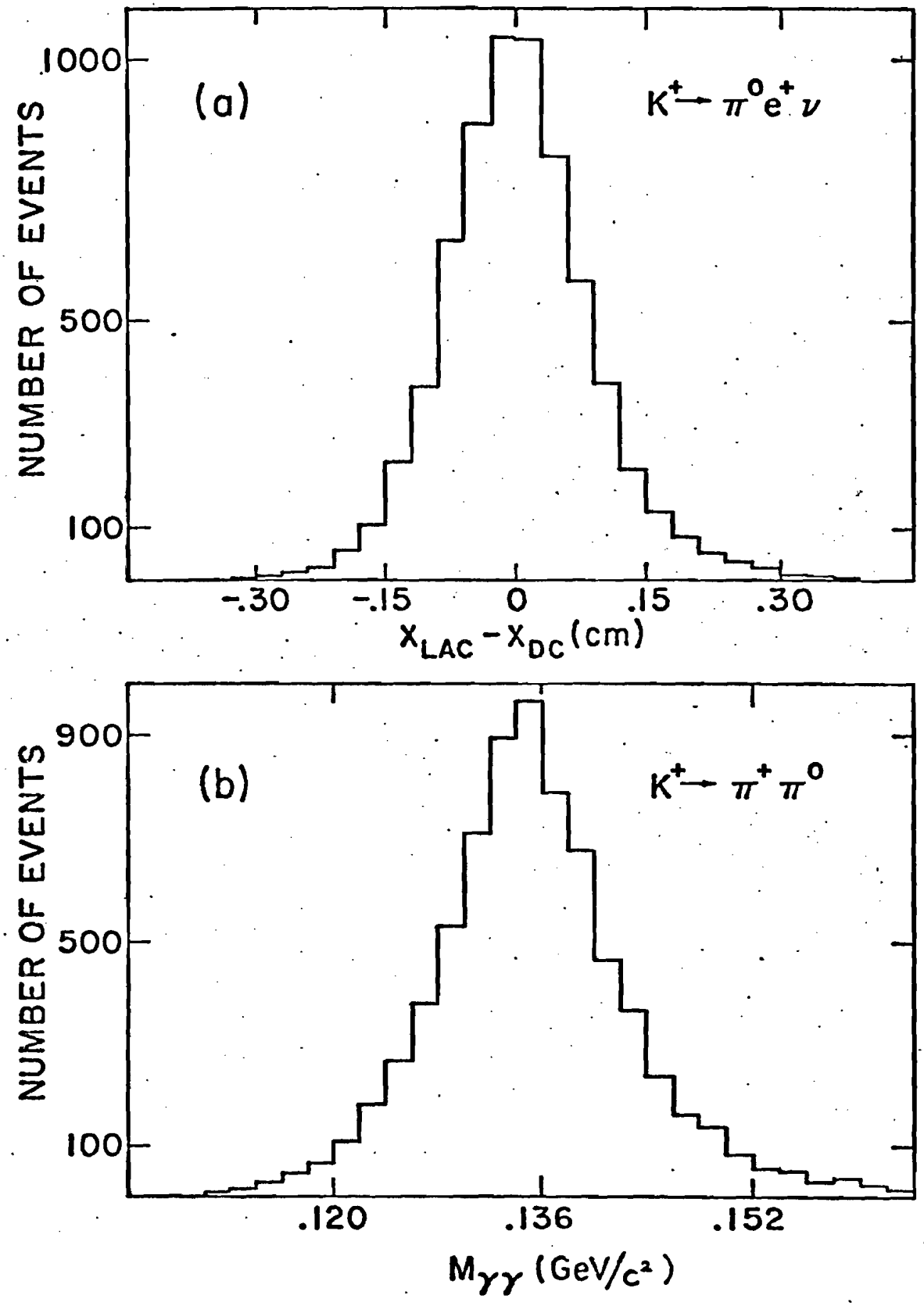
(a)
$K^+ \to \pi^0 e^+ \nu$
NUMBER OF EVENTS
1000
500
100
-.30
-.15
0
.15
.30
$X_{LAC} - X_{DC}$ (cm)
(b)
$K^+ \to \pi^+ \pi^0$
NUMBER OF EVENTS
900
500
100
.120
.136
.152
$M_{\gamma\gamma}$ (GeV/c^2)

Figure 23

fit to the distribution in Figure 23b indicated a π^0 mass resolution of 7 Mev/c^2.

The electromagmetic shower shape obtained from 50 Gev/c electrons is shown in Figure 24 together with the hadronic shower shape for comparison. It was determined later by using photons with various energies that the electromagnetic shower shape was independent of energy within 3-5%. The shower shape was used in the reconstruction program to separate overlapping photons from each other.

The response of the detector to hadrons was investigated by using the π^-'s from the decay $K^+ \rightarrow \pi^+\pi^+\pi^-$. Since they were bent by the analyzing magnet in opposite direction with respect to π^+'s and there were no photons in the decay, the π^-'s were isolated from any other particles. It was determined that ~36% of the hadrons did not interact with the LAC at all. The relative energy distribution (LAC energy/momentum) of the interacted hadrons with energy deposition of greater than 5 Gev is shown in Figure 25a. Figure 25b shows the distribution in the ratio of the energy deposition in the back of the LAC to the total LAC energy, both for hadrons and electrons. As seen from it, hadrons interacted mostly at the back of the detector. The requirement of having less than 20% of the energy at the back distinguished electrons and photons from hadrons. This

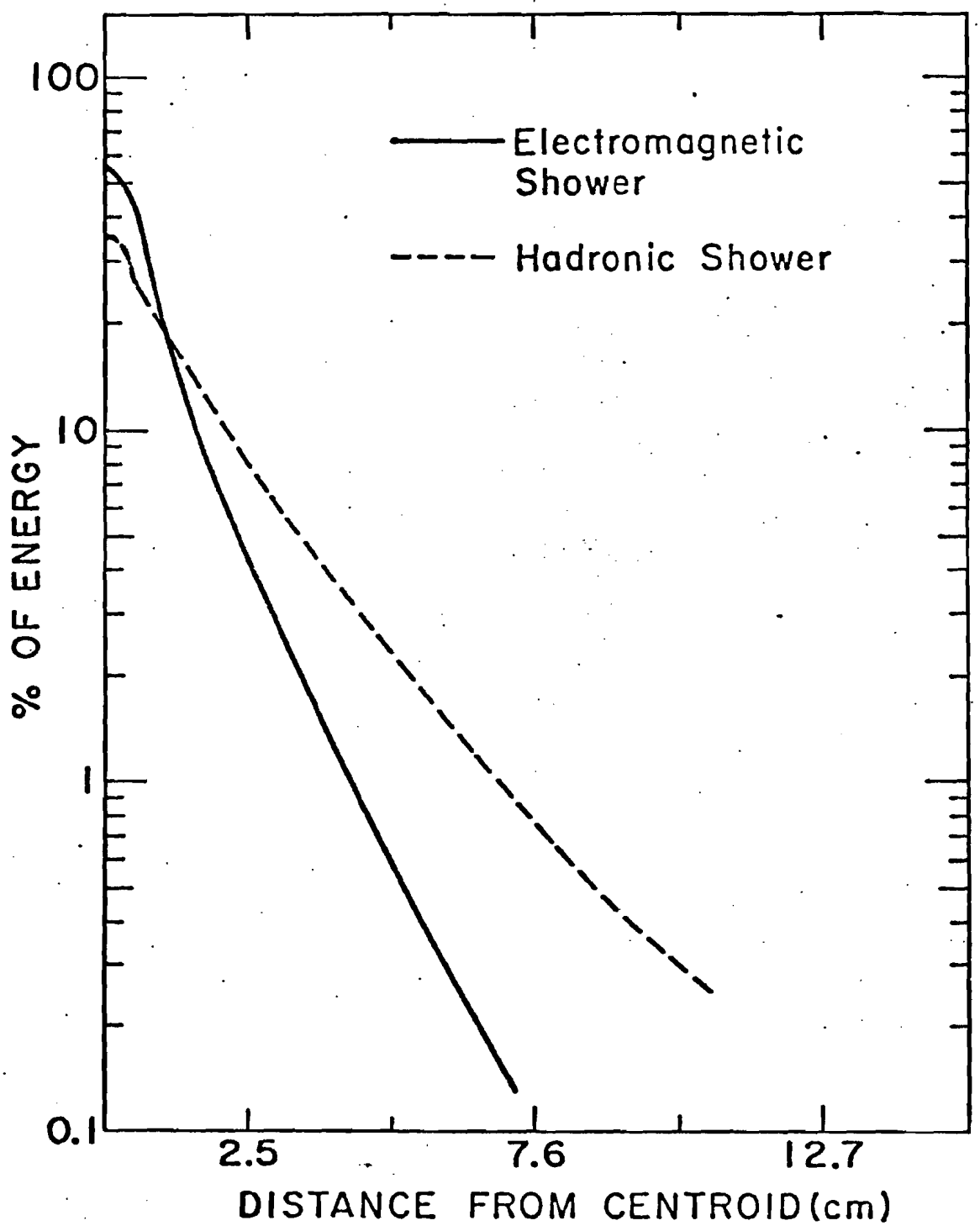
100
10
1
0.1
% OF ENERGY
Electromagnetic Shower
Hadronic Shower
2.5
7.6
12.7
DISTANCE FROM CENTROID (cm)

Figure 24

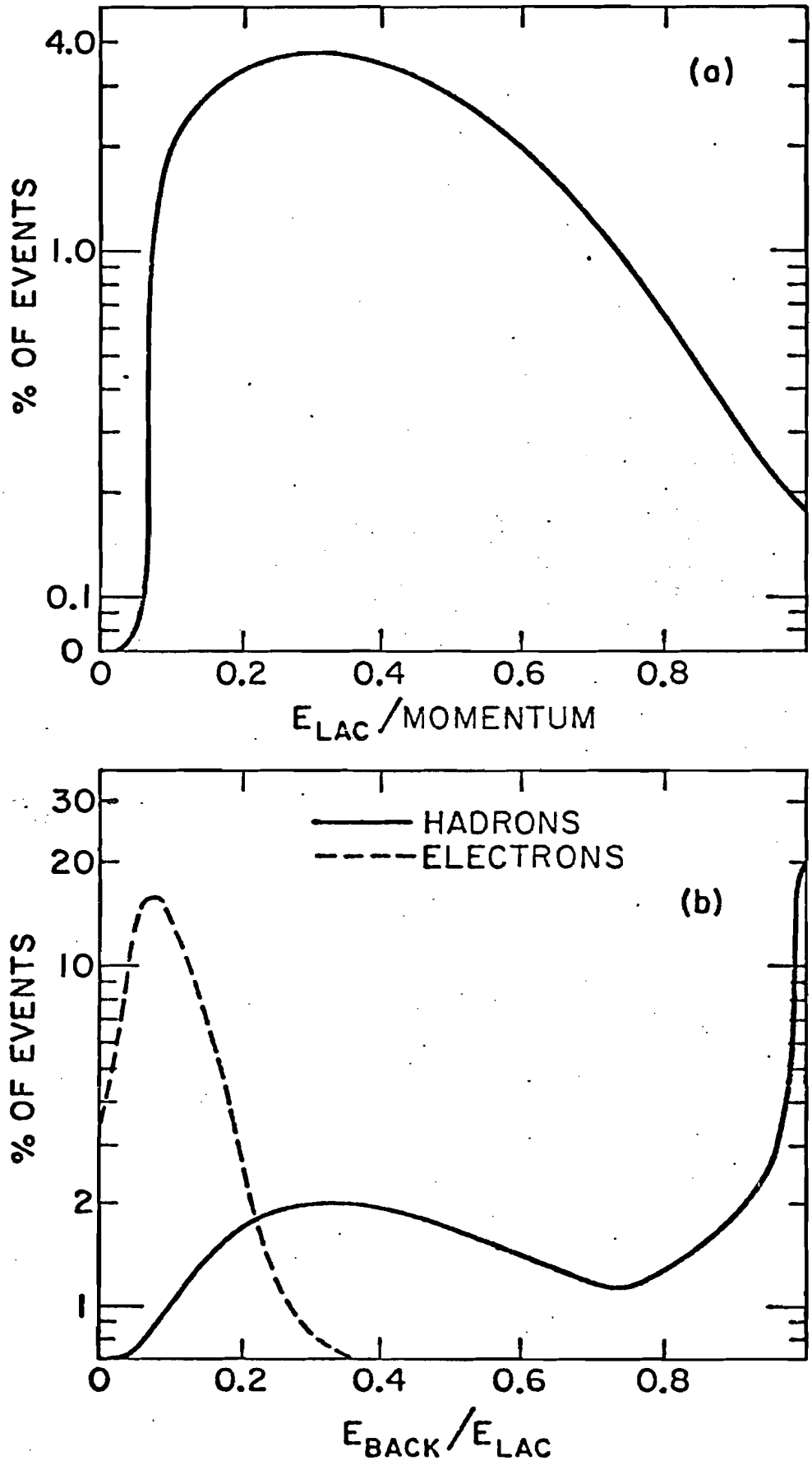
4.0
1.0
0.1
0
% OF EVENTS
(a)
0
0.2
0.4
0.6
0.8
E_LAC /MOMENTUM
30
20
10
2
1
% OF EVENTS
HADRONS
ELECTRONS
(b)
0
0.2
0.4
0.6
0.8
E_BACK/E_LAC

Figure 25

information and the hadronic shower shape obtained from this study were used to simulate the response of the detector to hadrons in a Monte Carlo model of the experiment (see Chapter IV).

The distribution of the difference between the positions as determined by the LAC and the drift chambers, X(lac)-X(dc), for the hadrons is shown in Figure 26 and to be compared with the same distribution for the electrons in Figure 23a. As seen from the Figure 26, the position resolution of the LAC for the hadrons was better than 1 cm.

B. DATA RECONSTRUCTION

Raw data as recorded on magnetic tapes by the on-line program were processed to determine the positions and energies of various particles that were detected. The main aspects of this process is presented below.

1. Charged Track Reconstruction

In Section A we described the determination of the calibration constants of the drift chamber system. As a first step of charged track reconstruction, these constants were used to convert the digital data from drift and

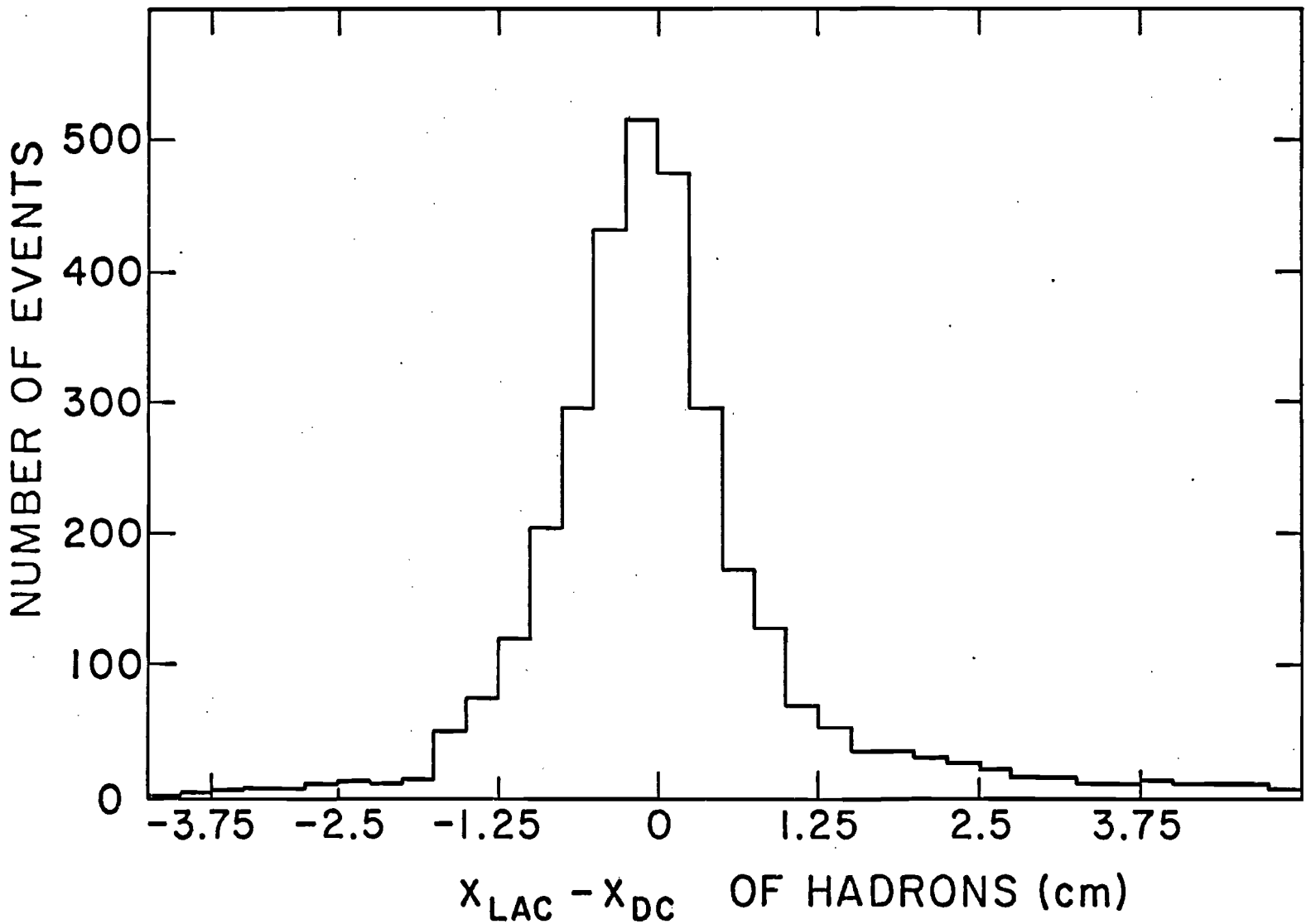
NUMBER OF EVENTS
500
400
300
200
100
0
-3.75
-2.5
-1.25
0
1.25
2.5
3.75
$X_{LAC} - X_{DC}$ OF HADRONS (cm)

Figure 26

proportional chambers to spatial coordinates. At this stage, because of the left/right ambiguity, there existed two equally likely coordinates for each hit in a drift chamber.

Using the hits from P2, D3 and D4 chambers, a search for tracks downstream of the magnet was initiated. After finding hits in the X and U projections, hits in the V projection were predicted and searched for. When a predicted hit was found, all hits were fitted to a straight line. (A hit in a projection was considered to exist if at least one of the pair of staggered planes in that projection had a hit). All possible combinations for which all hits were within 1 mm of the fitted line were considered, and the fit with the best χ^2 was chosen as the initial downstream track segment.

Next, the upstream track segment was searched for. The analyzing magnet BM109 deflected the charged particles horizontally and its magnetic field was very uniform. Therefore, the trajectory of a charged particle passing through the magnet could be approximated by two straight line segments that intersected at the center of the magnet and had the same vertical slope. This approximation provided a starting point for the search for the upstream segment of the track. Another point, hence X-slope, was provided by the hits found in P1 chamber. At this point of

the procedure, than, an initial track hypothesis for the whole trajectory was defined by five parameters; X and Y coordinates of the center of the magnet, the Y-slope that was common to both upstream and downstream segments, and the X-slopes to those segments.

Before the next stage of the reconstruction, a weight

$$W_i = \exp[-(r_i - r_o)^2 / 2\sigma^2]$$

was calculated for each hit, including the ambiguities, which fell within 4 mm radius of the initial track hypothesis. In this expression, $(r_i - r_o)$ was the distance between the hit and the track hypothesis and σ was equal to 6.4 mm initially. Then, an iterative fitting procedure was carried out, in each time the σ was reduced by a factor of 3/4 , a new set of parameters were determined and the hits with bad W_i were thrown away. The left/right ambiguities in each pair were resolved by eliminating the hit that had the smaller weight. The search radius was reduced from 4 mm to 1 mm and a final fit was performed to define a single track.

The beam trajectory was calculated by using the hits from the beam chambers J1 and J2. During the analysis, the vertex of the interaction was defined to be the point where the beam track and outgoing charged particle track trajectories were closest to each other. The efficiency of

combining a K^+ beam track of a $K^+ \rightarrow \pi^+\pi^0$ decay with the outgoing π^+ track was greater than 95%. About 1% of the tracks were lost because of the inefficiency in the chambers and the rest of the losses was due to the tight requirement for finding the downstream trajectories.

2. Photon Reconstruction

The positions and the energies of the photons were calculated by the gamma reconstruction program. The raw data contained counts for any of the 480 channels. The pedestal levels were subtracted in each channel and the results were multiplied by appropriate conversion factors to determine the energy deposited in each channel. A minimum energy of 450 Mev was required to be registered in any channel for further considerations.

During the initial reconstruction stage, the X and Y views were treated separately. First, groups of peaks and valleys were searched for in the front half of each view. Using the information about the shower shape, each peak in a group was separated from others to form "gamma"s. The energies and the positions of these gammas were calculated by a three channel algorithm in the following way: The pulse heights P1, P2 and P3 around the peak (P2 being the peak) were used to calculate the energy

for that gamma using the expression

$$E=a[P1+P2+P3+b(P1+P3)]$$

The constants a and b were determined emprically using the calibration data. The position of the same gamma was determined from the formula

$$X=X0 + [C_1+C_2A + (C_3+C_4A)]$$

with $A=(P3-P1)/P2 - C_5$ and X0 being the position of the center of the peak channel strip. The constants C_1, C_2, C_3, C_4, C_5 were also determined from the calibration data. Gammas with energies in one view less than 2.4 Gev were not considered in the later stages.

The next step was to correlate the gammas in the two views to make photons. For correlation, the criteria was the difference in energies of the two views. Since the LAC was finely segmented in the Z-direction and the X and Y planes were interleaved, one could expect the energy in X view, E_x, to be almost equal to the energy in Y view, E_y. Therefore, for the correlation, the quantity

$$|E_x-E_y|/(E_x+0.5+0.03E_x^2)^{1/2}$$

was required to be less than a threshold which was increased in each of several searches. In each turn of the search, the correlated gammas were removed from consideration for the next search.

In some cases, two showers were separated in one view

but overlapped in the other. The single peak in the overlapping view was split if this improved the overall fit.

After all the possible correlations were made, the energies in both views and the corresponding back energies that were calculated by another three channel algorithm, were added to form the photon energies. The photon positions were assigned as the positions of the gammas which were determined only from the front part of the LAC. Before the results were written into summary tape , the photon positions were compared with the extrapolated charged track positions on the LAC. The ones that matched up with the charged track within 2.5 cm were called "photon-charged overlaps" as canditates for electrons or interacting hadrons. The ratio of the back to front energy determined whether such a particle was called a hadron or an electron.

C. RUN TO RUN CONSISTENCY

As each raw data tape was processed, the reconstructed energies , positions and charged track trajectories, along with a copy of the raw data, were written into a summary tape. During this processing, various quantities were examined for each run to ensure that the apparatus worked well and consistently throughout the experiment.

The chamber efficiencies and scaler rates were studied for each run to check for potential troubles. A good overall test of the apparatus was provided by the decays $K^+ \rightarrow \pi^+\pi^0$ and $K^+ \rightarrow \pi^+\pi^+\pi^-$ which topologically resemble the decays (8) - (11). The number of these decays on each processed tape was sufficient to obtain a run to run comparison accurate to +/- 10%. The runs that had a statistically significant low rate of these decays were left out from further analysis. This way, seven tapes, which were mostly test runs, were eliminated. The behaviour of the LAC was monitored by the π^0 mass. The average value of the reconstructed π^0 mass from $K^+ \rightarrow \pi^+\pi^0$ decays of each run is plotted on Figure 27 with error bars on a few typical points. The 1-2% fluctuation did not look too serious. Therefore, empirical and run dependent correction factors were applied to the data to compensate for the fluctuations.

The degree of accuracy of the calibration and the reconstruction is reflected by the resolution of the spectrometer and the agreement between the real data and predictions of a Monte Carlo model which is made up according to the knowledge of the experiment. This subject is discussed in the next chapter.

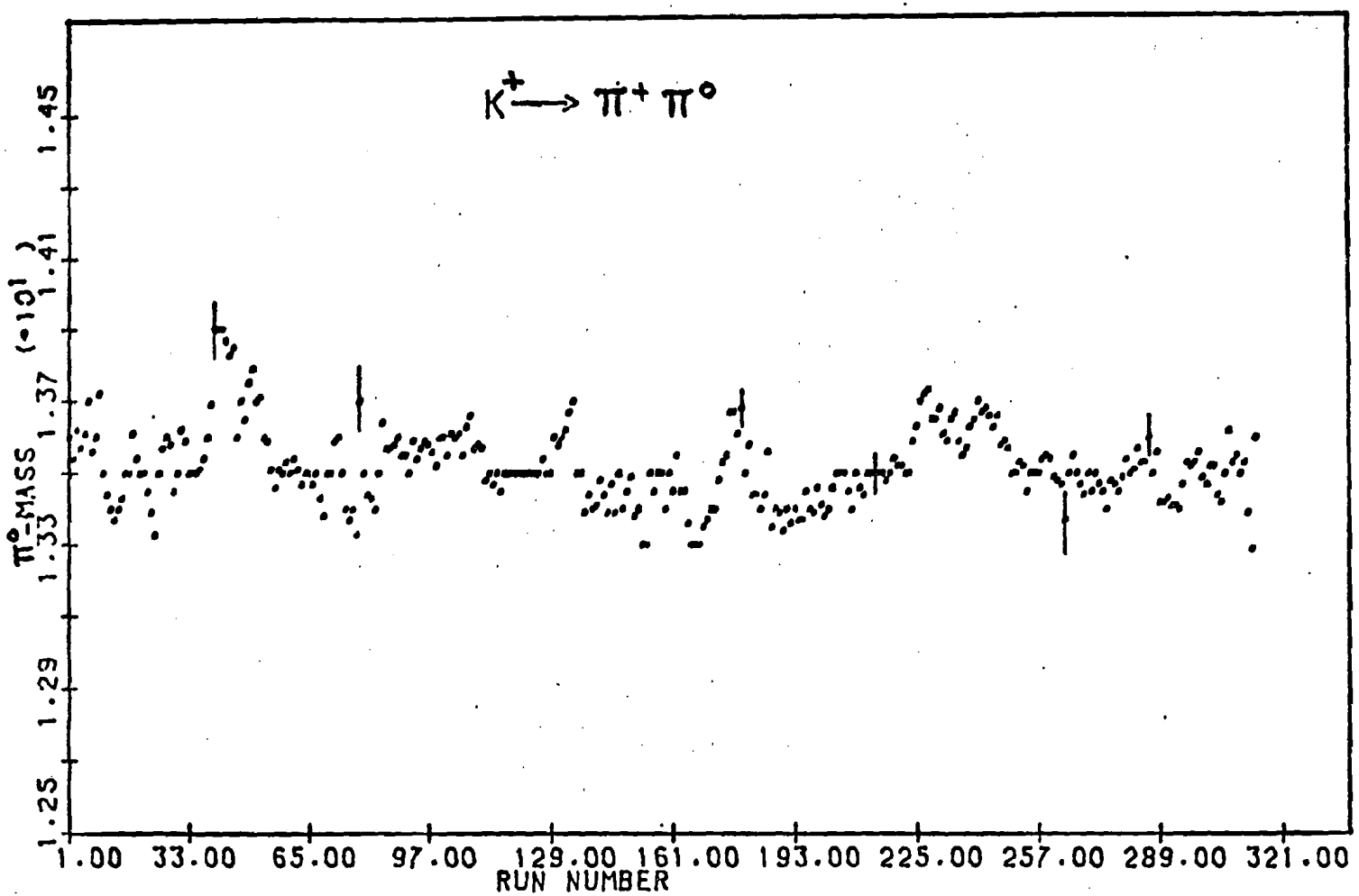
$K^+ \longrightarrow \pi^+ \pi^0$
π^0-MASS $(\cdot 10^1)$
1.25
1.29
1.33
1.37
1.41
1.45
1.00
33.00
65.00
97.00
129.00
161.00
193.00
225.00
257.00
289.00
321.00
RUN NUMBER

Figure 27

CHAPTER IV

RESOLUTION AND MONTE CARLO MODEL

The performance of the spectrometer as a whole is discussed in this chapter. A Monte Carlo model of the experiment is described and various measured quantities are compared with the predictions of this model.

A. MONTE CARLO MODEL

In order to obtain information about the geometrical and trigger related acceptance factors, a Monte Carlo model of the spectrometer was constructed and used to generate events of the reactions under study. Its parameters were determined from and adjusted to the real data as follows:

1) The angular divergence, the transverse dimensions and the focus of the beam were determined from the reconstructed beam tracks.

2) The transverse positions of the counters BA, BV and VE were determined from the sharp cutoffs seen in spatial distributions of the charged tracks at the Z-positions of these counters.

3) The logic signals MBV2 and TC were simulated by generating signals for proportional chambers. The efficiencies and noise levels of the chambers as determined from the real data were imposed onto the generated signals.

4) The behaviour of the various counters as observed from the real data were simulated.

5) The multiple Coulomb scattering of the charged particles passing through the target was simulated by using the Gaussian approximation for this effect.

6) Using the known angular resolution of +/- 0.04 mrad of the drift chambers, a Gaussian error was imposed on the charged track trajectories.

7) The magnetic field value and effective length of the analyzing magnet BM109 were determined from the real data. The magnet aperture limits were established by studying the cutoffs in the distributions of reconstructed charged tracks at the Z-positions of the both ends of the magnet. Similarly, the edges of the chambers were determined and implemented in the Monte Carlo.

8) The photon energies for front and back portions of the LAC were distributed to the channels according to the

shower shape that was obtained by the LAC calibration. The ratio of front to back energies was chosen to have the same distribution as in the real data. The energy in each channel was smeared by using the energy resolution determined from the real data (Chapter III) and a random energy level was added to simulate amplifier noise.

9) To simulate the LAC logic, E(up), E(down) and E(tot) were calculated the same way as in the experiment and the requirements for the minimum energy and energy on opposite side of the charged track trajectory were imposed.

10) The hole in the center of the LAC was simulated by rejecting any photon hitting at actual hole coordinates. The energy leakage of photons impinging near the hole was also simulated.

11) The effects of hadron interactions with the LAC were introduced into the Monte Carlo model, simulating the distributions described in Chapter III.

12) A random noise in the LAC due to the beam, as observed in the real data, was also simulated.

Events that were generated by this Monte Carlo model were processed by the same reconstruction program as the

real data. They could then be compared with the real data by analyzing them with the same kinematics program. The next section presents the results of these comparisons. The solid curves in the figures are the Monte Carlo predictions, normalized to the number of events in the histogrammed distributions of the real data.

B. SPECTROMETER RESOLUTION

1. K^+ Decays

As stated earlier, the decays $K^+ \rightarrow \pi^+\pi^0$ and $K^+ \rightarrow \pi^+\pi^+\pi^-$ resembled the reactions of interest. Large statistics data were available on these well established decays. Consequently, the behaviour of the spectrometer for these reactions was a good indicator of the quality of the experiment. In this section, a detailed comparison is made between data obtained on the above decays and with Monte Carlo model predictions. Agreement between measured and predicted quantities is essential to show the accuracy of the Monte Carlo model and our level of understanding of the spectrometer.

The decay $K^+ \rightarrow \pi^+\pi^0$ was topologically identical to the RHO trigger mode Reactions (8) and (10). This decay is

defined primarily by the existence of one charged track and two photons. The kaon, before it decayed, was identified by the K1 Cerenkov counter. To ensure that only free kaon decays were being considered, we required that the decay vertex, the intersection of the incoming K^+ track and the outgoing π^+ track, occures inside the decay pipe downstream of the target. Other requirements, like correct total energy, π^0 and $\pi^+\pi^0$ mass values, further defining the decay are discussed below.

The $K^+ \rightarrow \pi^+\pi^+\pi^-$ decay resembled the Reactions (9) and (11). Both A1 and VEE triggers were sensitive to this decay. The data collected with VEE trigger was then used to study the behaviour of the spectrometer for the Reactions (9) and (11).

2. Monte Carlo Comparisons

Figures 28a and 28b show the vertex distributions for the K^+ decays. The Monte Carlo distributions are shown for the intervals in which the real decays were selected. The falloff at the downstream end of the decay pipe was primarily due to the MBV2 requirement in the triggers. Losses near the origin (target area) were caused by the target vetoes and (especially in $K^+ \rightarrow \pi^+\pi^+\pi^-$) by the S and H counters. To avoid the problems that might be

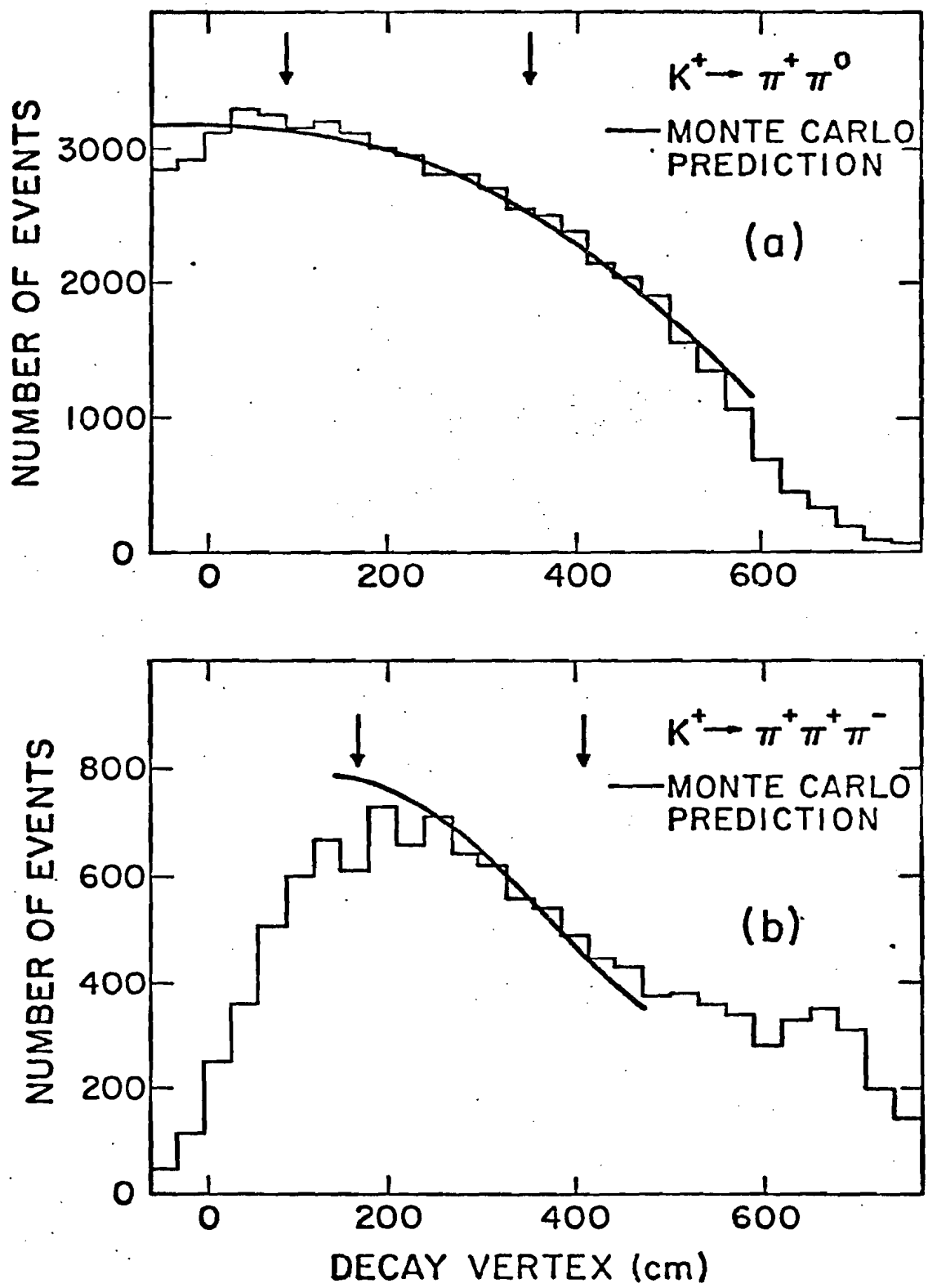
$K^+ \to \pi^+ \pi^0$
MONTE CARLO PREDICTION
(a)
NUMBER OF EVENTS
3000
2000
1000
0
0
200
400
600
$K^+ \to \pi^+ \pi^+ \pi^-$
MONTE CARLO PREDICTION
(b)
NUMBER OF EVENTS
800
600
400
200
0
0
200
400
600
DECAY VERTEX (cm)

Figure 28

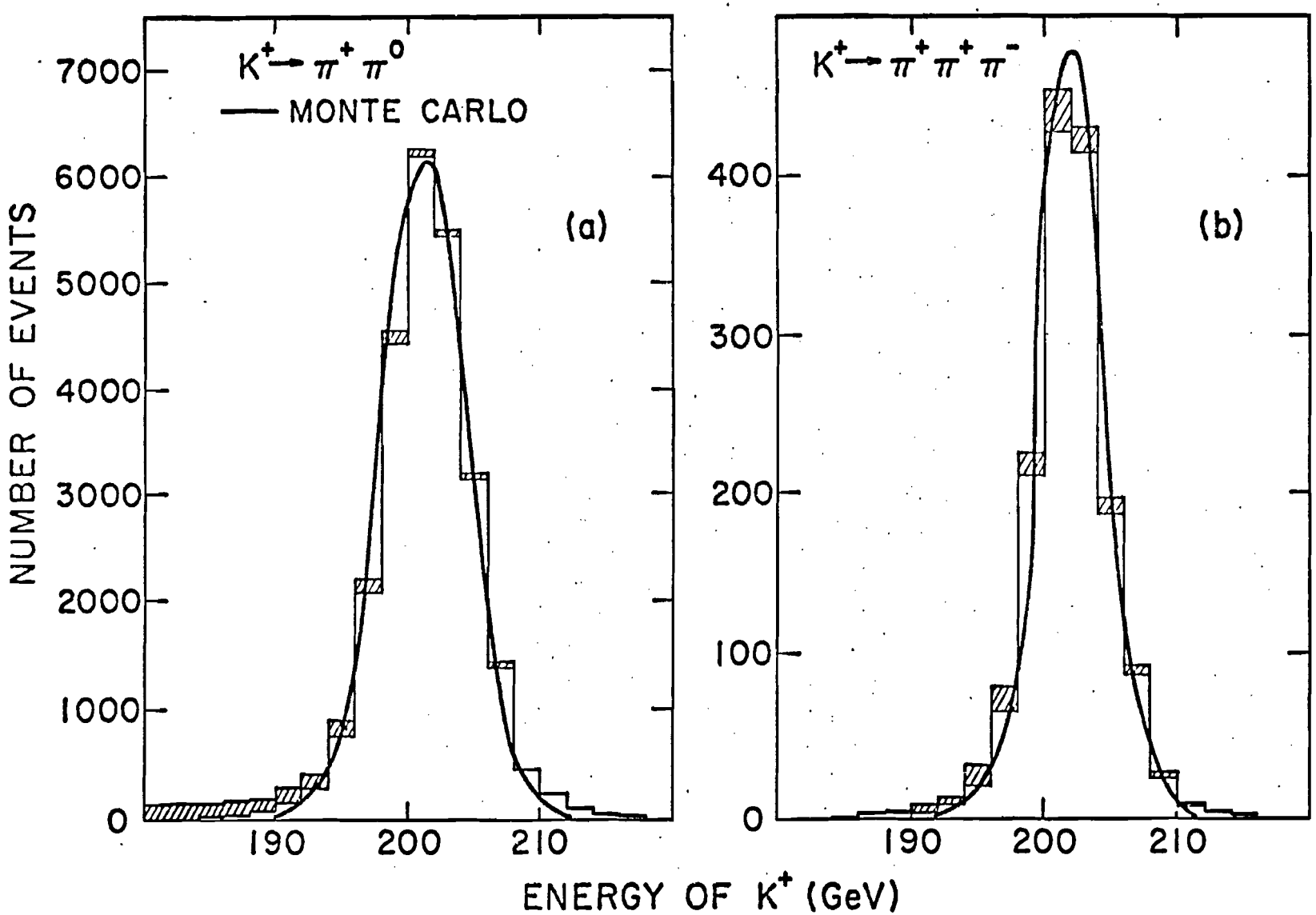
$K^+ \to \pi^+ \pi^0$
MONTE CARLO
(a)
$K^+ \to \pi^+ \pi^+ \pi^-$
(b)
NUMBER OF EVENTS
7000
6000
5000
4000
3000
2000
1000
0
400
300
200
100
0
190
200
210
190
200
210
ENERGY OF K^+ (GeV)

Figure 29

associated with these signals, only data with a vertex between 90 cm and 340 cm downstream of the target were used in the $K^+ \rightarrow \pi^+\pi^0$ decay. For the $K^+ \rightarrow \pi^+\pi^+\pi^-$ decay the vertex cut was between 140 cm and 400 cm. These cuts are indicated by arrows in the Figures 28a and 28b.

The total energy distributions for these decays are shown in Figures 29a and 29b. If the $\pi^+\pi^0$ mass and $\pi^+\pi^+\pi^-$ mass were restricted to be between 0.46 Gev/c^2 and 0.54 Gev/c^2, the events in the shaded region would be removed. These low energy events in the $K^+ \rightarrow \pi^+\pi^0$ distribution were mostly $K^+ \rightarrow e^+\pi^0\nu$ decays with missing ν-energy, and in the $K^+ \rightarrow \pi^+\pi^+\pi^-$ distribution were $K^+ \rightarrow \pi^+\pi^0$ decays followed by $\pi^0 \rightarrow e^+e^-\gamma$, with γ not detected. The arrows indicate the limits used for the total energy to define the decays.

The 2-photon mass distribution as obtained from the $K^+ \rightarrow \pi^+\pi^0$ decays is shown in Figure 30. As stated in Chapter III, the photons had an energy of at least 5 Gev. The mass resolution is 7 Mev/c^2. The arrows indicate the limits used for 2-photon mass cuts for further analysis.

The $\pi^+\pi^0$ and $\pi^+\pi^+\pi^-$ mass distributions are shown in Figures 31a and 31b. The cuts on the total energy and on the

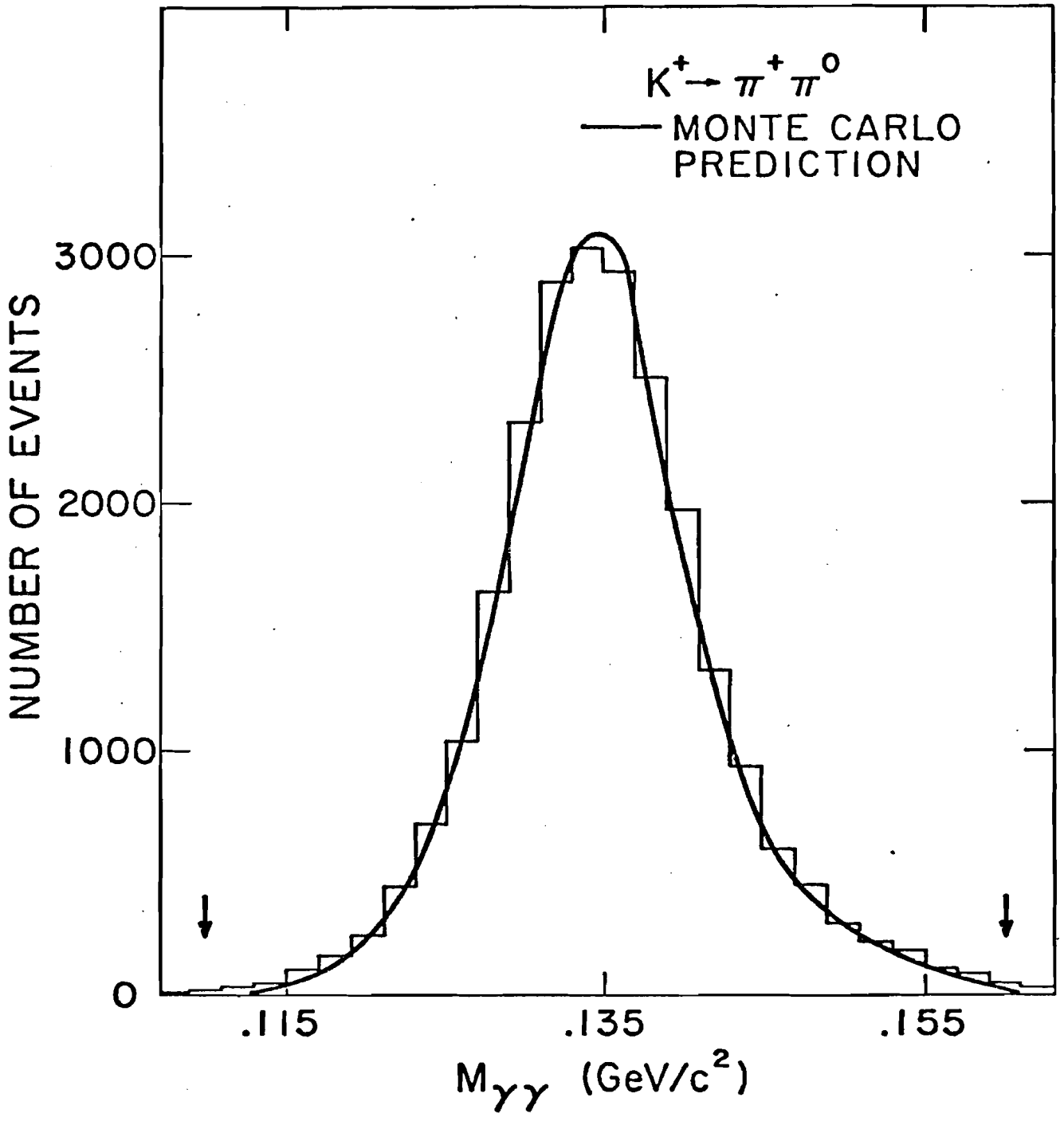
$K^+ \to \pi^+ \pi^0$
MONTE CARLO PREDICTION
NUMBER OF EVENTS
3000
2000
1000
0
.115
.135
.155
$M_{\gamma\gamma}$ (GeV/c^2)

Figure 30

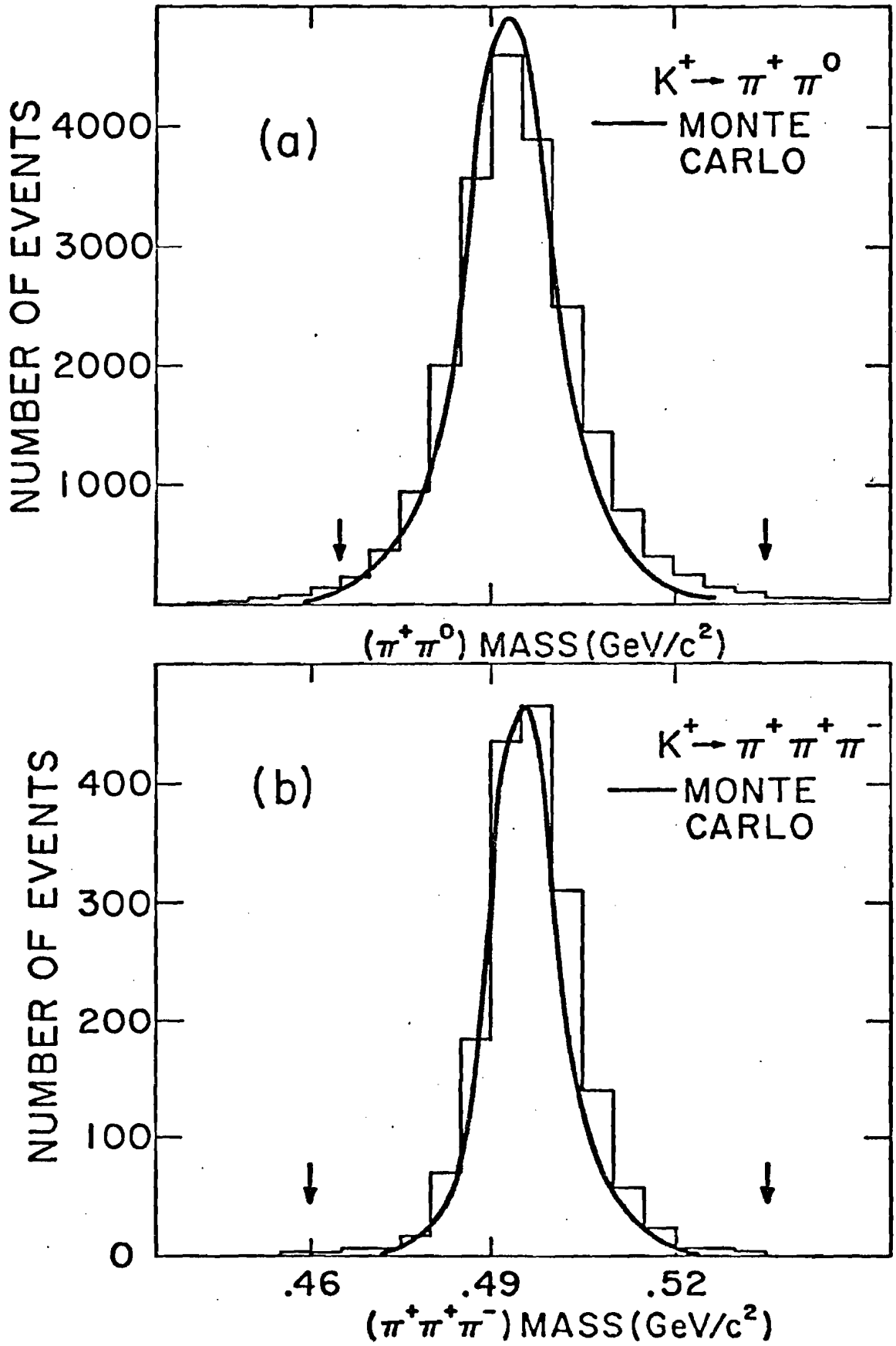
(a)
$K^+ \to \pi^+ \pi^0$
MONTE CARLO
NUMBER OF EVENTS
4000
3000
2000
1000
$(\pi^+\pi^0)$ MASS (GeV/c^2)
(b)
$K^+ \to \pi^+ \pi^+ \pi^-$
MONTE CARLO
NUMBER OF EVENTS
400
300
200
100
0
.46
.49
.52
$(\pi^+\pi^+\pi^-)$ MASS (GeV/c^2)

Figure 31

two photon mass were applied to the data before plotting. Mass resolutions are 8 Mev/c^2 for the $\pi^+\pi^\circ$ mass and 7 Mev/c^2 for the $\pi^+\pi^+\pi^-$ mass. The arrows indicate the mass cuts applied to the data.

The distribution for the square of the transverse distance of the charged particle π^+ of the $K^+ \rightarrow \pi^+\pi^\circ$ decay from the beam axis at Z position of P1X chamber is shown in Figure 32a. The agreement between the real data and the Monte Carlo model indicates that the chamber inefficiency in the beam region did not cause any serious problem.

Figure 32b shows the angular distribution of the $K^+ \rightarrow \pi^+\pi^\circ$ decays in the helicity frame. The angle is that of the charged pion relative to the flight direction of the kaon. Since the kaon has zero spin, the angular distribution must be isotropic. But the charged tracks with small θ were vetoed by the MBV2, BA and VE counters and the low energy π°'s tended to be eliminated by the AM counters and the minimium photon energy requirement of the LAC. Thus the acceptance was a strong function of Cosθ as shown in the plot.

The Dalitz plots for $K^+ \rightarrow \pi^+\pi^+\pi^-$ decays are shown in Figure 33 for the real data and the Monte Carlo model

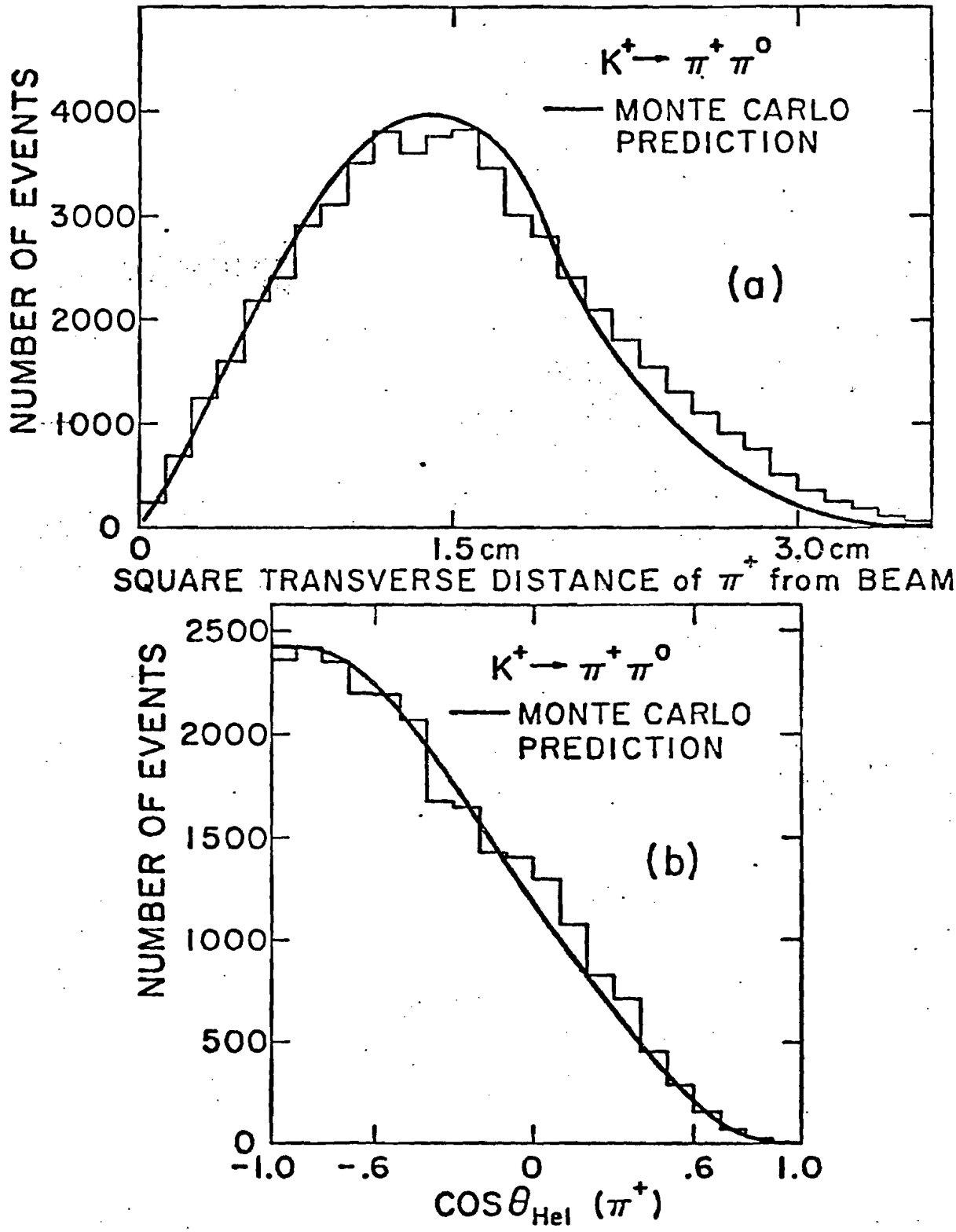
$K^+ \to \pi^+ \pi^0$
MONTE CARLO PREDICTION
(a)
NUMBER OF EVENTS
4000
3000
2000
1000
0
0
1.5 cm
3.0 cm
SQUARE TRANSVERSE DISTANCE of π^+ from BEAM
$K^+ \to \pi^+ \pi^0$
MONTE CARLO PREDICTION
(b)
NUMBER OF EVENTS
2500
2000
1500
1000
500
0
-1.0
-.6
0
.6
1.0
$\cos\theta_{Hel}$ (π^+)

Figure 32

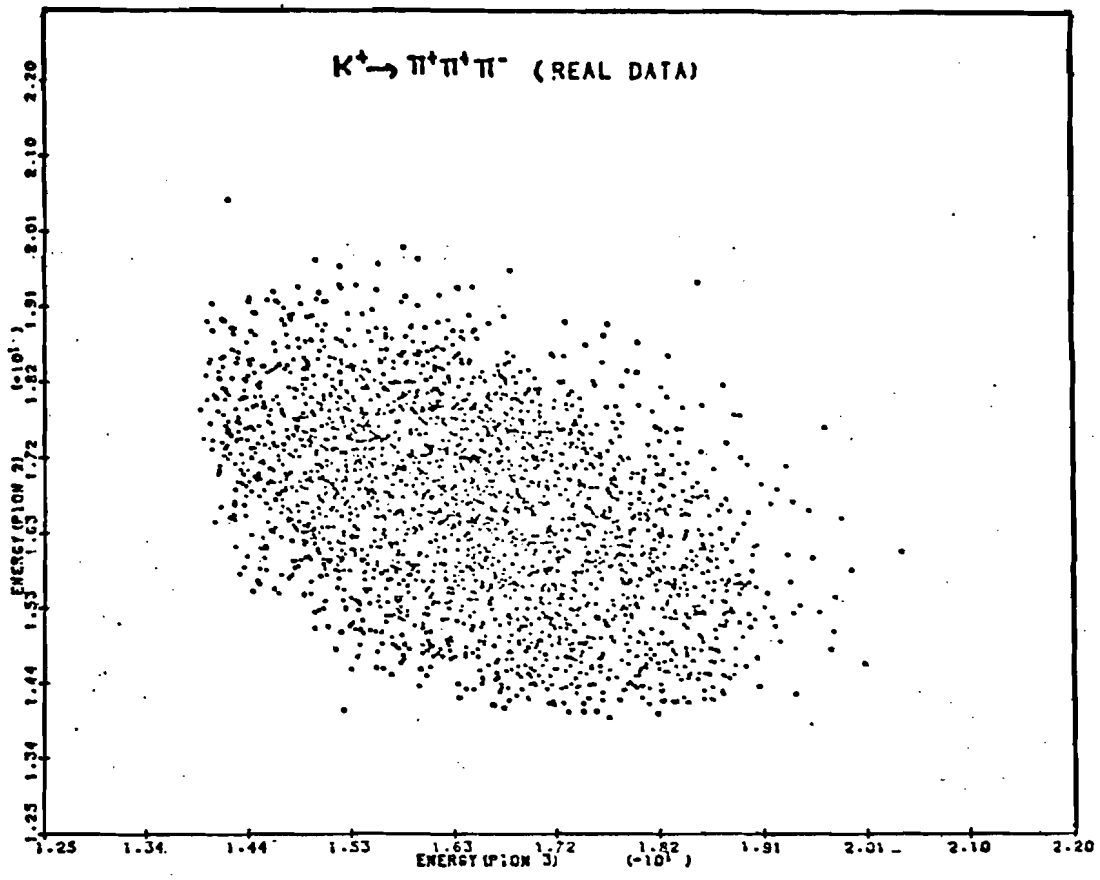
K+→ π+π+π- (REAL DATA)
ENERGY (PION 2) (-10¹)
ENERGY (PION 3) (-10¹)
1.25
1.34
1.44
1.53
1.63
1.72
1.82
1.91
2.01
2.10
2.20

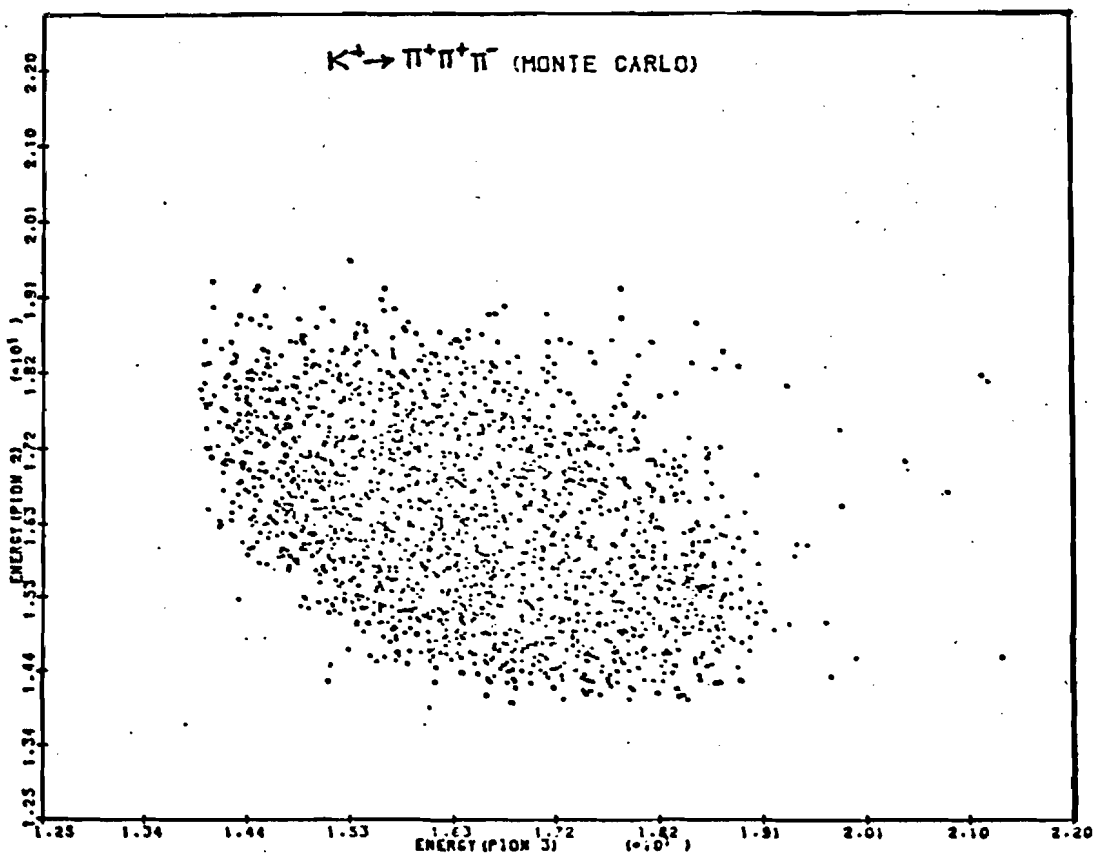
K+→ π+π+π- (MONTE CARLO)
ENERGY (PION 2) (-10¹)
ENERGY (PION 3) (-10¹)
1.25
1.34
1.44
1.53
1.63
1.72
1.82
1.91
2.01
2.10
2.20

Figure 33

events. The point densities seem to be uniform, except at the tails where the low energy events described earlier are apparent, as expected for spin zero particle decays.

In Figure 34a we show the distribution of the energy asymmetry, $|E_{\gamma 1} - E_{\gamma 2}|/(E_{\gamma 1} + E_{\gamma 2})$. Here, $E_{\gamma 1}$ is the energy of the one photon and $E_{\gamma 2}$ is that of the other photon from the $K^+ \rightarrow \pi^+\pi^\circ$ decays. Cuts on total energy, $\pi^+\pi^\circ$ mass, 2-photon mass and decay vertex were applied to define the $K^+ \rightarrow \pi^+\pi^\circ$ decays in this plot. The only restrictions on photon energies were those imposed during the reconstruction. The agreement between the data and the Monte Carlo model prediction is quite good. The distribution for the transverse distance between the charged particle and the nearest photon of the same decays at the Z-position of the LAC is presented in Figure 34b. The lower cutoff of 2.5 cm is apparent. The good agreement between the data and the Monte Carlo prediction is an indicator to how well the hadrons were accounted for as far as their interference to photon reconstruction is concerned.

In Figure 35, the t-distributions of $K^+ \rightarrow \pi^+\pi^\circ$ are shown for the lead, the copper and the empty (MT) targets. The effect of the multiple scattering for different targets is clearly seen. With a perfect resolution spectrometer, all of the events would appear at t=0. The finite

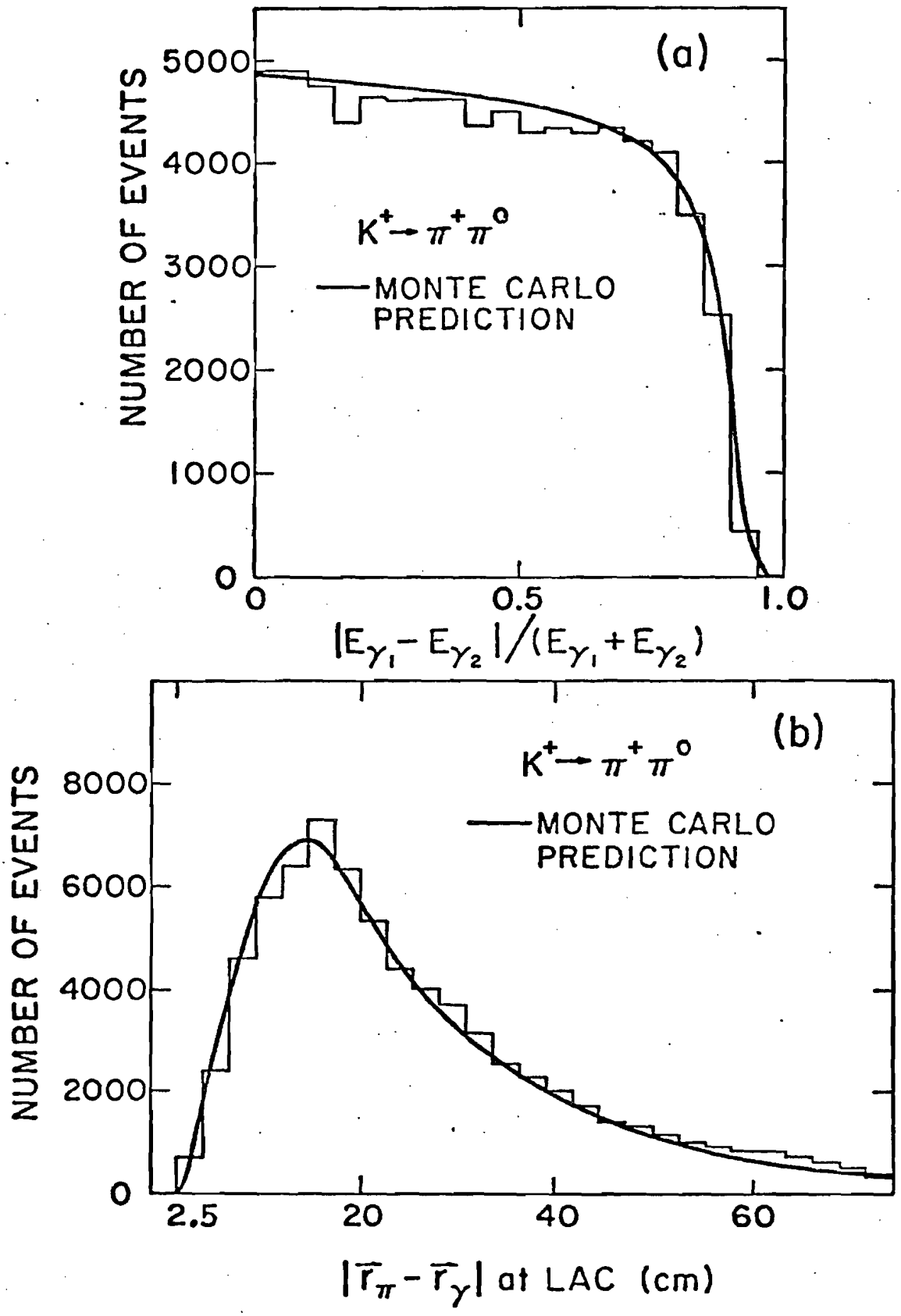
(a)
NUMBER OF EVENTS
5000
4000
3000
2000
1000
0
$K^+ \to \pi^+ \pi^0$
MONTE CARLO PREDICTION
0
0.5
1.0
$|E_{\gamma_1} - E_{\gamma_2}|/(E_{\gamma_1} + E_{\gamma_2})$
(b)
NUMBER OF EVENTS
8000
6000
4000
2000
0
$K^+ \to \pi^+ \pi^0$
MONTE CARLO PREDICTION
2.5
20
40
60
$|\bar{r}_\pi - \bar{r}_\gamma|$ at LAC (cm)

Figure 34

t-resolution is seen from the figure. A Gaussian fit to the plot indicated a p_T resolution of 8 Mev/c for the MT, 10 Mev/c for the lead and 12 Mev/c for the copper targets.

The t-distributions for $K^+ \rightarrow \pi^+\pi^+\pi^-$ are shown in Figure 36. There the difference between targets are less obvious and the p_T resolution is seen to be 12 Mev/c for the empty target (MT) 13 Mev/c for the lead and 15 Mev/c for the copper targets. During fitting the t-distributions of Reactions (8) - (11), the p_T resolutions above were used in the fitting program.

In summary, the excellent agreement between the Monte Carlo model and the data for the $K^+ \rightarrow \pi^+\pi^0$ and $K^+ \rightarrow \pi^+\pi^+\pi^-$ decays gives us confidence that the same model will be accurate for the A_2^+ and $K^{*+}(1430)$ decays. For these decays the low statistics of the data limits our ability to compare directly the data and the Monte Carlo model.

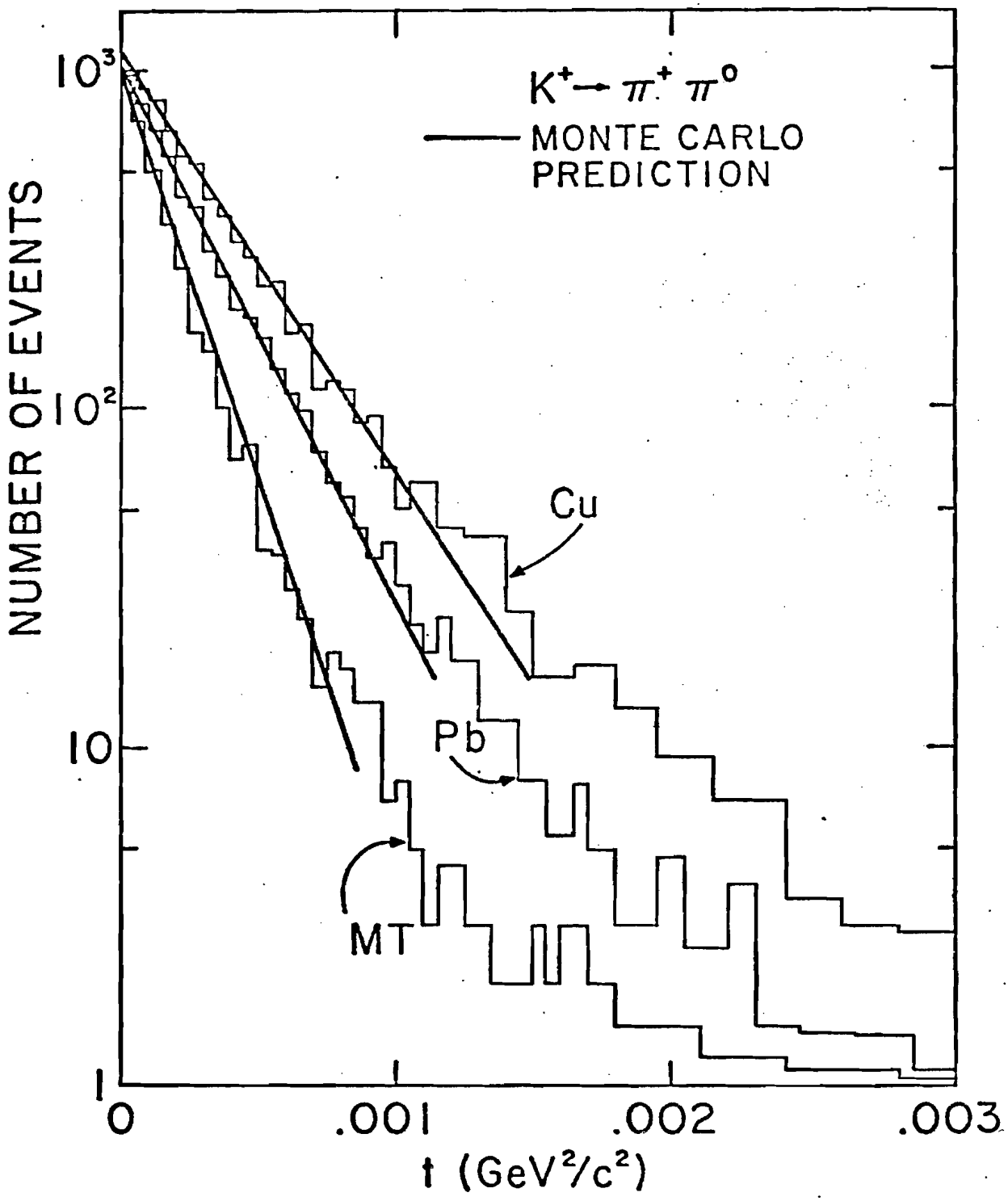
$K^+ \rightarrow \pi^+ \pi^0$
MONTE CARLO PREDICTION
NUMBER OF EVENTS
10^3
10^2
10
1
0
.001
.002
.003
t (GeV²/c²)
Cu
Pb
MT

Figure 35

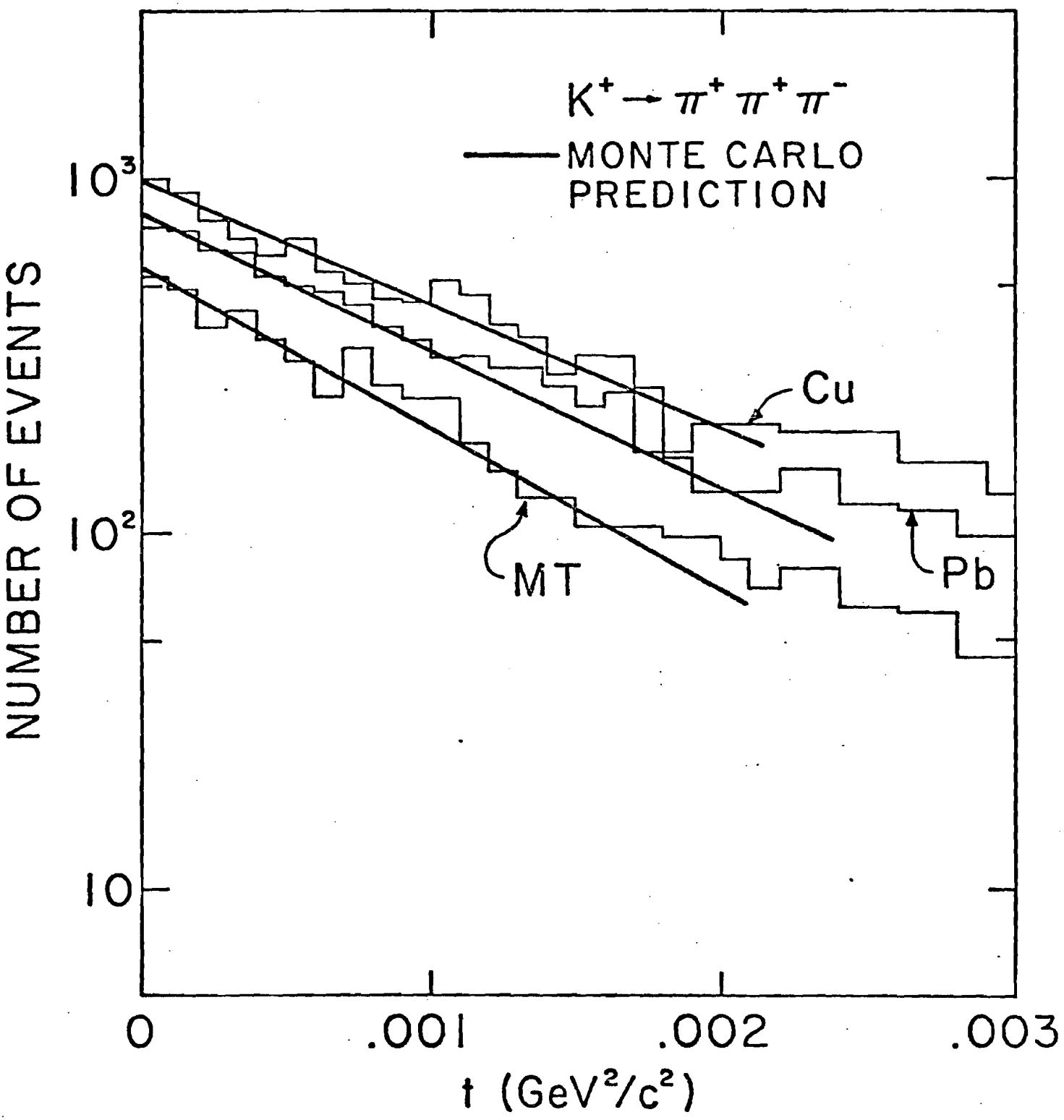
$K^+ \rightarrow \pi^+ \pi^+ \pi^-$
MONTE CARLO PREDICTION
Cu
Pb
MT
NUMBER OF EVENTS
10^3
10^2
10
0
.001
.002
.003
t (GeV²/c²)

Figure 36

CHAPTER V

DATA NORMALIZATION

It is explicit from Equation (7) that the radiative decay widths $\Gamma(A_2^+ \to \pi^+\gamma)$ and $\Gamma(K^{*+}(1430) \to K^+\gamma)$ are directly proportional to the Coulomb production cross sections of the A_2^+ and $K^{*+}(1430)$ mesons. There are however some uncertainties concerning the measurements of these cross sections. The absolute efficiencies of the components of the spectrometer are difficult to determine. There may be dead time and possibly other effects which affect the overall trigger efficiency. These effects may not be detected by comparing the Monte Carlo predictions on various distributions with data on the $K^+ \to \pi^+\pi^0$ and $K^+ \to \pi^+\pi^+\pi^-$ decays, although the model itself agrees very well with the data. To compensate for all the uncertainities one can and can not think of, a factor averaged over the entire running period was needed to normalize the cross section data before the widths could be calculated. The kaon decays, collected simultaneously with the A_2^+ and $K^{*+}(1430)$ events, were used for this purpose. In this chapter, we describe the determination of the corrections and the normalization factors. Section A discusses the correction factors applied to the data. The normalization procedure as derived from

the kaon decays is explained in Section B.

A. CORRECTIONS TO DATA

There are many ways that particles produced by interactions in the target could be lost without being detected by the spectrometer. For instance, the secondary charged particles could be absorbed. The photons could be converted into $e^+ e^-$ pairs by the target or by the material in the spectrometer. Some events were vetoed by the random firings of various counters. These and other similar processes required some corrections to be applied to the data.

The correction factors for photon conversion into $e^+ e^-$ pairs can be calculated from the approximate formula[32]

$$N(t) = N_0 \exp\left(-\frac{7}{9} t\right)$$

where t is the radiation length of the absorbing material. The effect of the absorption of charged particles was estimated by using the data of A. S. Carroll et al[33] on absorption cross sections.

The corrections can be categorized in various groups:

1) Spectrometer Related Corrections

The various components of the spectrometer could produce by absorption a loss of charged particles and photons. The material in the chambers, the counters and others amounted to 3.42×10^{-2} proton collision length and 8.44×10^{-2} radiation length. The correction factors for the charged particle absorption and the photon conversion by this material are listed in Table IIa. As seen from the table, the absorption corrections for charged particles are different for the different trigger modes. This is so because some of the material in the spectrometer did not interfere in the VEE trigger events.

The beam particles, as well as the produced secondary charged particles, could be absorbed by the target. The photons from π^0 or η decays inside the target could be converted into $e^+ e^-$ pairs. The correction factors for these effects are listed in Table IIb.

2) Beam Related Corrections

The incident beam flux was measured with the procedure outlined in Chapter II.F. Corrections were applied for misidentification of beam particles by the Cerenkov counters, and for decays and interactions of the beam particles along the beam line.

Misidentification of the beam particles by the Cerenkov counters was caused mostly by electronic noise. The pressure curves (Figures 8, 9, 10) and particle counting scalers were used to estimate the correction factors. The kaon contamination in the pion beam was about 0.5%. The pion contamination in the kaon beam was about 1.5%.

The pion beam also contained ~0.5% electrons and muons[34] that were recorded by the Cerenkov counters as pions.

Kaons and pions could decay before they reached the target. Via a Monte Carlo program, the decays $\pi^+ \rightarrow \mu^+\nu$ and $K^+ \rightarrow \mu^+\nu$ were determined to reduce the effective pion and kaon beam fluxes by 0.4%.

The material like the J1 and J2 chambers, He bags and beam pipe windows in the beam line, 4 m upstream of the

target, amounted to about 5.7×10^{-3} proton absorption length. Correction for the absorption of the beam by this material was estimated to be less than 0.5%. The interaction of the beam particles with this material caused an increase in the number of beam tracks for some events. Some of the events had no beam track information at all. This could create ambiguities and therefore triggers with no or more than one beam tracks were disregarded; a correction was applied for that effect.

Also, any of the counters, V1-V4, A0L, A0R, A1, A2, H or AM, could have fired on occasion, killing good events. This could happen when a scattered beam particle hits any of these counters or by a production of δ -rays at the target. To estimate an overall correction factor for these effects, beam particles of the BEAM trigger events were tracked through the spectrometer until they hit the BA counter. A signal from any of these counters in coincidence with the beam was searched for. The existing signals could have been created by δ -rays (if they were from V1-V4), by random firings of any counter or by a misaligned H counter. The rate at which these ccincidences were taking place was used to determine the correction factor for their effects. Ideally, a signal from the S counter should have been present for every beam trigger. As a matter of fact, at some point during the experiment, the S counter was

discovered to have been accidentally bent away from the beam line. The rate at which the beam tracks missed the S counter was used to correct for the effect of this accident.

The results of all these corrections, combined for the runs of each targets, are listed in Table IIc.

3) Other Corrections

The hadronic interactions within the LAC were discussed in Chapter III.A. Sometimes, pulses generated by hadrons were reconstructed as photons. Therefore, some of the three photon events were actually two photon (RHO or Al trigger) events, some of the one photon events were no photon (Al trigger) events. By studying the $K^+ \rightarrow \pi^+\pi^0$ events that contained an extra photon, a 2.2% correction was determined to be applied and RHO and Al trigger mode events. The study on $K^+ \rightarrow \pi^+\pi^+\pi^-$ events with one extra photon showed that a 7.2% correction should be applied to the events in the Al trigger mode. The VEE trigger events did not need any of these corrections because the LAC had no part in these events.

The thresholds determining the discriminator levels of the S counter signals necessitated a 0.6% correction to the RHO mode events and a 10% correction to the VEE mode events.

The Dalitz decay of $\pi^0 \rightarrow e^+ e^- \gamma$ implies a 1.15% correction for the reactions involving a π^0.

B. NORMALIZATION

If all losses of real events could be exactly determined, one could obtain accurate corrections for each types of events. In practice this is hard to achieve. In order to check the corrections we determined, they were applied to the reactions that were understood well, namely the decays $K^+ \rightarrow \pi^+\pi^0$ and $K^+ \rightarrow \pi^+\pi^+\pi^-$. The results of the analysis of the A_2^+ and $K^{*+}(1430)$ data were normalized to the observed rates of these decays.

The normalization factors were determined as follows:

The numbers of kaons in the beam expected to decay inside the decay pipe were calculated for the above two modes. For these calculations, the decay intervals were taken as the ones shown in Figure 28 by arrows. Then the numbers of kaon decays observed in these modes were compared with the expected numbers after the above corrections and the acceptance corrections were applied. The acceptance corrections were determined by using the Monte Carlo model of the experiment (see Chapter IV) and included both the geometrical and trigger acceptances. The ratio of the expected to the observed number of decays is identified as

the normalization factor. This procedure was followed for each target and the results are listed in Table III.

Both normalization factors would be equal to the unity if all the losses were accounted for. The deviation from the unity in the $K^+ \longrightarrow \pi^+\pi^+\pi^-$ normalization factors is larger than the others. That means there are more events in this decay that we could not account for. This is expected since the $K^+ \longrightarrow \pi^+\pi^+\pi^-$ events are more complex and difficult to reconstruct compared to the $K^+ \longrightarrow \pi^+\pi^0$ events. The chamber inefficiencies are more effective in three charged particle events and tracks can easily be lost. In addition, the decay vertex definition gets more dubious when it involves three outgoing charged particles.

TABLE IIa

Spectrometer Related Correction Factors

Correction Factor for \ Trigger	RHO , Al	VEE
π^+ Absorption in Spectrometer	1.0270 ± 0.0008	1.0246 ± 0.0007
K^+ Absorption in Spectrometer	1.0242 ± 0.0007	1.0220 ± 0.0006
$\pi^0(\eta)$ Conversion in Spectrometer	1.1403 ± 0.0028	----

TABLE IIb

Target Related Correction Factors

Correction Factor for \ Target	CU	PB
π^+ Absorption in Target	1.0176 ± 0.0030	1.0028 ± 0.0005
K^+ Absorption in Target	1.0163 ± 0.0030	1.0027 ± 0.0005
$\pi^0(\eta)$ Conversion in Target	1.3815 ± 0.0027	1.1776 ± 0.0030

TABLE IIc

Beam Correction Factors

Target	CU		PB	
Trigger / Beam Particle	RHO , VEE	Al	RHO , VEE	Al
π^+	1.381 ± 0.027	1.562 ± 0.031	1.389 ± 0.027	1.474 ± 0.029
K^+	1.366 ± 0.029	1.531 ± 0.030	1.351 ± 0.026	1.427 ± 0.028

TABLE III

K^+-Decay Normalization Factors

Target / Reaction Mode	CU	PB
RHO	1.036 ± 0.020	1.051 ± 0.021
VEE	1.164 ± 0.033	1.108 ± 0.026

CHAPTER VI

A_2^+ AND $K^{*+}(1430)$ DATA

In this chapter we discuss the analysis of the data on the Primakoff productions of A_2^+ and $K^{*+}(1430)$ In Sections A and B, we present the decay modes of the A_2^+ and $K^{*+}(1430)$ mesons which were investigated. In particular, we study the reactions

$$\pi^+ A \longrightarrow A\, \pi^+ \eta, \quad \eta \hookrightarrow \gamma\gamma \tag{12a}$$

$$\eta \hookrightarrow \pi^+\pi^-\pi^0 \tag{12b}$$

$$\pi^+ A \longrightarrow A\, K^+ K_S^0, \quad K_S^0 \hookrightarrow \pi^+\pi^- \tag{13}$$

$$K^+ A \longrightarrow A\, K^+ \pi^0, \quad \pi^0 \hookrightarrow \gamma\gamma \tag{14}$$

$$K^+ A \longrightarrow A\, K_S^0 \pi^+, \quad K_S^0 \hookrightarrow \pi^+\pi^- \tag{15}$$

where A represents the target nucleus. We also compare the results with the Monte Carlo model predictions to check the reliability of the normalization procedure. In Section C, we present the results of mass fittings and in Section D, we fit the t-distribution and extract the radiative decay widths of A_2^+ and $K^{*+}(1430)$.

The details of the Monte Carlo model of the experiment have already been discussed in Chapter IV. To simulate Reactions (12) - (15), the corresponding particles were generated at the target with $t \sim 0$. The acceptance was found to be nearly t-independent for $t < 0.1$ $(Gev/c)^2$. Then the decays of these particles were simulated using a $\sin^2\theta \cos^2\theta \sin^2\phi$ decay distribution in the Gottfried-Jackson frame and the produced particles were traced through the spectrometer. Events that were outside of the geometrical acceptance of the spectrometer or those that did not satisfy the simulated trigger logic were rejected. In the following figures the predictions of the Monte Carlo model are indicated by solid curves. The real data are shown by histograms.

Comparing the data and the Monte Carlo predictions the following cuts were determined to define Reactions (12)-(15):

i) Total energy within 195 and 212 Gev for Reaction (12a), and 192 and 212 Gev for the others.

ii) Interaction vertex within +/- 28 cm of the target.

iii) Two photon mass in the range 0.51-0.58 Gev/c^2 to define the η meson for Reaction (12a).

iv) Two photon mass in the range 0.11-0.16 Gev/c^2 to define the π^0 meson in Reactions (12b) and (14).

v) $\pi^+\pi^-\pi^0$ mass within 0.50 and 0.59 Gev/c^2 to define the η meson for Reaction (12b).

vi) $\pi^+\pi^-$ mass in the range 0.46-0.54 Gev/c^2 to define the K_S^0 meson for Reactions (13) and (15).

These cuts are indicated by arrows on the corresponding figures below.

A. A_2^+(1310) DATA

The $\pi^+\eta$ mass distributions shown in Figure 37 for the lead and the copper targets indicate that Reaction (12a) is dominated by A_2^+ production. The data were required to have the cuts (i), (ii) and (iii) on total energy, interaction vertex and mass described above.

The main source of background is the production of the B^+(1235) particle that decays into $\omega\pi^+$ followed by $\omega \rightarrow \pi^0\gamma$ and $\pi^0 \rightarrow \gamma\gamma$. Missing one of the three photons makes this decay look like Reaction (12a). A tighter energy cut was applied to eliminate the B^+(1235) decays. Figure 38 shows the total energy distribution of the events in Figure 37 without the cut (i). The low energy tail is due to the background events just mentioned. The shaded distributions are obtained if the data are required to have a $\pi^+\eta$ mass cut of 1.20 - 1.44 Gev/c^2. This requirement eliminates most of the background events since the missing photon lowers the B^+(1235) mass further down.

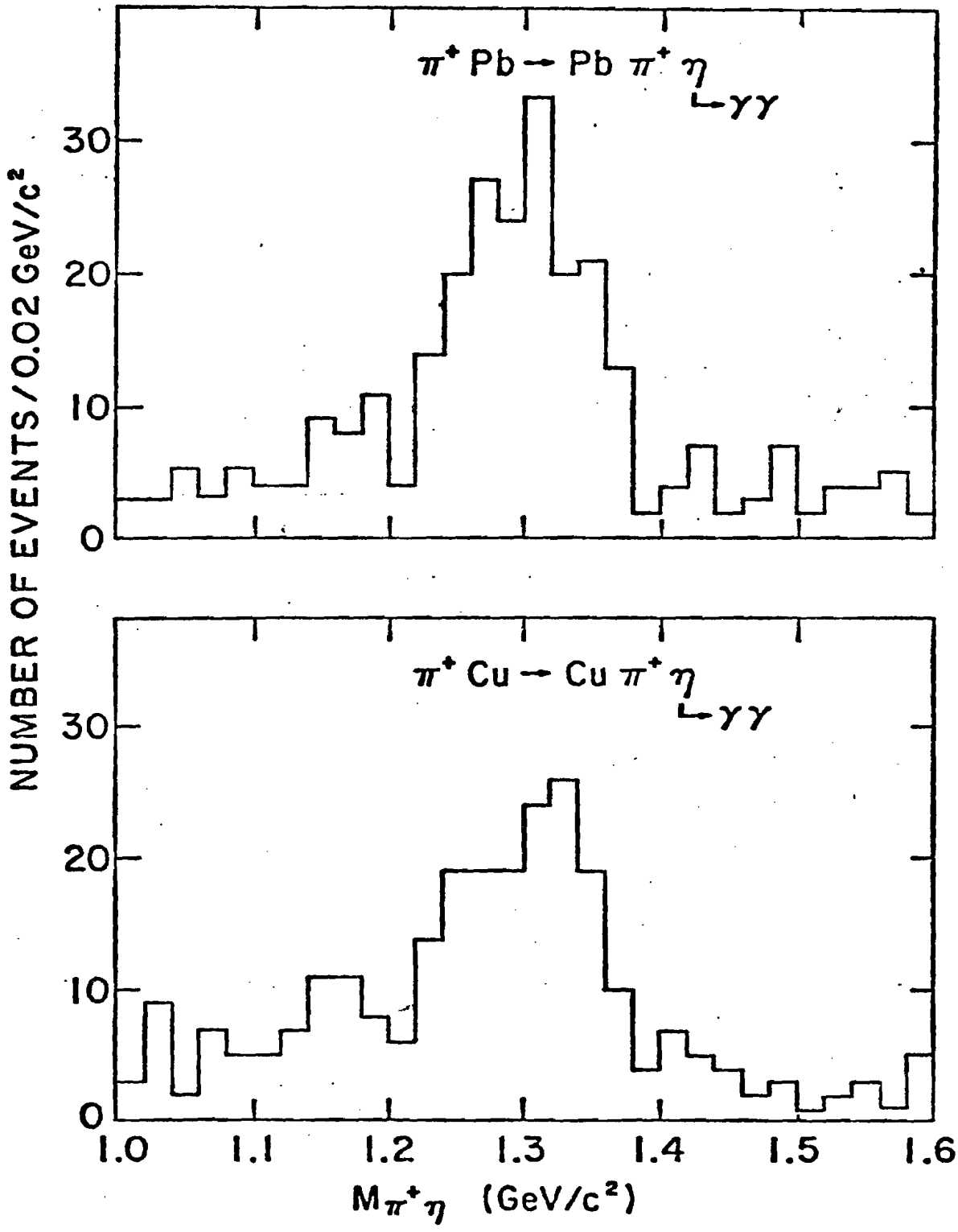
π^+ Pb → Pb $\pi^+ \eta$
$\gamma\gamma$
π^+ Cu → Cu $\pi^+ \eta$
$\gamma\gamma$
NUMBER OF EVENTS / 0.02 GeV/c²
0
10
20
30
1.0
1.1
1.2
1.3
1.4
1.5
1.6
$M_{\pi^+\eta}$ (GeV/c²)

Figure 37

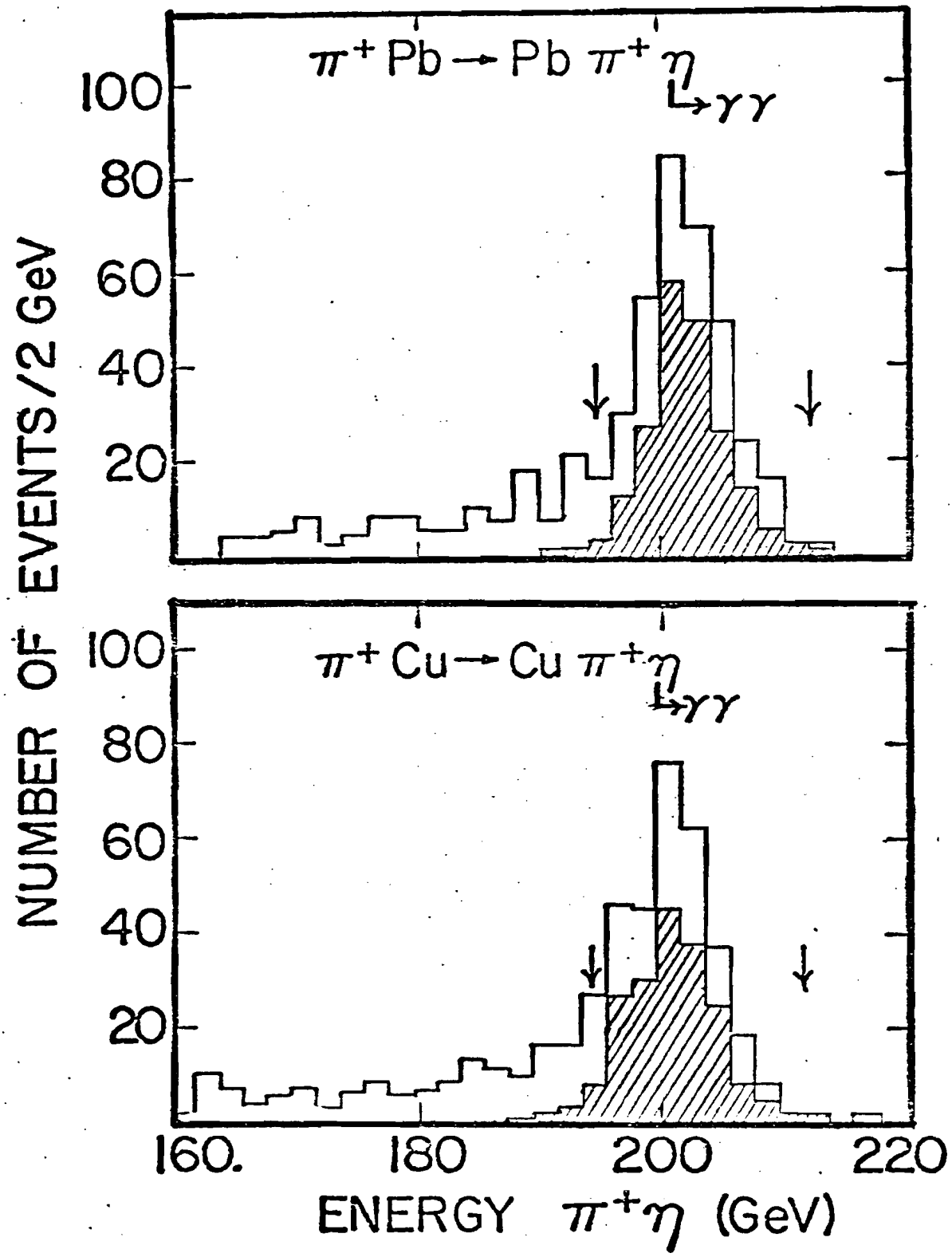
$\pi^+ Pb \rightarrow Pb\ \pi^+ \eta$
$\hookrightarrow \gamma\gamma$
$\pi^+ Cu \rightarrow Cu\ \pi^+ \eta$
$\hookrightarrow \gamma\gamma$
NUMBER OF EVENTS/2 GeV
100
80
60
40
20
160.
180
200
220
ENERGY $\pi^+\eta$ (GeV)

Figure 38

Figure 39a shows the reconstructed interaction vertex for A_2^+ candidates from Reaction (12a) with the lead target. The cuts (i) and (iii) above have been applied to the data. In addition, a requirement of $t \lesssim 0.005$ $(Gev/c)^2$ was imposed to ensure the coherent Coulomb production (see Figure 58 for t-distributions of these events). The data have also been corrected for empty target background. The Monte Carlo prediction is in good agreement with the data.

Figure 39b shows the angular distribution of the A_2^+ decays in the Gottfried-Jackson frame. Data were required to satisfy the conditions (i),(ii) and (iii) and have a $\pi^+\eta$ mass between 1.20 Gev/c^2 and 1.44 Gev/c^2. The data and the Monte Carlo prediction are in good agreement with $\sin^2\theta \cos^2\theta$ dependence as expected for the decay of coherently produced A_2^+ (see Chapter I.A). The fall off for small values of θ ($\cos\theta \sim 1$) is due to MBV2 and BA vetoes. The $\sin^2\phi$ dependence could not be resolved by the spectrometer. The production plane is poorly known because of the finite t-resolution.

The two photon mass distribution for the same events is shown in Figure 40 for the lead target. The cuts (i) and (ii) were imposed on the data. The Monte Carlo prediction agrees well with the data. For comparison, the two photon mass distribution obtained from $\rho^+ \rightarrow \pi^+\pi^0$ decays is also shown in the same figure.

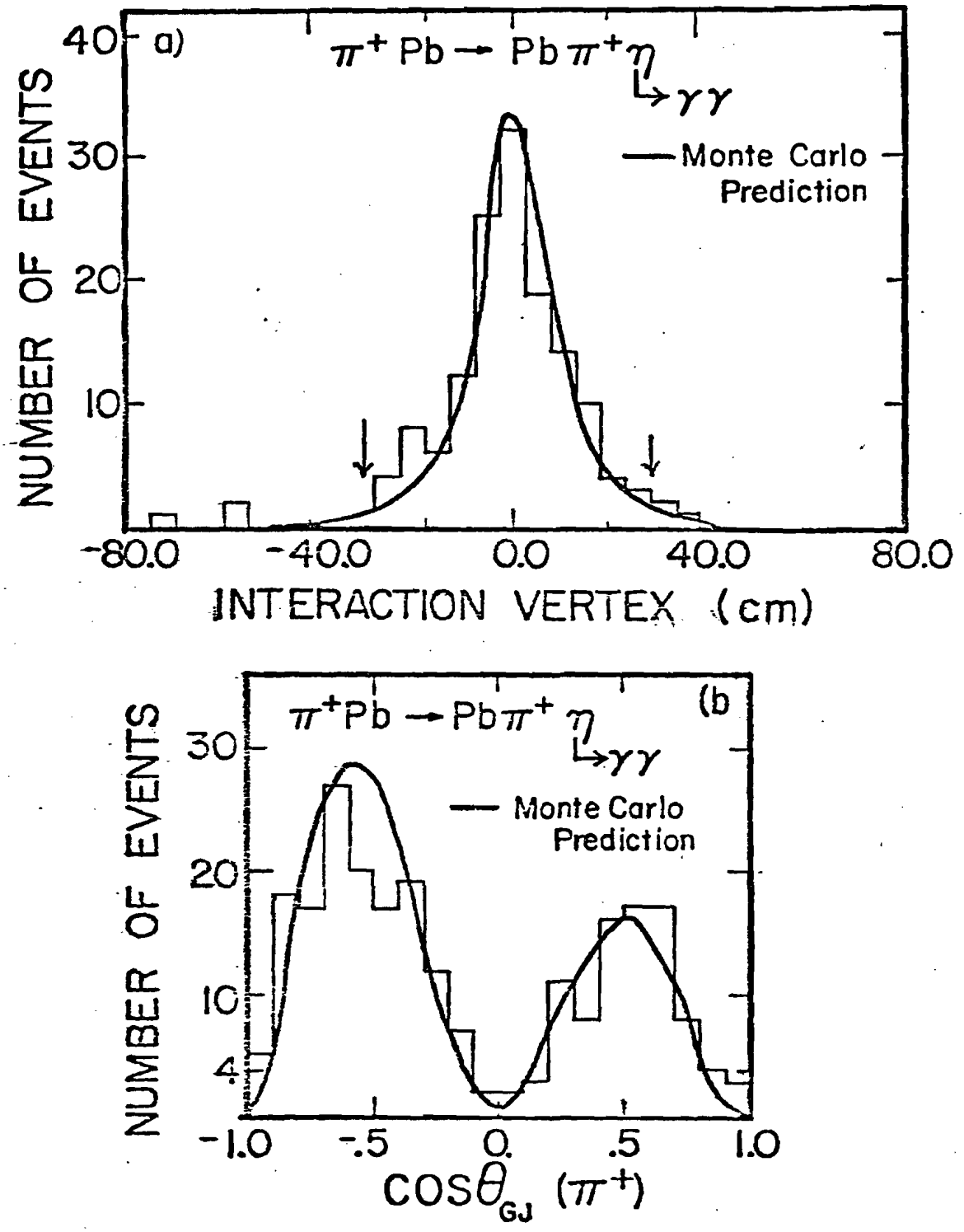
a)
$\pi^+ Pb \rightarrow Pb\pi^+\eta$
$\hookrightarrow \gamma\gamma$
Monte Carlo Prediction
NUMBER OF EVENTS
40
30
20
10
-80.0
-40.0
0.0
40.0
80.0
INTERACTION VERTEX (cm)
(b
$\pi^+ Pb \rightarrow Pb\pi^+\eta$
$\hookrightarrow \gamma\gamma$
Monte Carlo Prediction
NUMBER OF EVENTS
30
20
10
4
-1.0
-.5
0.
.5
1.0
$\cos\theta_{GJ}$ (π^+)

Figure 39

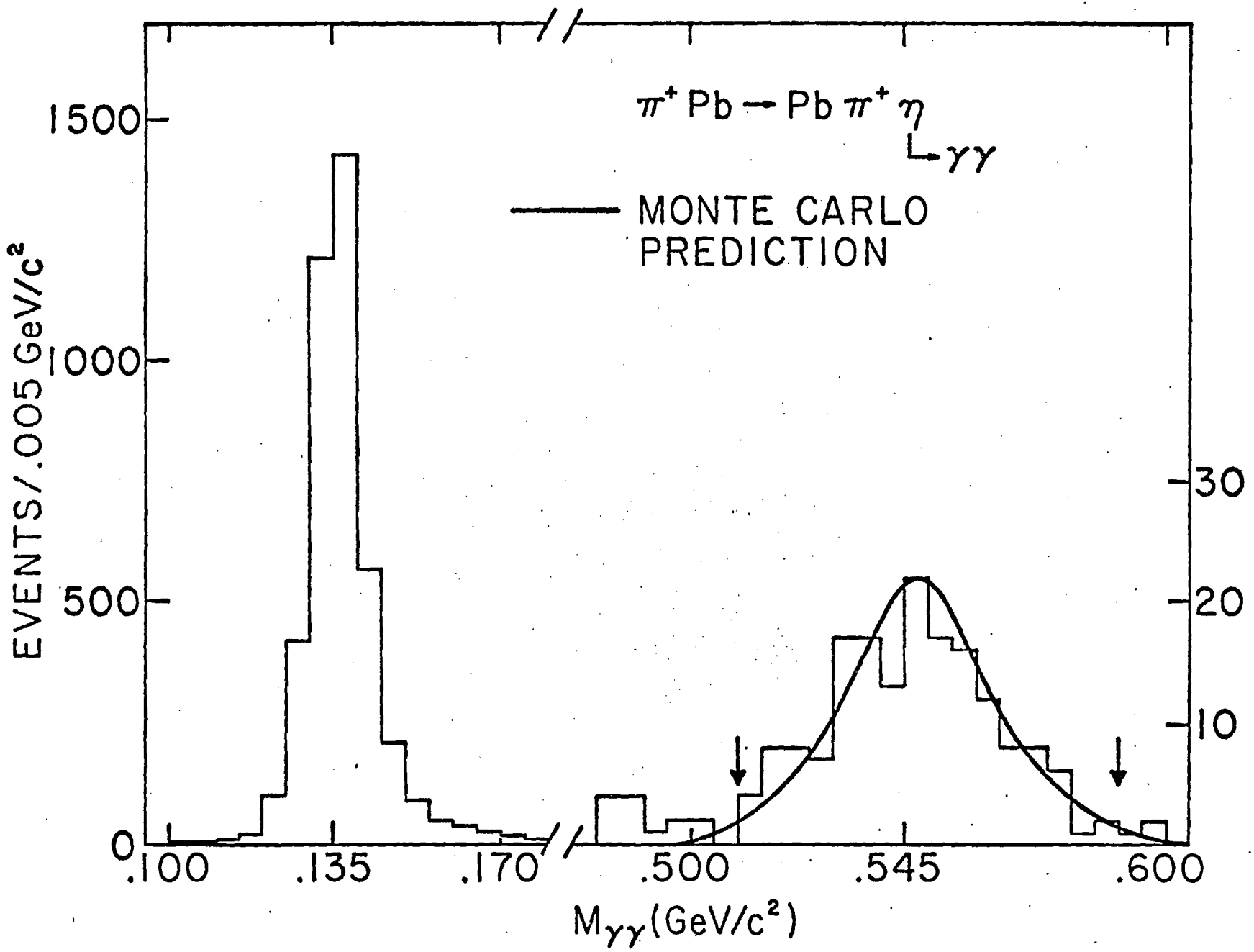
$\pi^+ Pb \rightarrow Pb\, \pi^+ \eta$
$\hookrightarrow \gamma\gamma$
MONTE CARLO PREDICTION
EVENTS/.005 GeV/c²
1500
1000
500
0
30
20
10
.100
.135
.170
.500
.545
.600
$M_{\gamma\gamma}$(GeV/c²)

Figure 40

In Figure 41a, we show the $\pi^+\pi^+\pi^-\pi^0$ mass distribution as an indication to the dominance of Reaction (12b) by A_2^+ production. The lead and the copper data were combined to improve the resonance with better statistics. The data were required to have the cuts (i), (ii), (iv) and (v) on total energy, interaction vertex, two photon mass and $\pi^+\pi^-\pi^0$ mass.

Figure 41b shows the reconstructed total energy for the events described above without the cut (i). The distribution of the interaction vertex is presented in Figure 42a for the same events. The data were imposed the cuts (i), (iv), (v) and corrected for empty target. Again the Monte Carlo prediction is in good agreement with the data.

The angular distribution of the A_2^+ decays in the Gottfried-Jackson frame is shown in Figure 42b for the events of Figure 41a that have $\pi^+\pi^+\pi^-\pi^0$ mass in the range 1.16-1.54 Gev/c^2. The $\sin^2\theta\cos^2\theta$ dependence is apparent and in reasonably good agreement with the Monte Carlo model. Figure 42c shows the two photon mass distribution for the same data without the cut (iv). The Monte Carlo prediction is consistent with the data.

In Figure 43, we present the $\pi^+\pi^-\pi^0$ mass distribution of the $\pi^+\pi^+\pi^-\pi^0$ events. The data have the cuts (i), (ii) and

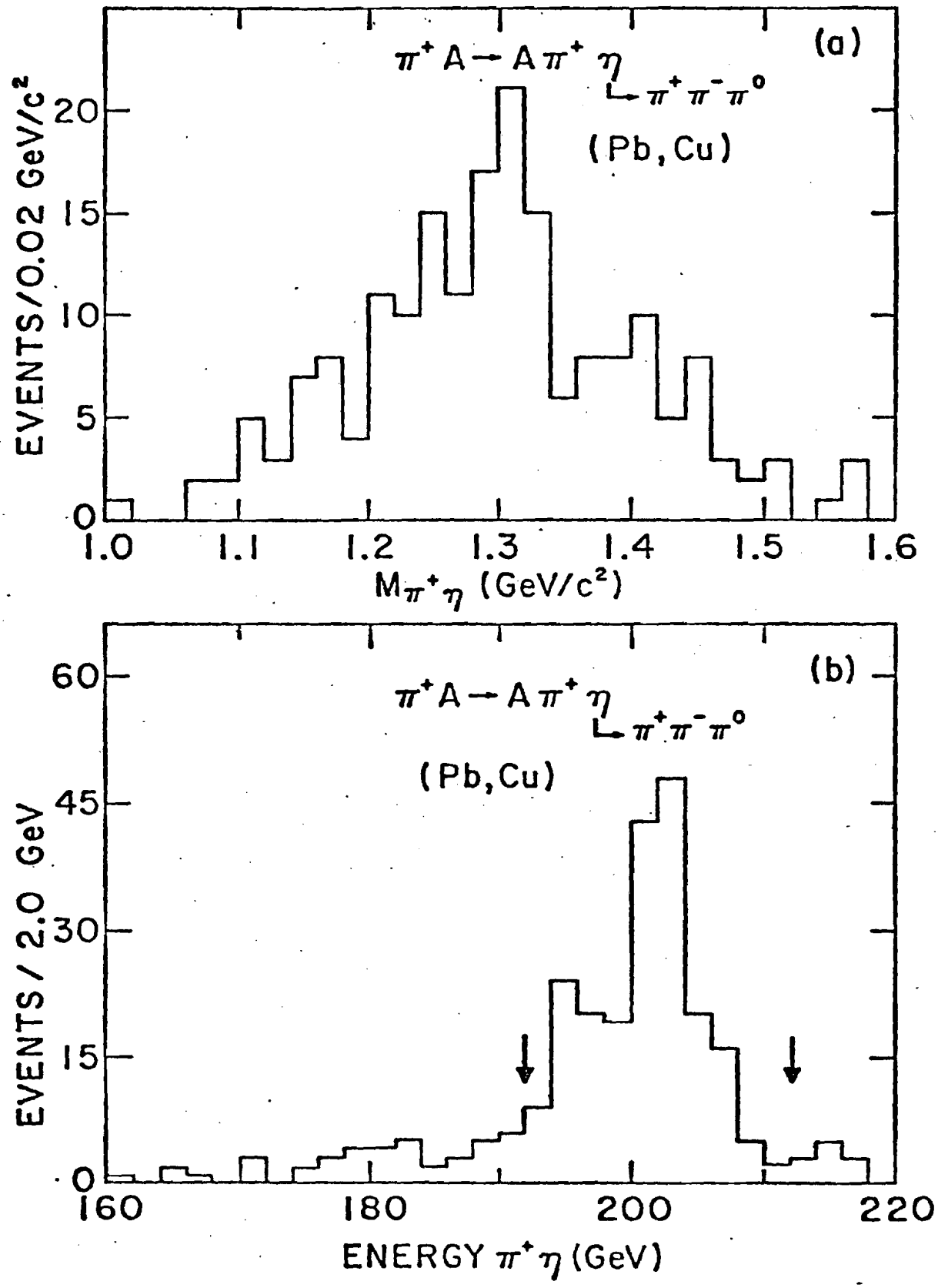
(a)
$\pi^+ A \rightarrow A \pi^+ \eta$
$\hookrightarrow \pi^+ \pi^- \pi^0$
(Pb, Cu)
EVENTS/0.02 GeV/c²
0
5
10
15
20
1.0
1.1
1.2
1.3
1.4
1.5
1.6
$M_{\pi^+\eta}$ (GeV/c²)
(b)
$\pi^+ A \rightarrow A \pi^+ \eta$
$\hookrightarrow \pi^+ \pi^- \pi^0$
(Pb,Cu)
EVENTS / 2.0 GeV
0
15
30
45
60
160
180
200
220
ENERGY $\pi^+\eta$ (GeV)

Figure 41

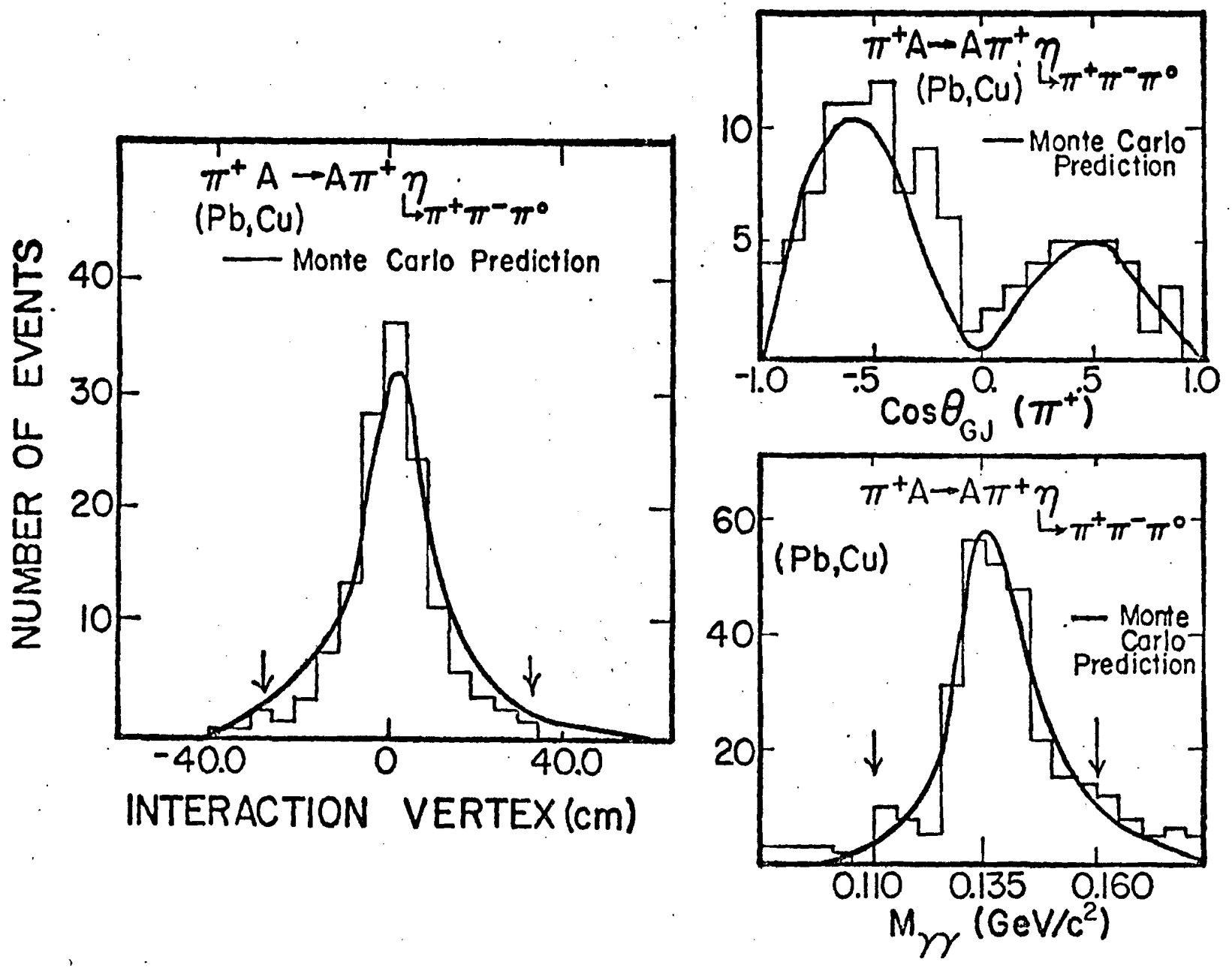
$\pi^+ A \to A\pi^+ \eta$
(Pb,Cu)
$\hookrightarrow \pi^+\pi^-\pi^0$
Monte Carlo Prediction
NUMBER OF EVENTS
40
30
20
10
-40.0
0
40.0
INTERACTION VERTEX (cm)
$\pi^+ A \to A\pi^+ \eta$
(Pb,Cu)
$\hookrightarrow \pi^+\pi^-\pi^0$
Monte Carlo Prediction
10
5
-1.0
-.5
0.
.5
1.0
$\cos\theta_{GJ}$ (π^+)
$\pi^+ A \to A\pi^+ \eta$
$\hookrightarrow \pi^+\pi^-\pi^0$
(Pb,Cu)
Monte Carlo Prediction
60
40
20
0.110
0.135
0.160
$M_{\gamma\gamma}$ (GeV/c^2)

Figure 42

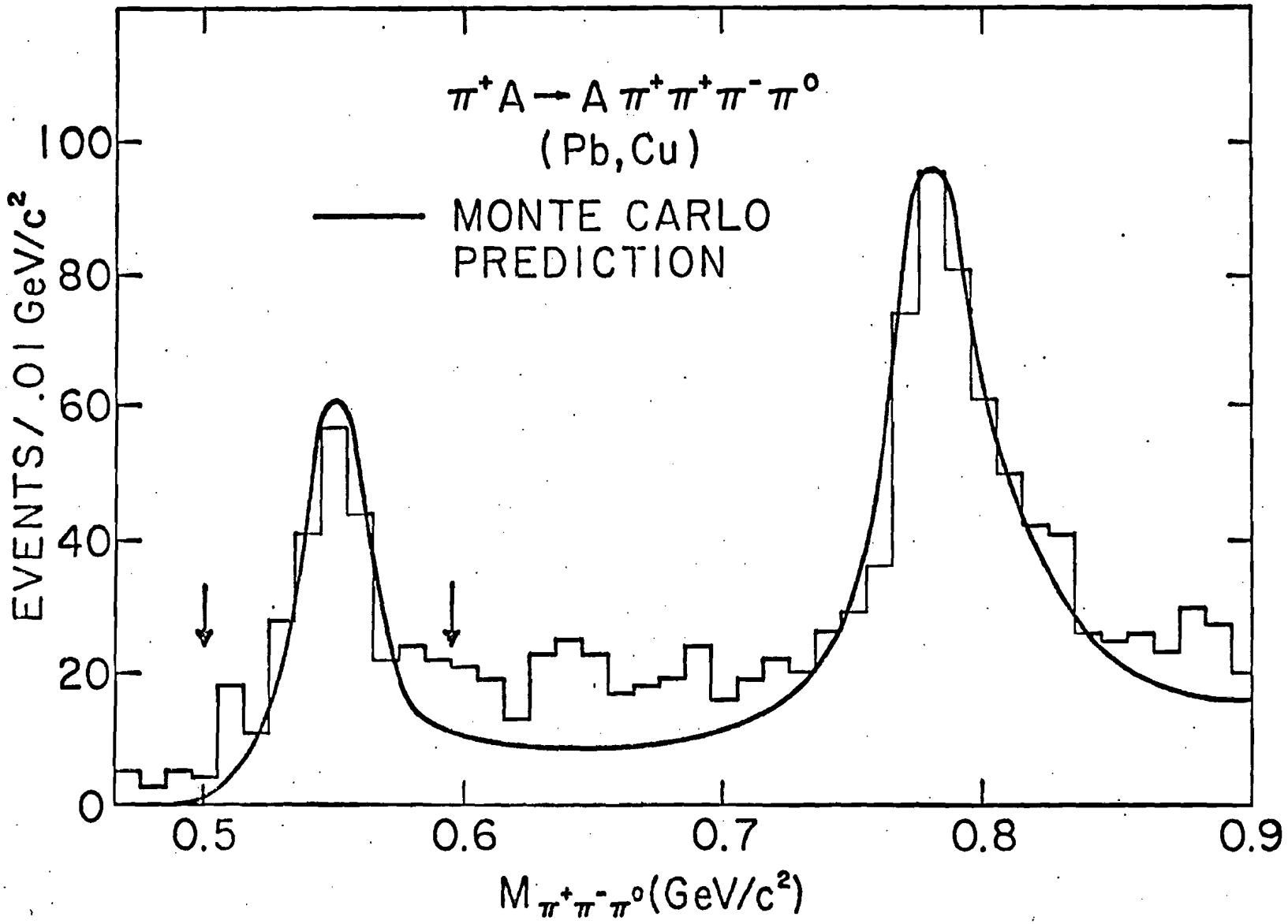
$\pi^+ A \rightarrow A \pi^+ \pi^+ \pi^- \pi^0$
(Pb,Cu)
MONTE CARLO
PREDICTION
EVENTS/.01 GeV/c²
100
80
60
40
20
0
0.5
0.6
0.7
0.8
0.9
$M_{\pi^+\pi^-\pi^0}$(GeV/c²)

Figure 43

(iv) mentioned above. Both the η peak and the ω peak, which is due to $B^+(1235)$ decaying into $\omega\pi^+$, are seen clearly. The Monte Carlo prediction agrees well with the real data. The tail on the higher side of the η peak is mostly due to pions from ω decays interfered with the $\pi^+\pi^-\pi^0$ formation for η. This effect does not of course present in the Monte Carlo prediction as strongly as in the real data. It was simulated by mixing the events generated for both types of decays. A small t or $\pi^+\pi^+\pi^-\pi^0$ mass cut eliminates this background considerably.

We have also studied the decays of A_2^+ into two kaons via the Reaction (13). The $K^+K_S^0$ mass distributions shown in Figure 44 for the lead and the copper targets indicate that Reaction (13) is dominated by the production of $A_2^+(1310)$ and possibly by another state at about 1440 Mev/c^2 (see Section C for more details). Cuts (i), (ii) and (vi) on total energy, interaction vertex and $\pi^+\pi^-$ mass were imposed on the data. Also, K_S^0 was required to decay in the decay tank.

Figure 45 shows the reconstructed total energy of these events without the requirement (i). The total energy was defined to be the summation of the energies of three charged particles. Therefore the lower tail in the distributions are the events with three charged particles with any number of photons. They can mostly be eliminated by an A_2^+ mass cut

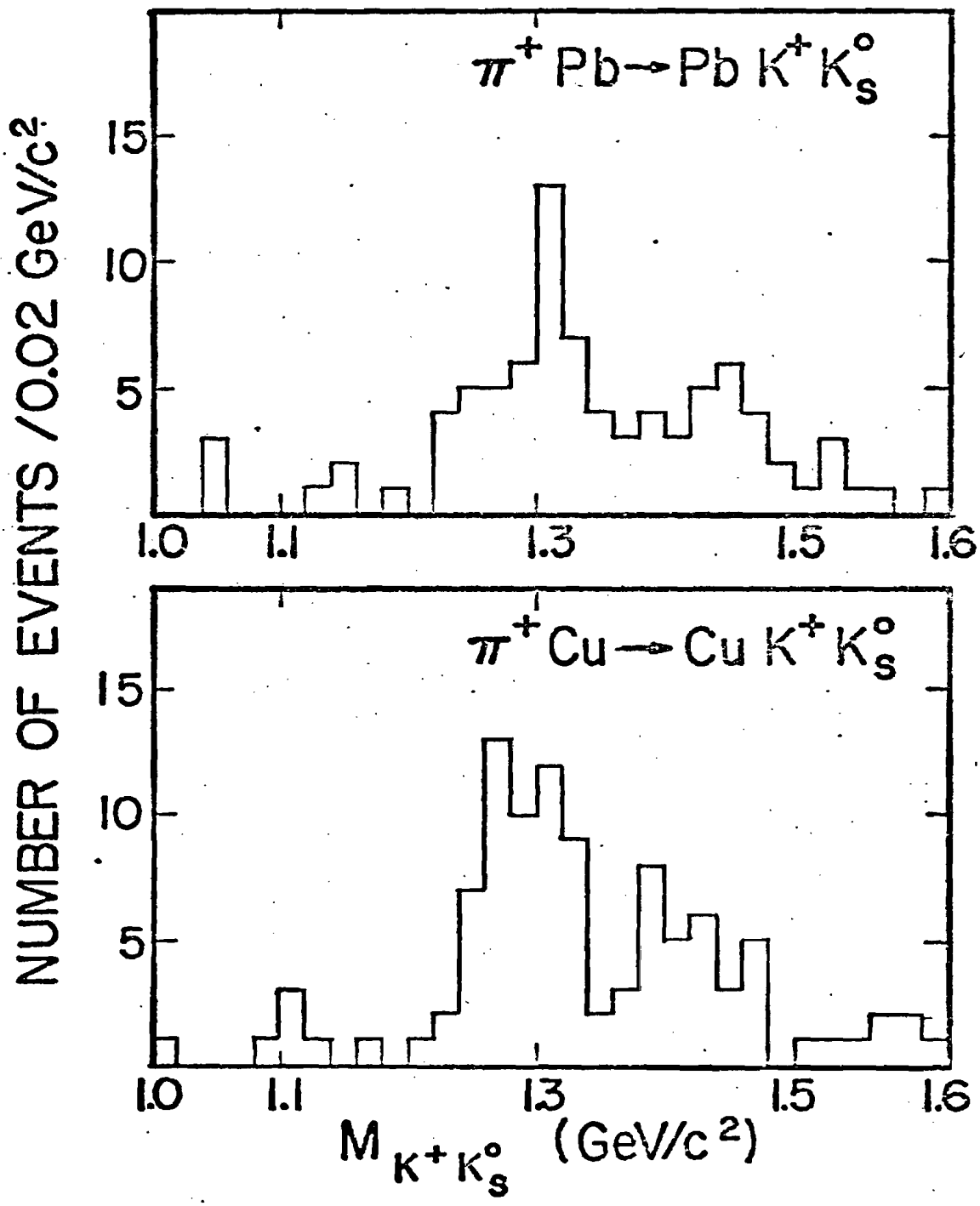
$\pi^+ Pb \rightarrow Pb\, K^+ K^0_s$
$\pi^+ Cu \rightarrow Cu\, K^+ K^0_s$
NUMBER OF EVENTS /0.02 GeV/c²
15
10
5
1.0
1.1
1.3
1.5
1.6
$M_{K^+ K^0_s}$ (GeV/c²)

Figure 44

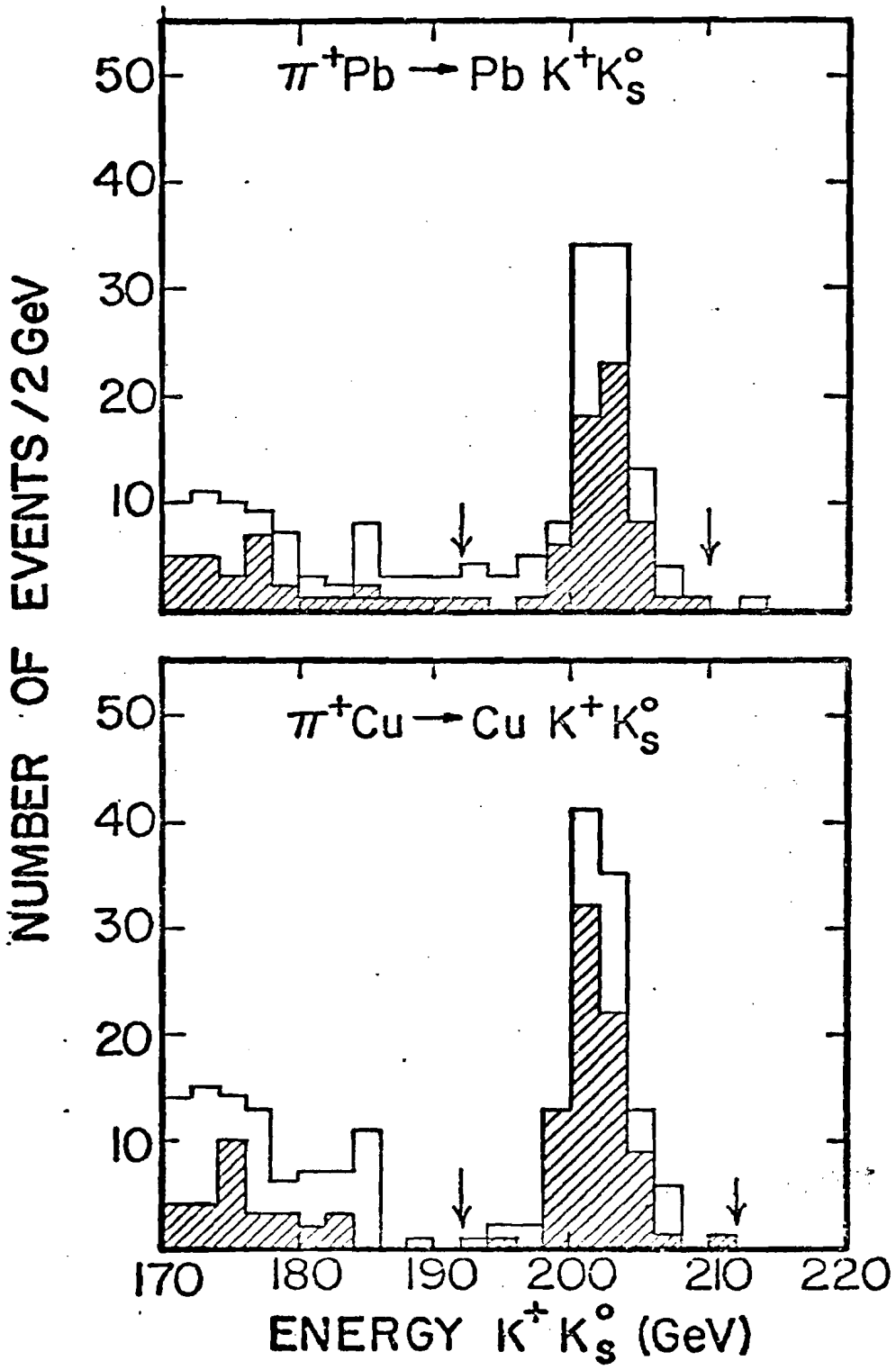
$\pi^+Pb \rightarrow Pb\ K^+K^o_s$
$\pi^+Cu \rightarrow Cu\ K^+K^o_s$
NUMBER OF EVENTS /2 GeV
50
40
30
20
10
170
180
190
200
210
220
ENERGY $K^+K^o_s$ (GeV)

Figure 45

in the range 1.20 - 1.38 Gev/c^2. The shaded histograms show the events surviving the mass cut.

The interaction vertex distribution is shown in Figure 46a for the lead target. The data were corrected for empty target and required to have $t \leqslant 0.005$ $(Gev/c)^2$, to ensure the coherent Coulomb production of A_2^+, in addition to the cuts (i) and (vi). The Monte Carlo prediction is observed to be in good agreement with the data.

The angular distribution of the decays of the A_2^+ candidates in the Gottfried-Jackson frame is presented in Figure 46b. The data have all the cuts mentioned above plus an A_2^+ mass within the range 1.20 - 1.38 Gev/c^2. As expected, we observe a $\sin^2\theta \cos^2\theta$ dependence of these decays.

Figure 46c shows the $\pi^+\pi^-$ (K_S^0) mass distribution for the lead target data. The events in this distribution survived the cuts (i) on total energy and (ii) on interaction vertex, two pions were also required to form a vertex inside the decay tank.

So far, we did not make any distinction between the two peaks of the histograms of Figure 44. This, after all, did not manifest itself while we were discussing various

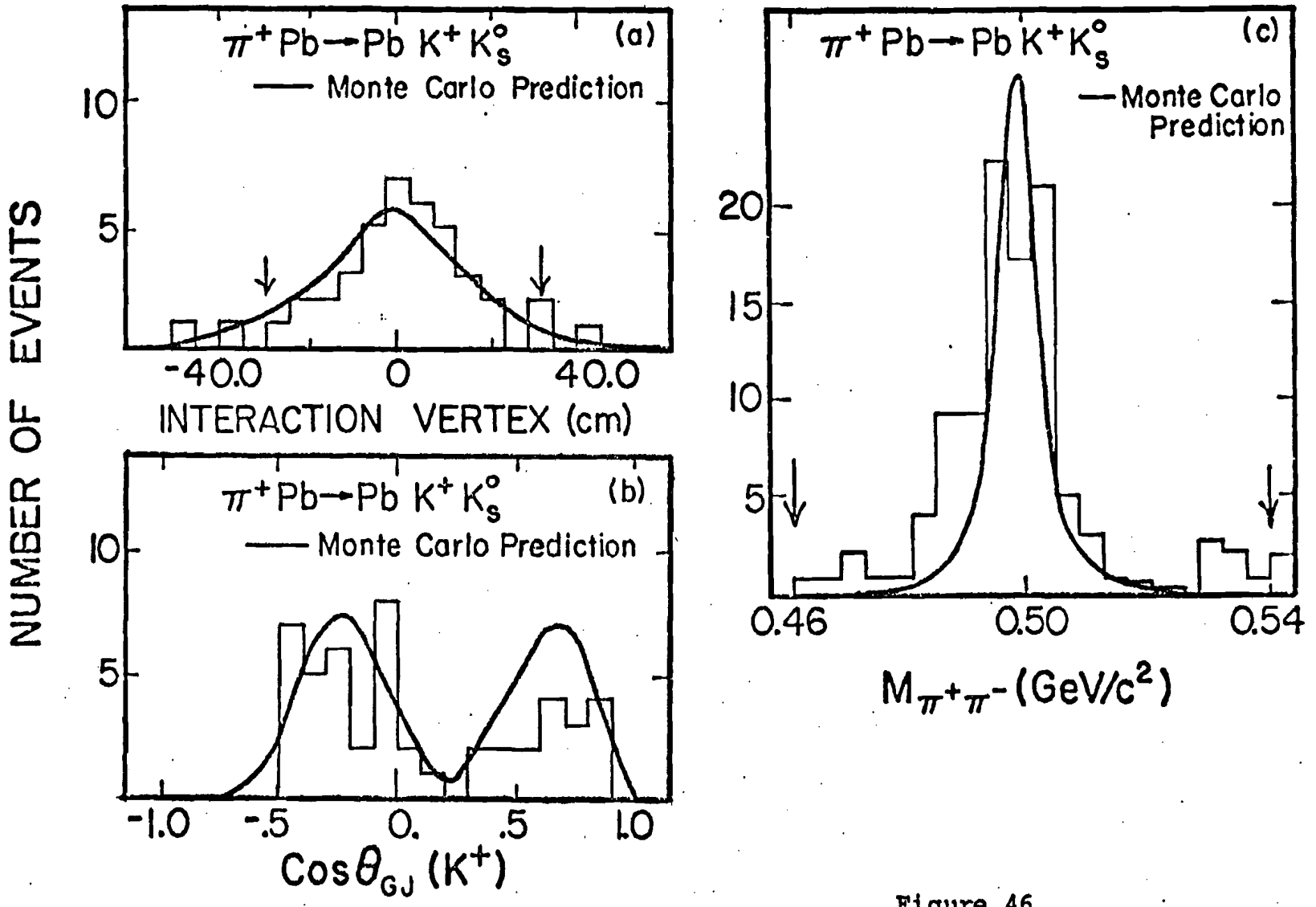
$\pi^+ Pb \to Pb\ K^+ K^0_s$
(a)
Monte Carlo Prediction
10
5
-40.0
0
40.0
INTERACTION VERTEX (cm)
NUMBER OF EVENTS
$\pi^+ Pb \to Pb\ K^+ K^0_s$
(b)
Monte Carlo Prediction
10
5
-1.0
-.5
0.
.5
1.0
$\cos\theta_{GJ}(K^+)$
$\pi^+ Pb \to Pb\ K^+ K^0_s$
(c)
Monte Carlo Prediction
20
15
10
5
0.46
0.50
0.54
$M_{\pi^+\pi^-}$ (GeV/c^2)

Figure 46

parameters of the Reaction (13) such as total energy, interaction vertex, K_S^0 mass and angular distributions of the A_2^+ decays. In other words, there are no indications that the second peak with higher mass value is an artifact of some error in the kinematics of the analysis or a source of background that we do not understand. However, the events in this second peak were studied thoroughly for all possible errors. They were made sure to contain K_S^0 's that decay in the decay tank, to have no missing energy, to be originated at the target, and observed to have an angular distribution in the Gottfried-Jackson frame like $J^P=2^+$ particles. We should point out that the first peak is at the same place as the resonances observed in the Reactions (12a) and (12b) (see Figures 53 and 54) and remind that there are earlier experiments reporting observations of similar higher peak in the same mass distribution[35].

The results of mass fittings and further tests on the reality of the second peak are discussed in Sections C and D.

B. $K^{*+}(1430)$ DATA

The Primakoff production of $K^{*+}(1430)$ was studied via Reactions (14) and (15). The $K^{*+}(890)$ meson is produced simultaneously and decays in the same modes. We observe them together in mass distributions (see Figures 47 and 50). Their mass values are sufficiently different to separate them. For the discussions in this section, $K^{*+}(1430)$ is defined in Reaction (14) with $K^+\pi^0$ mass and in Reaction (15) with $K_S^0\pi^+$ mass within 1.22 Gev/c^2 and 1.64 Gev/c^2. We discuss here only the $K^{*+}(1430)$ production, the details of the analysis on $K^{*+}(890)$ can be found elsewhere[31].

The $K^+\pi^0$ mass distributions shown in Figure 47 are clear indications of the production of $K^{*+}(1430)$ (and K (890) too) in Reaction (14). The data were required to have the cuts (i), (ii) and (iv) on total energy, interaction vertex and two photon mass, respectively.

The reconstructed total energy is shown in Figures 48a and 48b for the data from the lead and the copper targets with the cut (i) removed. The interaction vertex distribution is presented in Figure 48c for the lead target events. The Monte Carlo prediction is in good agreement with the data. There, the data have the cuts (i) and (iv) and in addition, the requirement $t \lesssim 0.005$ (Gev/c)^2 to ensure

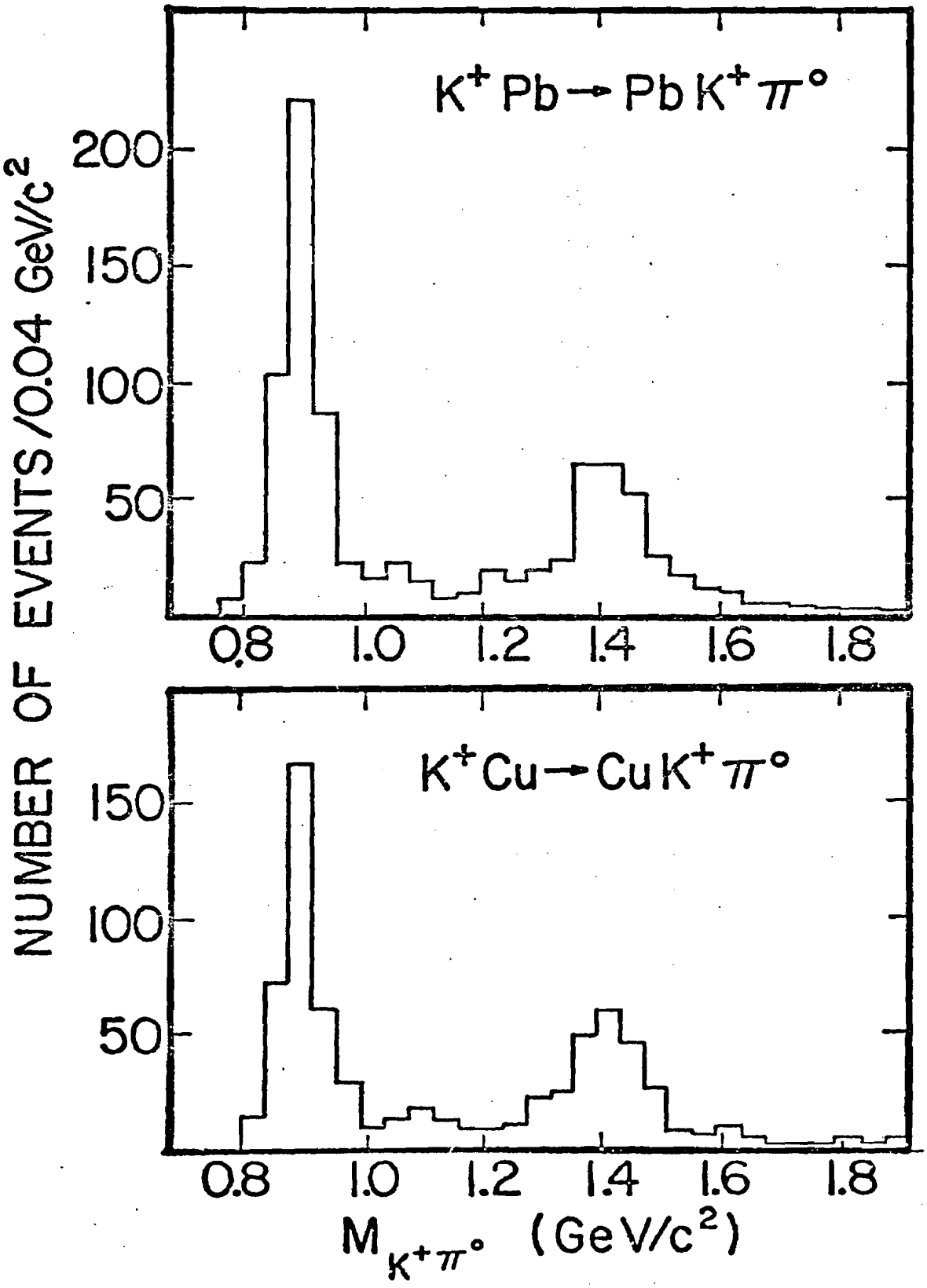
K+ Pb → Pb K+ π°
K+ Cu → Cu K+ π°
NUMBER OF EVENTS /0.04 GeV/c²
200
150
100
50
0.8
1.0
1.2
1.4
1.6
1.8
M K+π° (GeV/c²)

Figure 47

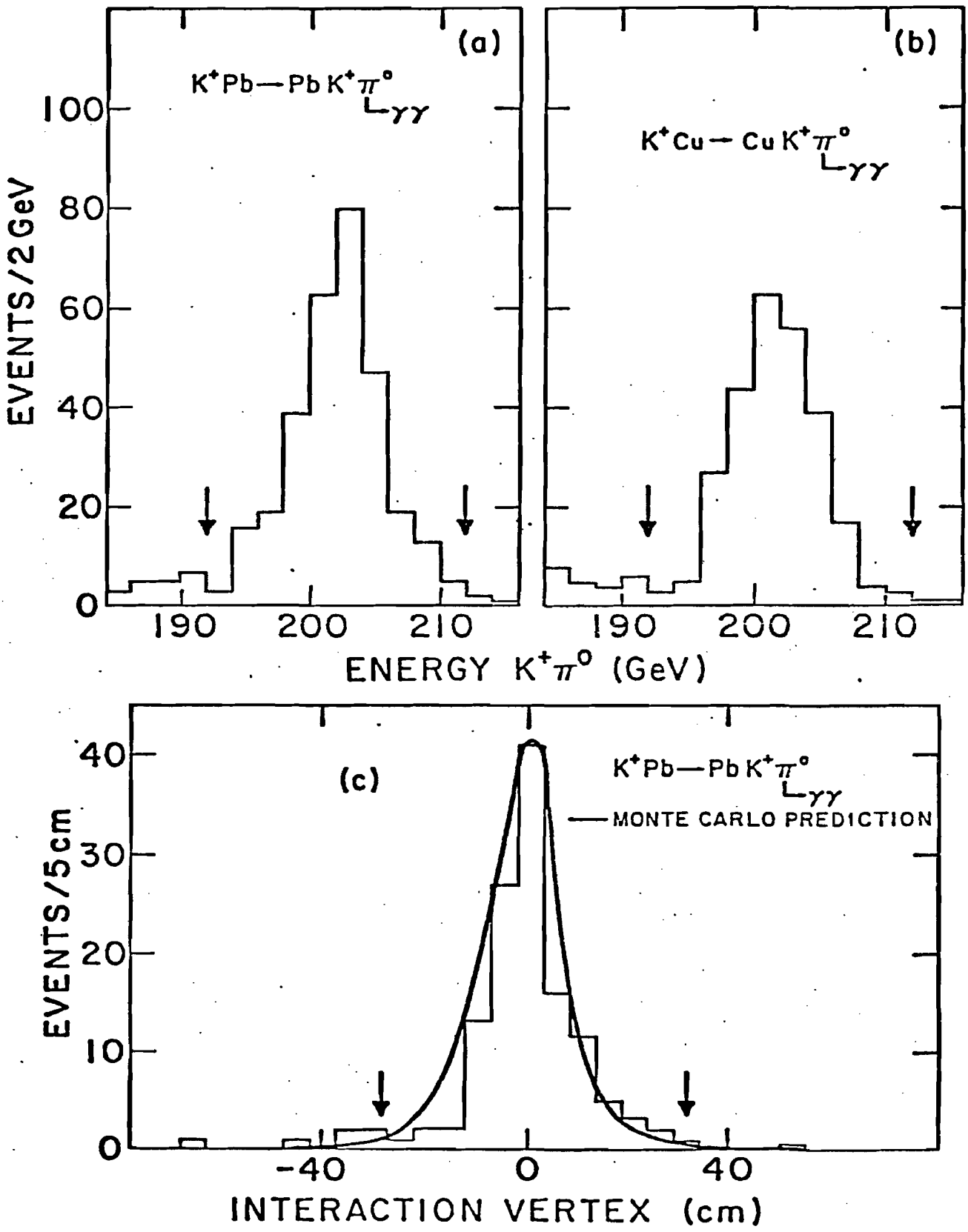
(a)
K⁺Pb—Pb K⁺π°
└γγ
(b)
K⁺Cu— Cu K⁺π°
└γγ
EVENTS/2GeV
100
80
60
40
20
0
190
200
210
ENERGY K⁺π° (GeV)
(c)
K⁺Pb—Pb K⁺π°
└γγ
MONTE CARLO PREDICTION
EVENTS/5cm
40
30
20
10
0
-40
0
40
INTERACTION VERTEX (cm)

Figure 48

the coherent Coulomb production. The data have been corrected for empty target effects. Figure 49a shows the decay angular distribution of the events of Figure 47 on the lead target, with a $K^{*+}(1430)$ mass in the range 1.22 - 1.64 Gev/c^2, in the Gottfried-Jackson frame. The Monte Carlo prediction is in good agreement with the data. Figure 49b presents the two photon mass distribution of the events obtained from the lead target. Again the Monte Carlo correctly predicts the experimental distribution.

The $K_s^0\pi^+$ ($K_s^0 \rightarrow \pi^+\pi^-$) mass distributions shown in Figure 50 indicate that Reaction (15) is also dominated by the production of $K^{*+}(1430)$ (and $K^{*+}(890)$). The data were required to have the cuts (i) on total energy, (ii) on interaction vertex and (vi) on K_s^0 mass. The two pions of K_s^0 are also required to form a vertex in the decay tank.

Figure 51a and 51b show the reconstructed total energy distributions of these events without the cut (i). The total energy was defined as the sum of the energies of all three charged particles in these events. The low energy tails are therefore due to the events with three charged particles and any number of photons. A $K^{*+}(1430)$ mass cut within 1.22 and 1.64 Gev/c^2 eliminates most of these events and the shaded distributions are obtained.

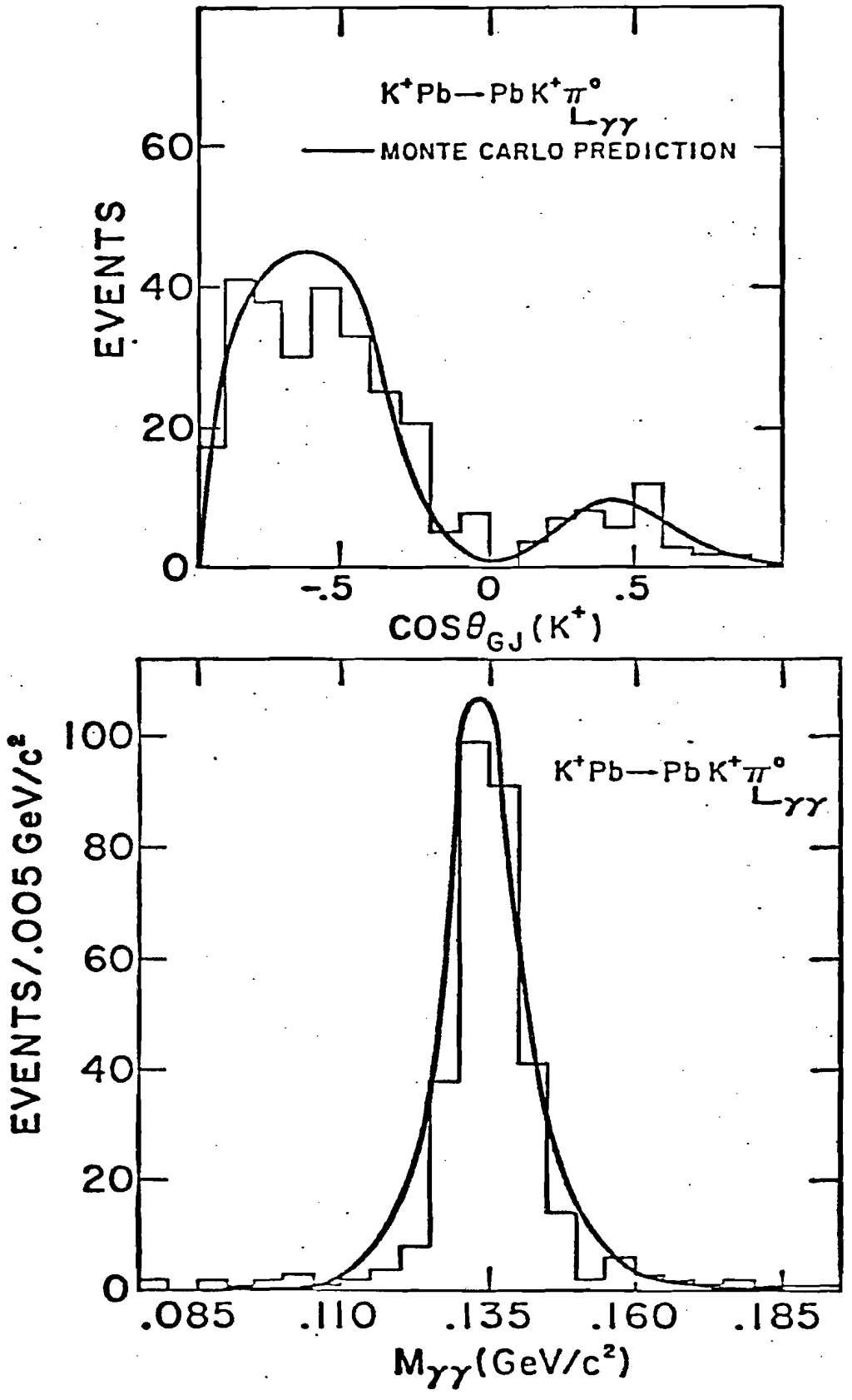
K⁺Pb—Pb K⁺π°
└γγ
MONTE CARLO PREDICTION
EVENTS
60
40
20
0
-.5
0
.5
COSθ_GJ (K⁺)
EVENTS/.005 GeV/c²
100
80
60
40
20
0
K⁺Pb—Pb K⁺π°
└γγ
.085
.110
.135
.160
.185
M_γγ(GeV/c²)

Figure 49

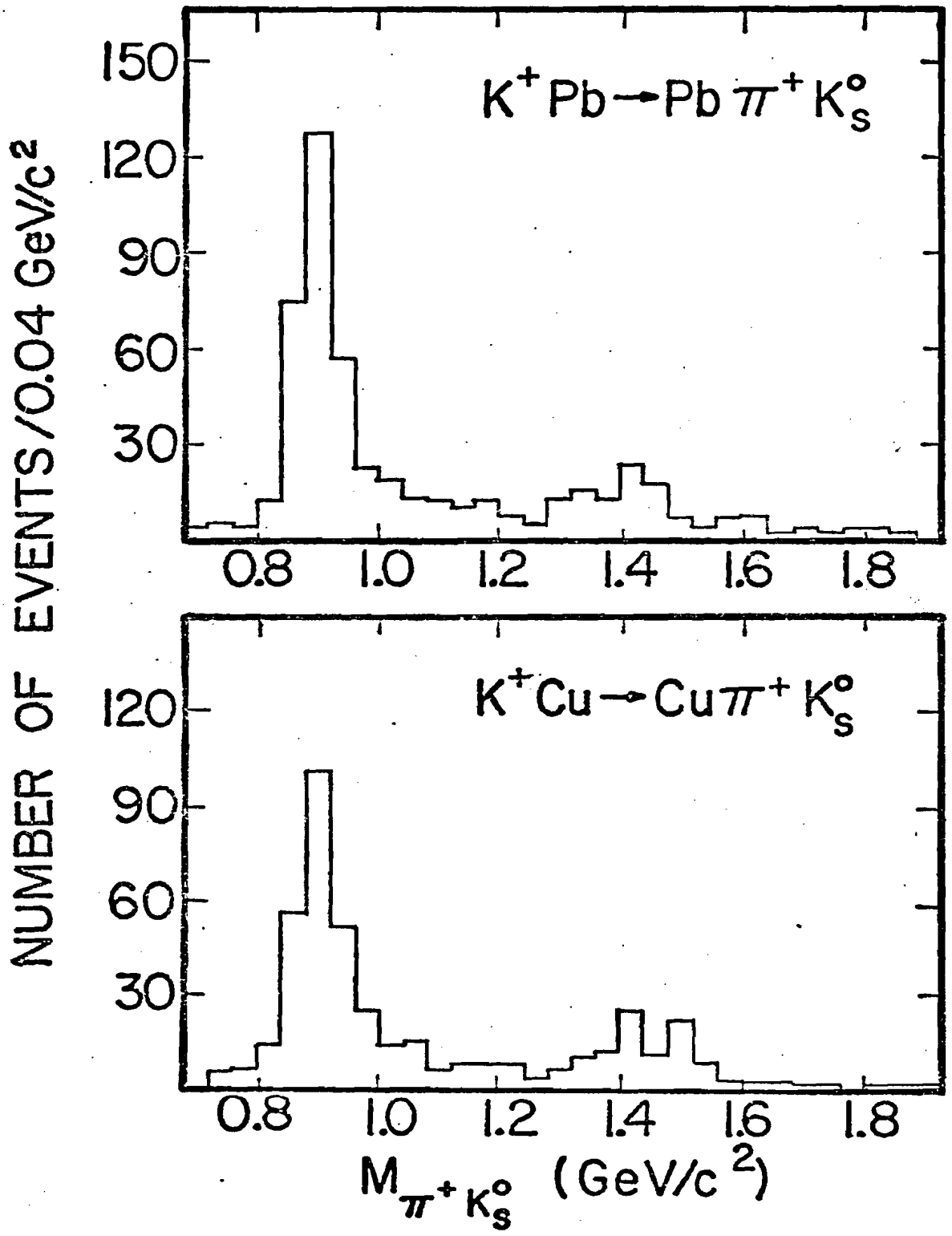
$K^+Pb \rightarrow Pb\,\pi^+ K^o_s$
$K^+Cu \rightarrow Cu\,\pi^+ K^o_s$
NUMBER OF EVENTS/0.04 GeV/c^2
150
120
90
60
30
0.8
1.0
1.2
1.4
1.6
1.8
$M_{\pi^+ K^o_s}$ (GeV/c^2)

Figure 50

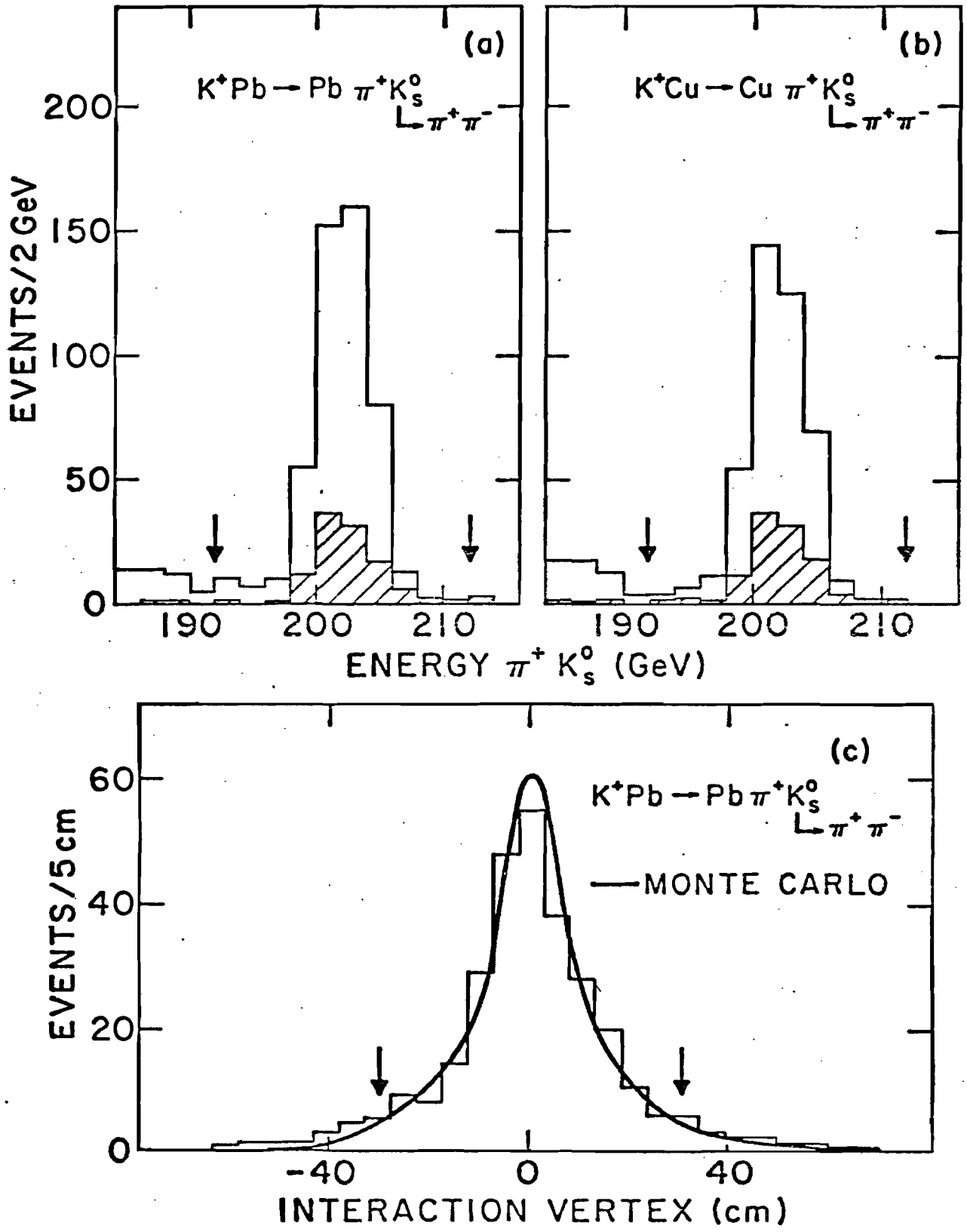
(a)
$K^+Pb \rightarrow Pb\ \pi^+K^0_s$
$\hookrightarrow \pi^+\pi^-$
(b)
$K^+Cu \rightarrow Cu\ \pi^+K^0_s$
$\hookrightarrow \pi^+\pi^-$
EVENTS/2 GeV
200
150
100
50
0
190
200
210
ENERGY $\pi^+ K^0_s$ (GeV)
(c)
$K^+Pb \rightarrow Pb\ \pi^+K^0_s$
$\hookrightarrow \pi^+\pi^-$
MONTE CARLO
EVENTS/5 cm
60
40
20
0
-40
0
40
INTERACTION VERTEX (cm)

Figure 51

The interaction vertex distribution is presented in Figure 51c for the lead target events with the cut (ii) removed. Again, the data have $t \lesssim 0.005$ $(Gev/c)^2$ and been corrected for empty target. The Monte Carlo prediction agrees fairly well with the data. The angular distribution of the $K^{*+}(1430)$ decays in the Gottfried-Jackson frame is shown in Figure 52a for the lead target. In addition to the cuts (i), (ii) and (vi) mentioned above, the data were required to have a $K^{*+}(1430)$ mass within 1.22 and 1.64 Gev/c^2.

Figure 52b presents the mass distribution of two pions that form a vertex in the decay tank. The data which were obtained from the lead target, were imposed the cuts (i) and (ii). The Monte Carlo prediction seems to agree reasonably well with the data.

The results of the mass fittings for $K^{*+}(1430)$ is discussed in Section C.

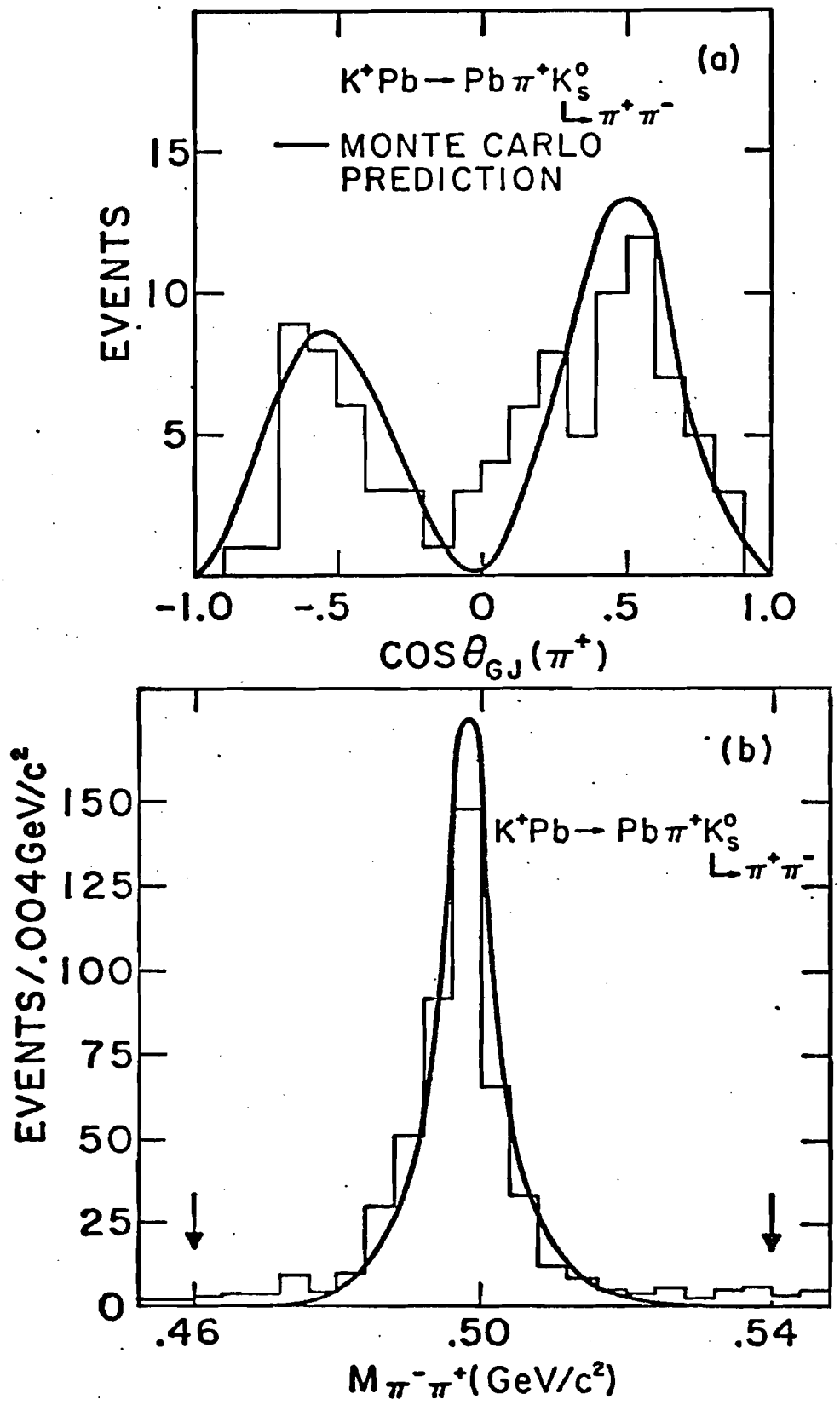
(a)
K⁺Pb → Pb π⁺ K⁰s
└ π⁺ π⁻
MONTE CARLO PREDICTION
EVENTS
15
10
5
-1.0
-.5
0
.5
1.0
cos θGJ (π⁺)
(b)
K⁺Pb → Pb π⁺ K⁰s
└ π⁺ π⁻
EVENTS/.004GeV/c²
150
125
100
75
50
25
0
.46
.50
.54
Mπ⁻π⁺(GeV/c²)

Figure 52

C. MASS SPECTRA

The cross section for the Coulomb production of a system a of mass M_{a^*} in the reaction a + A --> A + a^* is given by[36]

$$\frac{d\sigma}{dt\,dM_{a^*}^2} = \frac{Z^2\alpha}{\pi}\,\frac{\sigma_\gamma(M_{a^*}^2)}{(M_{a^*}^2 - M_a^2)}\,\frac{t-t_{min}}{t^2}\,\left|F_{EM}(t)\right|^2 \qquad (16)$$

where Z is the nuclear charge, $F_{EM}(t)$ is the effective nuclear form factor, containing absorption of incoming and outgoing states in nuclear matter (look Chapter I for details). $\sigma_\gamma(M_{a^*}^2)$ represents the cross section for the reaction γa --> a^* at a center of mass energy M_{a^*} and given by

$$\sigma_\gamma(M_{a^*}^2) = \frac{2\pi}{q^{*2}}\,\frac{(2S_{a^*}+1)}{(2S_a+1)}\,\left|T(\gamma a \to a^*)\right|^2 \qquad (17)$$

Here, S_a and S_{a^*} are the spins of the incident and the produced systems, respectively; q^* is the momentum of the photon in the center of mass system of a^*:

$$q^* = \frac{M_{a^*}^2 - M_a^2}{2M_{a^*}}$$

Integration of Equation (16) over t, and substitution of Equation (17) for σ_γ yields

$$\frac{d\sigma}{dM_{a^*}^2} \propto P_{inc}^2 t_{max} Z^2 \frac{M_{a^*}^2}{(M_{a^*}^2 - M_a^2)^3} |T(\gamma a \to a^*)|^2 \tilde{F}(M_{a^*}^2) \qquad (18)$$

where t_{max} is the maximum range of integration. $\tilde{F}(M^2)$ is a slowly varying function and comes from the integration of the electromagnetic form factor over t. It accounts for the mass dependent absorption of the a^* system and calculated by using the optical model as described in Chapter I. The value t_{max}=0.01 $(Gev/c)^2$ was chosen to emphasize the Coulomb contribution to A_2^+ or $K^{*+}(1430)$ production.

The T-matrix in Equation (18) has a D-wave Breit-Wigner resonance form[37]:

$$|T(\gamma a \to a^*)|^2 = \frac{M_0^2 \Gamma_{\gamma a}(M^2)\, \Gamma_{a^*}(M^2)}{(M^2 - M_0^2)^2 + M_0^2 \Gamma_{a^*}(M^2)} \qquad (19)$$

where Γ_{a^*} and $\Gamma_{\gamma a}$ are the mass dependent partial decay widths, and M_0 is the mass at resonance.

The phenomenological forms of the partial decay widths that we used for our data and yielded the best fits to statistically more significant data on ρ^+ and $K^{*+}(890)$ of this experiment were[37,38]

$$\Gamma_{a^*} = \Gamma_0 \left(\frac{q}{q_0}\right)^{2J+1} \frac{\rho(q_0 R)}{\rho(qR)}$$

$$\Gamma_{\gamma a} = \Gamma_{\gamma 0} \left(\frac{k}{k_0}\right)^3 \frac{\rho(k_0 R)}{\rho(kR)} \quad ; \quad \Gamma_{\gamma 0} \left(\frac{k}{k_0}\right)^3 \frac{M}{M_0} \qquad (20)$$

$$\rho(qR) = q^4 R^4 + 3q^2 R^2 + 9$$

where q and k are momenta in the rest frame of the a^* and γa systems, respectively. Values at resonance are subscripted with a zero. Γ_0 is the total decay width of the resonance state, J is its total angular momentum. R is the range parameter and set to 1 fm =5 $(Gev)^{-1}$.

In the data we analyze, a^* system is $\pi^+\eta$ or $K^+K^0_S$ for the resonant state A_2^+, and $K^+\pi^0$ or $K^0_S\pi^+$ for $K^{*+}(1430)$. Their mass distributions are shown in Figures 53 - 57 with, in addition to the cuts discussed earlier, a small t of $t \leqslant 0.01$ $(Gev/c)^2$. For a better statistics, the data for the lead and the copper targets were combined. The data were corrected for empty target and geometrical acceptance of the spectrometer. The acceptance, as a function of mass, is shown by solid curves above the spectra. Using the fitting program MINUITS of CERN[39] the data were fit to the D-wave Breit-Wigner form of Equation (19) plus a linear background:

$$\frac{d\sigma}{dM} = A\left(\frac{M}{M^2-M_0^2}\right)^3 \tilde{F}(M^2)\,\frac{M_0 M\,\Gamma_{\gamma a}(M^2)\,\Gamma_{a^*}(M^2)}{(M_0^2-M^2)^2+M_0^2\,\Gamma_{a^*}(M^2)} + C_1 M + C_2 \qquad (21)$$

The accuracy of the fits is limited by the low statistics of the data. The following is the results we obtained:

1) $A_2^+ \to \pi^+\eta$ ($\eta \to \gamma\gamma$) mode:

Γ_0 =98 +/- 14 Mev,

M_0 =1312 +/- 9 Mev/c^2,

χ^2=26.0/30 (degree of freedom=dof)$^{-1}$.

2) $A_2^+ \rightarrow \pi^+\eta$ ($\eta \rightarrow \pi^+\pi^-\pi^0$) mode:

The data on this mode had a very low statistics and an unclear background. Also, separation of these events from more redundant, and topologically similar, events of $B^+(1235) \rightarrow \pi^+\omega$ (followed by $\omega \rightarrow \pi^+\pi^-\pi^0$) decay was not certain. These facts are reflected by the fitting results presented below.

Γ_0=140 +/- 82 Mev,
M_0=1302 +/- 14 Mev/c^2,
χ^2=7.9/7 (dof)$^{-1}$.

3) $A_2^+ \rightarrow K^+K_S^0$ ($K_S^0 \rightarrow \pi^+\pi^-$) mode:

For this mode, we fit the data to single and double resonance forms of Equation (21). In the double resonance fit, the higher mass state is represented by subscript x.

a) Double Resonance Fit:

Γ_0=85 +/- 46 Mev,
M_0=1309 +/- 9 Mev/c^2,
Γ_{0x}=52 +/- 32 Mev,
M_{0x}=1447 +/- 15 Mev/c^2,
χ^2=2.5/5 (dof)$^{-1}$.

b) Single Resonance Fit:

Γ_0 =99 +/- 48 Mev,

M_0=1314 +/- 11 Mev/c^2,

χ^2=14.0/10 $(dof)^{-1}$.

4) $K^{*+}(1430) \rightarrow K^+\pi^0$ ($\pi^0 \rightarrow \gamma\gamma$) mode:

Γ_0 =105 +/- 14 Mev,

M_0=1434 +/- 7 Mev/c^2,

χ^2=15.6/14 $(dof)^{-1}$.

5) $K^{*+}(1430) \rightarrow K^0_s\pi^+$ ($K^0_s \rightarrow \pi^+\pi^-$) mode:

Γ_0=94 +/- 28 Mev,

M_0=1423 +/- 10 Mev/c^2,

χ^2=6.7/9 $(dof)^{-1}$.

These fits are shown by solid curves in the corresponding figures. Arrows indicate the mass cuts used in t-distribution fits.

We see that the single resonance fit to Reaction (13) has a ~20% confidence level. The confidence level of the double resonance fit to the same data is ~75%. Fit to the data from Reaction (12a), where we have a single peak only, has a confidence level of ~80%. Therefore the double resonance fit to Reaction (13) is more consistent with the fit to Reaction (12a) data where we do not see a second

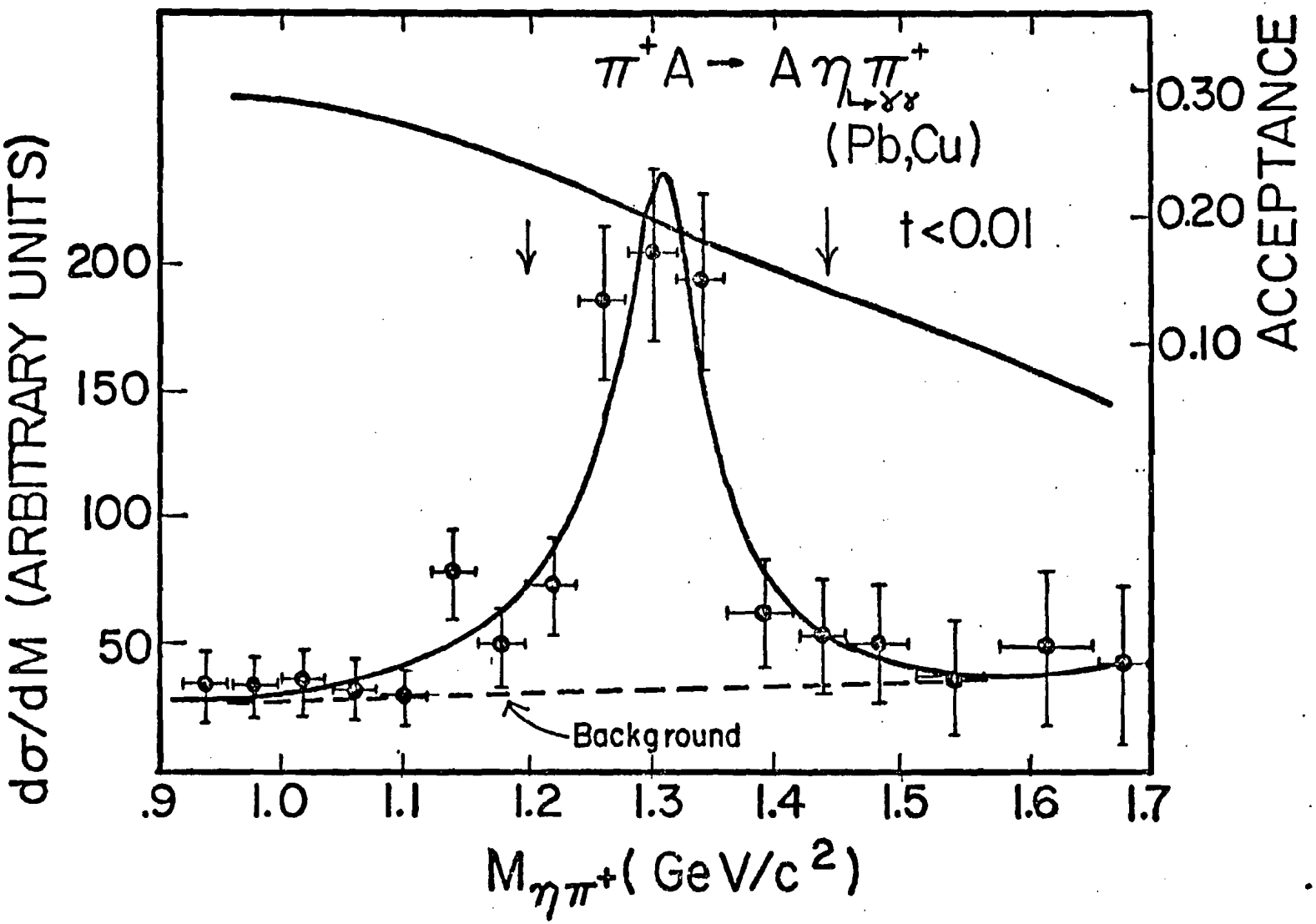
$\pi^+ A \to A \eta \pi^+$
$\hookrightarrow \gamma\gamma$
(Pb,Cu)
t<0.01
Background
dσ/dM (ARBITRARY UNITS)
200
150
100
50
.9
1.0
1.1
1.2
1.3
1.4
1.5
1.6
1.7
$M_{\eta\pi^+}$ (GeV/c^2)
0.30
0.20
0.10
ACCEPTANCE

Figure 53

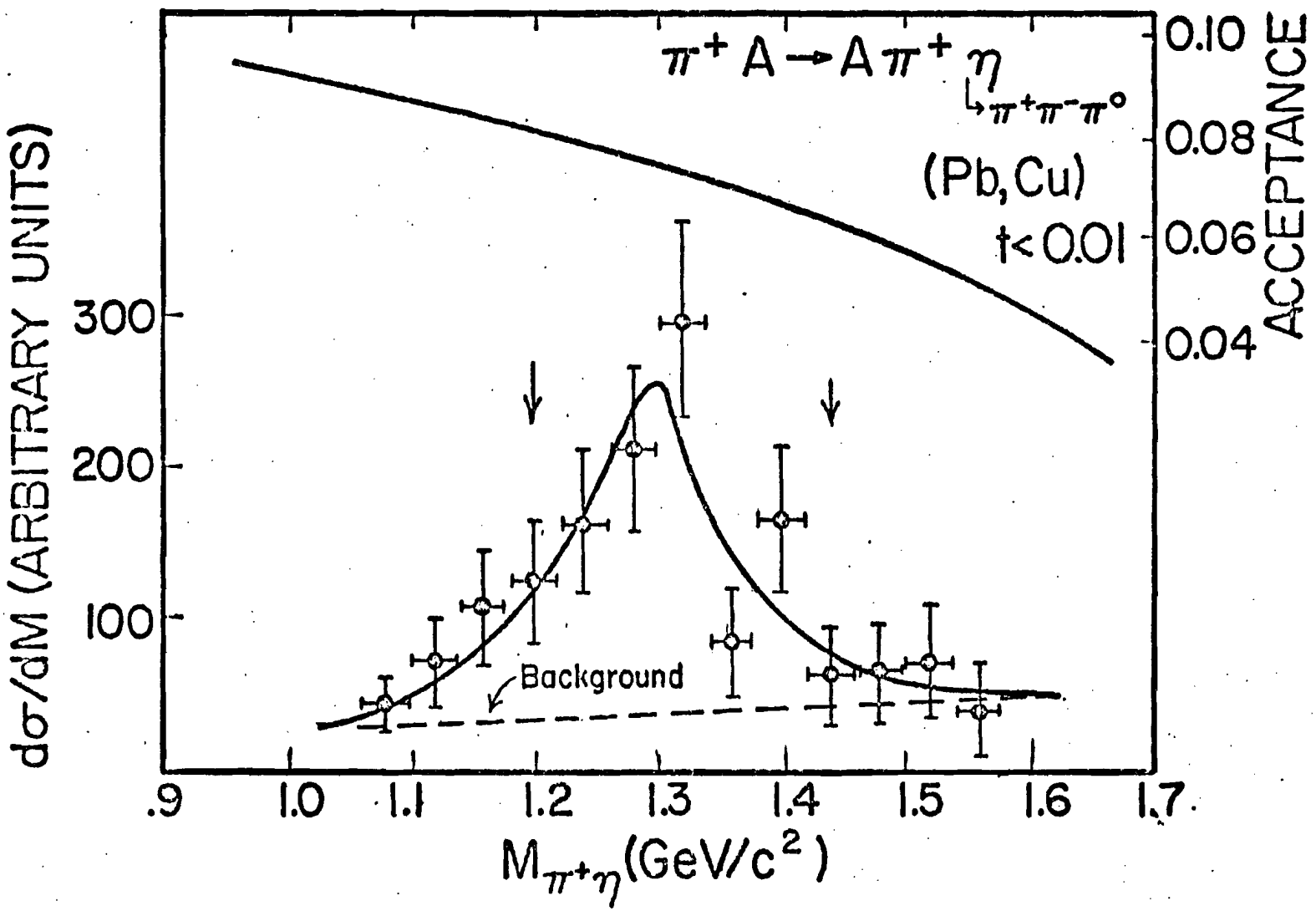
$\pi^+ A \rightarrow A \pi^+ \eta$
$\hookrightarrow \pi^+\pi^-\pi^0$
(Pb, Cu)
t< 0.01
Background
$d\sigma/dM$ (ARBITRARY UNITS)
ACCEPTANCE
$M_{\pi^+\eta}$ (GeV/c^2)
300
200
100
0.10
0.08
0.06
0.04
.9
1.0
1.1
1.2
1.3
1.4
1.5
1.6
1.7

Figure 54

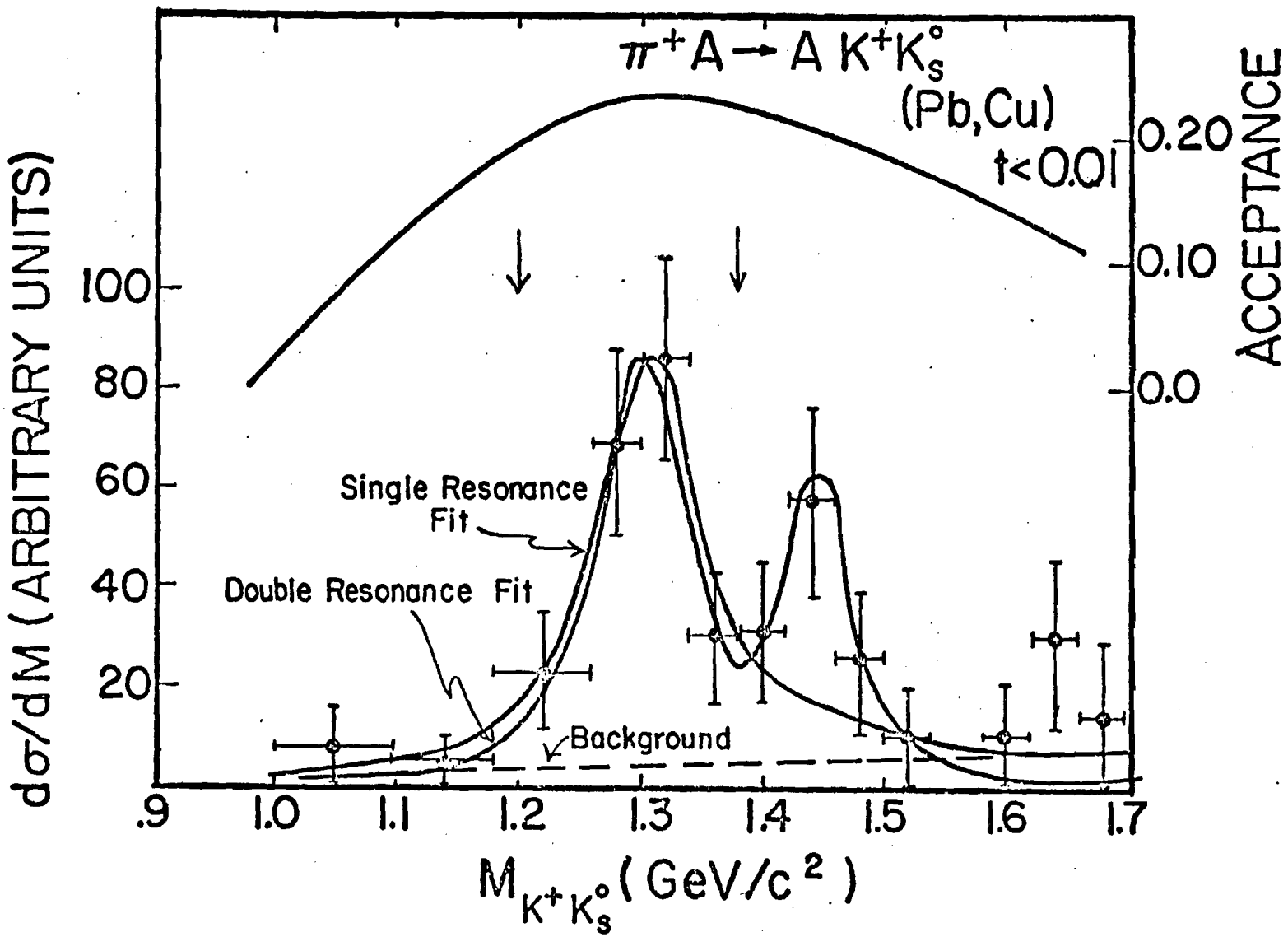
$\pi^+ A \rightarrow A K^+ K_s^\circ$
(Pb,Cu)
t<0.01
ACCEPTANCE
0.20
0.10
0.0
dσ/dM (ARBITRARY UNITS)
100
80
60
40
20
Single Resonance Fit
Double Resonance Fit
Background
.9
1.0
1.1
1.2
1.3
1.4
1.5
1.6
1.7
$M_{K^+K_s^\circ}$ (GeV/c²)

Figure 55

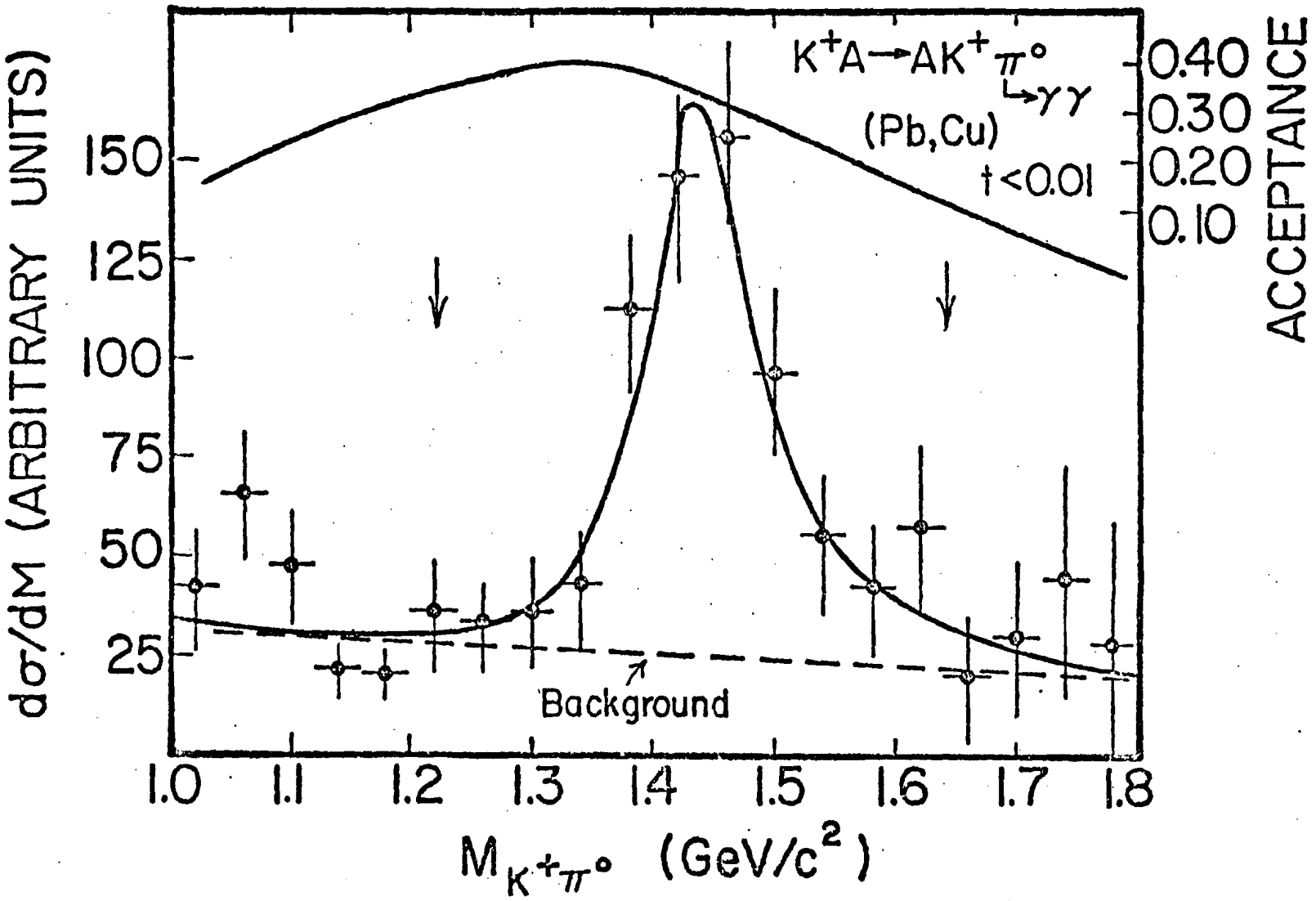
$K^+A \rightarrow AK^+\pi^0$
$\hookrightarrow \gamma\gamma$
(Pb,Cu)
$t<0.01$
Background
$d\sigma/dM$ (ARBITRARY UNITS)
ACCEPTANCE
$M_{K^+\pi^0}$ (GeV/c^2)
150
125
100
75
50
25
0.40
0.30
0.20
0.10
1.0
1.1
1.2
1.3
1.4
1.5
1.6
1.7
1.8

Figure 56

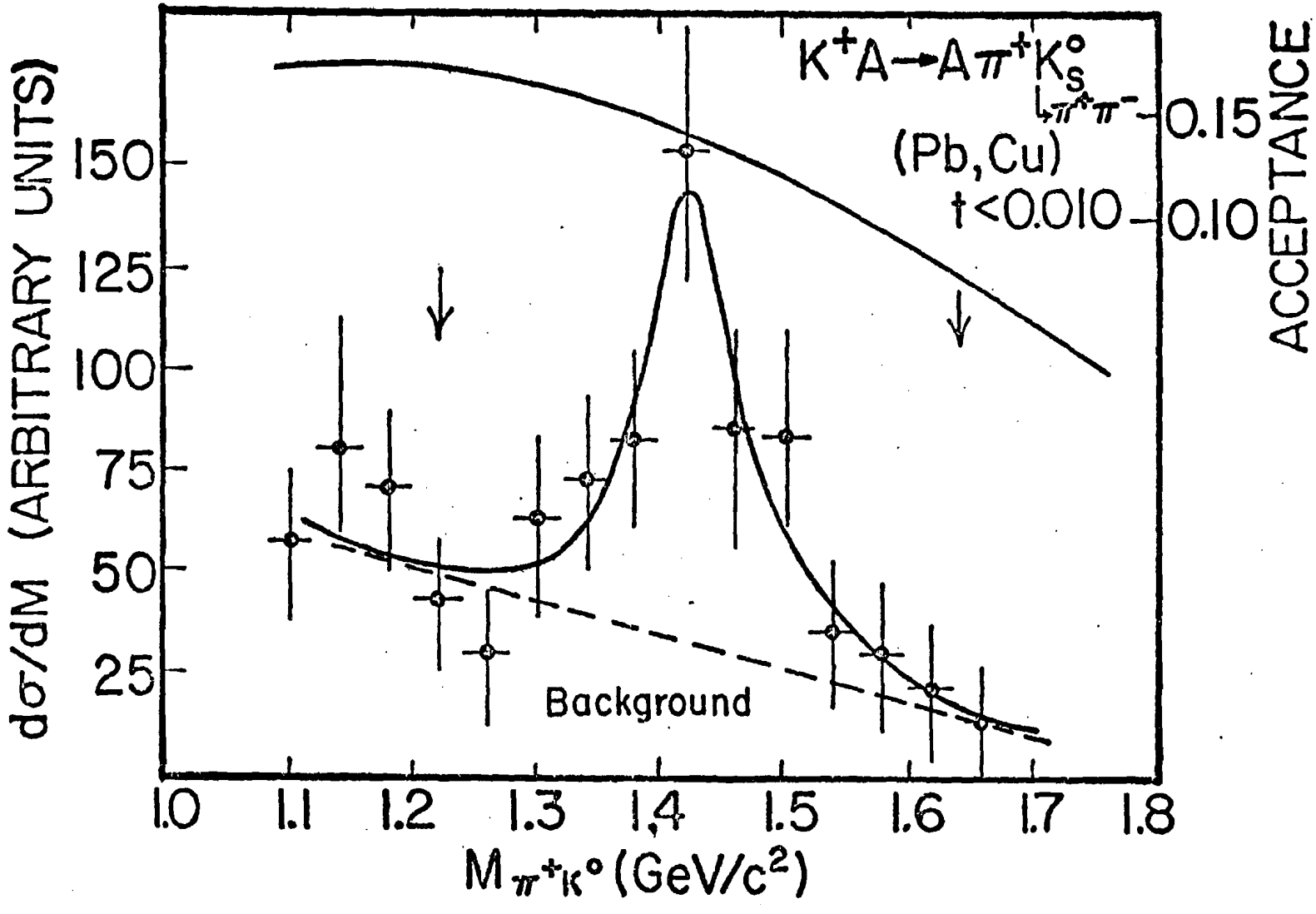
$K^+A \rightarrow A\pi^+K^0_S$
$\hookrightarrow \pi^+\pi^-$
(Pb,Cu)
t<0.010
Background
dσ/dM (ARBITRARY UNITS)
ACCEPTANCE
150
125
100
75
50
25
0.15
0.10
1.0
1.1
1.2
1.3
1.4
1.5
1.6
1.7
1.8
$M_{\pi^+K^0}$ (GeV/c²)

Figure 57

peak. Expressed in a different way, the ratio of the area under the double resonance curve within the mass range of 1.42-1.46 Gev/c^2 to the corresponding area under the single resonance curve is 3.67 +/- 1.70, which is more than one standard deviation away from unity. The width of this high mass peak, however, is larger than the one seen by K. J. Foley et al[35].

D. FITS TO t-DISTRIBUTIONS

The cross section for one interaction can be written as

$$\sigma(\text{per event}) = \frac{A}{N_0 \rho t} \frac{C.F}{\text{Incident flux}}$$

where N_0 is the Avogadro number, ρt is the thickness of the target in gm/cm^2 and A is the atomic number of the target material. The incident flux is determined by the Cerenkov and the scintillation counters as described in Chapter II.F. The correction factor (C.F) includes the geometric acceptance (averaged over a mass range of a particular reaction), the K^+ decay normalization factor and the corrections due to various losses explained in Chapter V. These correction factors are listed in Tables IVa, b, c, and d for the different targets and for the reactions we studied. The values of the cross section per event are added to these tables after a double line.

TABLE IVa

Correction Factors for the Process
$\pi^+A \rightarrow A\pi^+\eta$ ($\eta \rightarrow \gamma\gamma$)

Correction for \ Target	CU	PB
Counter Vetoes	1.381 ± 0.027	1.389 ± 0.027
Beam Absorption at Target	1.0176 ± 0.0030	1.0028 ± 0.0005
π^+ Absorption at Target	1.0176 ± 0.0030	1.0028 ± 0.0005
η Absorption at Target	1.3815 ± 0.0027	1.1776 ± 0.0030
π^+ Absorption at Spectrometer	1.0270 ± 0.0008	1.0270 ± 0.0008
η Absorption at Spectrometer	1.1403 ± 0.0028	1.1403 ± 0.0028
S-Counter Threshold	1.0060 ± 0.0006	1.0060 ± 0.0006
3-Photon	1.022 ± 0.005	1.022 ± 0.005
π^+ Decay	1.0035 ± 0.0004	1.0035 ± 0.0004
K^+- Decay Normalization	1.036 ± 0.020	1.051 ± 0.021
Geometrical Acceptance	5.952 ± 0.354	5.952 ± 0.354
Mass Cut	1.080 ± 0.020	1.103 ± 0.020
Total	15.897 ± 1.087	13.713 ± 0.941
Finite Width	1.087 ± 0.020	1.087 ± 0.020
σ (μb/event)	3.245 ± 0.349	14.968 ± 1.607

TABLE IVb

Correction Factors for the Process
$\pi^+ A \rightarrow A K^+ K_S^0$

Correction for \ Target	CU	PB
Counter Vetoes	1.381 ± 0.027	1.389 ± 0.027
Beam Absorption at Target	1.0176 ± 0.0030	1.0028 ± 0.0005
K^+ Absorption at Target	1.0163 ± 0.0030	1.0027 ± 0.0005
K_S^0 Absorption at Target	1.0163 ± 0.0030	1.0027 ± 0.0004
K^+ Absorption at Spectrometer	1.0220 ± 0.0005	1.0220 ± 0.0005
$\pi^+\pi^-$ Absorption at Spectrometer	1.0490 ± 0.0050	1.0490 ± 0.0050
S-Counter Threshold	1.0984 ± 0.0108	1.0984 ± 0.0108
2π Decay	1.0070 ± 0.0006	1.0070 ± 0.0006
K^+ Decay	1.0038 ± 0.0005	1.0038 ± 0.0005
K^+- Decay Normalization	1.164 ± 0.033	1.108 ± 0.026
Geometrical Acceptance	5.464 ± 0.318	5.464 ± 0.318
Mass Cut	1.075 ± 0.020	1.138 ± 0.025
Total	11.735 ± 0.839	11.489 ± 0.808
Finite Width	1.087 ± 0.020	1.087 ± 0.020
σ (μb/event)	9.718 ± 1.084	49.056 ± 5.456

TABLE IVc

Correction Factors for the Process
$K^+ A \rightarrow A K^+ \pi^0$

Correction for \ Target	CU	PB
Counter Vetoes	1.373 ± 0.027	1.358 ± 0.025
Beam Absorption at Target	1.0163 ± 0.0030	1.0027 ± 0.0005
K^+ Absorption at Target	1.0163 ± 0.0030	1.0027 ± 0.0005
π^0 Absorption at Target	1.3815 ± 0.0027	1.1776 ± 0.0030
K^+ Absorption at Spectrometer	1.0220 ± 0.0005	1.0220 ± 0.0005
π^0 Absorption at Spectrometer	1.1403 ± 0.0028	1.1403 ± 0.0028
S-Counter Threshold	1.0060 ± 0.0006	1.0060 ± 0.0006
3-Photon	1.022 ± 0.005	1.022 ± 0.005
K^+ Decay	1.0038 ± 0.0005	1.0038 ± 0.0005
π^0 Dalitz Decay	1.0115 ± 0.0005	1.0115 ± 0.0005
K^+ Decay Normalization	1.036 ± 0.020	1.051 ± 0.021
Geometrical Acceptance	3.289 ± 0.164	3.289 ± 0.164
Mass Cut	1.050 ± 0.010	1.050 ± 0.010
Total	8.527 ± 0.499	7.100 ± 0.416
Finite Width	1.064 ± 0.015	1.064 ± 0.015
σ (μb/event)	1.845 ± 0.097	7.490 ± 0.348

TABLE IVd

Correction Factors for the Process
$K^+ A \rightarrow A K_s^0 \pi^+$

Correction for \ Target	CU	PB
Counter Vetoes	1.373 ± 0.027	1.358 ± 0.025
Beam Absorption at Target	1.0163 ± 0.0030	1.0027 ± 0.0005
π^+ Absorption at Target	1.0176 ± 0.0030	1.0028 ± 0.0005
K_s^0 Absorption at Target	1.0163 ± 0.0030	1.0027 ± 0.0004
3π Absorption at Spectrometer	1.0756 ± 0.0015	1.0756 ± 0.0015
S-Counter Threshold	1.0984 ± 0.0108	1.0984 ± 0.0108
3π Decay	1.0105 ± 0.0010	1.0105 ± 0.0010
K^+- Decay Normalization	1.164 ± 0.033	1.108 ± 0.026
Geometrical Acceptance	9.124 ± 0.456	9.124 ± 0.456
Mass Cut	1.050 ± 0.010	1.050 ± 0.010
Total	19.219 ± 1.148	17.351 ± 1.015
Finite Width	1.064 ± 0.015	1.064 ± 0.015
σ (μb/event)	4.825 ± 0.227	20.698 ± 0.934

We have shown the mass intervals over which the geometrical acceptances were calculated in Figures 53 - 57. The corrections for the events outside of these limits, i.e the mass cut corrections, were estimated from these acceptance corrected mass spectra.

An additional correction is needed in calculating the radiative decay widths. This is because Equation (4) (and also Equation (7)) in Chapter I is obtained by assuming a narrow width resonance that can be approximated by a δ -function in mass[40]. This is not fully adequate for the line shapes of the A_2^+ and $K^{*+}(1430)$ mesons. Therefore, we corrected the values of the radiative decay width for the assumed narrow width approximation. This was done by inserting into Equation (16) the parametrization of Equation (19) and (20), and integrating numerically over the mass cut range of a particular reaction. These "finite width" correction values are also shown in Tables IVa-d.

The t - distributions of Reactions (12) - (15) are shown in Figures 58 - 61 for the lead and the copper targets. The cuts on total energy, interaction vertex, two photon mass and K_S^0 mass applied to the data are described in Sections A and B. The sharp forward peaks, increasing roughly as Z^2 for different targets, are seen clearly as expected. The long tail at larger t values are indication to the presence

of strong coherent production of the A_2^+ and $K^{*+}(1430)$ mesons.

We fit these distributions to Equation (7) described in Chapter I.D. The t-resolution of the spectrometer had to be taken into account. We assumed that the observed cross section, $d\sigma/dt$, is a convolution of the true production cross section, $d\sigma/d\tilde{t}$, with a resolution function $R(t,\tilde{t})$:

$$\frac{d\sigma}{dt} = \int d\tilde{t}\, R(t,\tilde{t})\, \frac{d\sigma}{d\tilde{t}}$$

and that this resolution function can be expressed as a two dimensional Gaussian distribution in transverse momentum:

$$R(t,\tilde{t}) = \frac{1}{2\pi\Delta^2} \exp\left[-\frac{|\tilde{\vec{q}}_T - \vec{q}_T|^2}{2\Delta^2}\right]$$

In this expression, $\tilde{\vec{q}}_T$ and $\vec{q}_T$ are the exact and the resolution smeared two dimensional transverse momenta, respectively. Δ is the standard deviation of the Gaussian distribution. Its value for any particular target and reaction was determined from the t-distribution of the corresponding K^+ decay data (see Chapter IV.B for all the values).

The t-dependent factors $f_c(t)$ and $f_s(t)$ were then

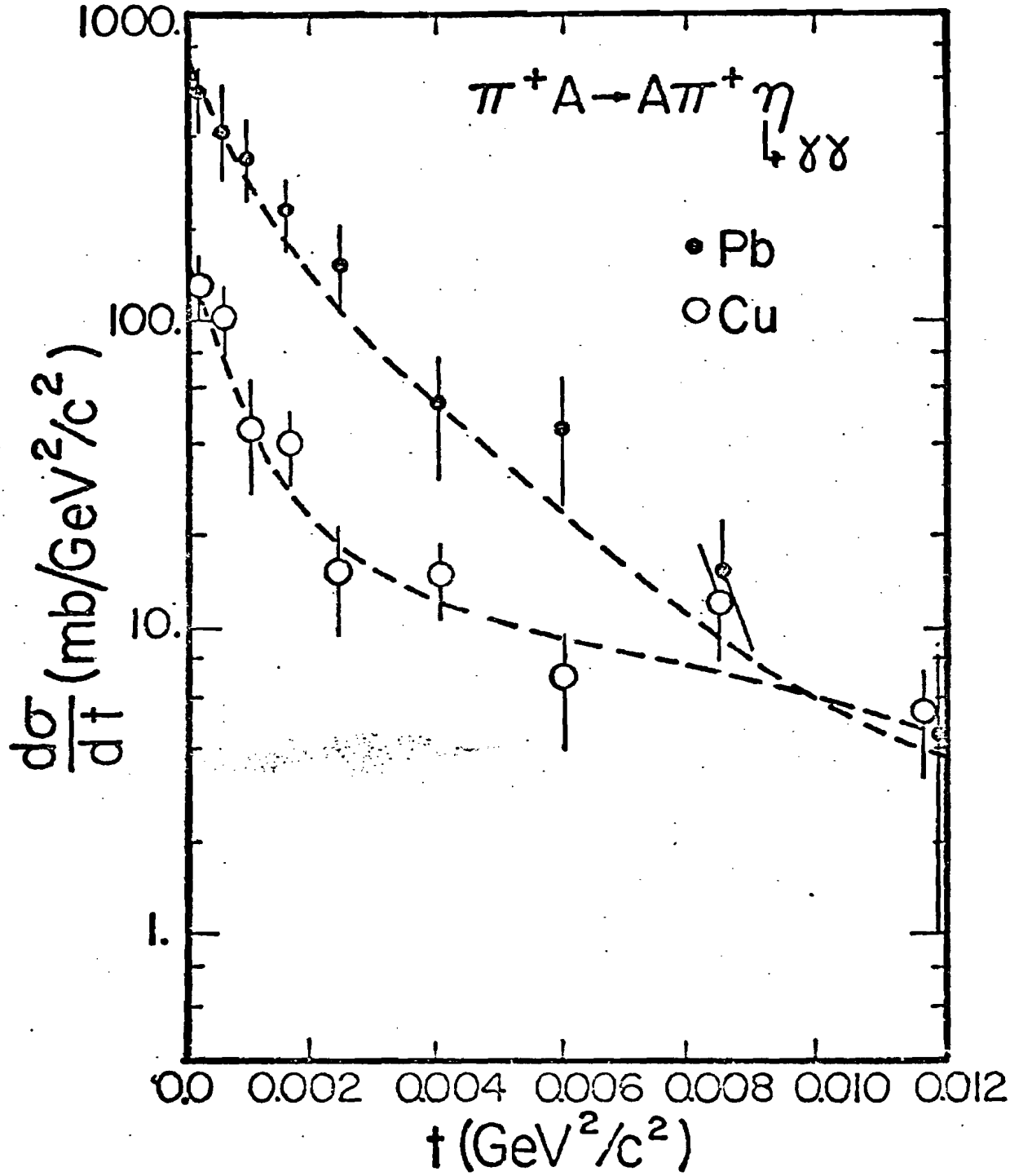
$\pi^+ A \to A \pi^+ \eta$
$\hookrightarrow \gamma\gamma$
• Pb
○ Cu
1000.
100.
10.
1.
$\frac{d\sigma}{dt}$ (mb/GeV^2/c^2)
0.0
0.002
0.004
0.006
0.008
0.010
0.012
t (GeV^2/c^2)

Figure 58

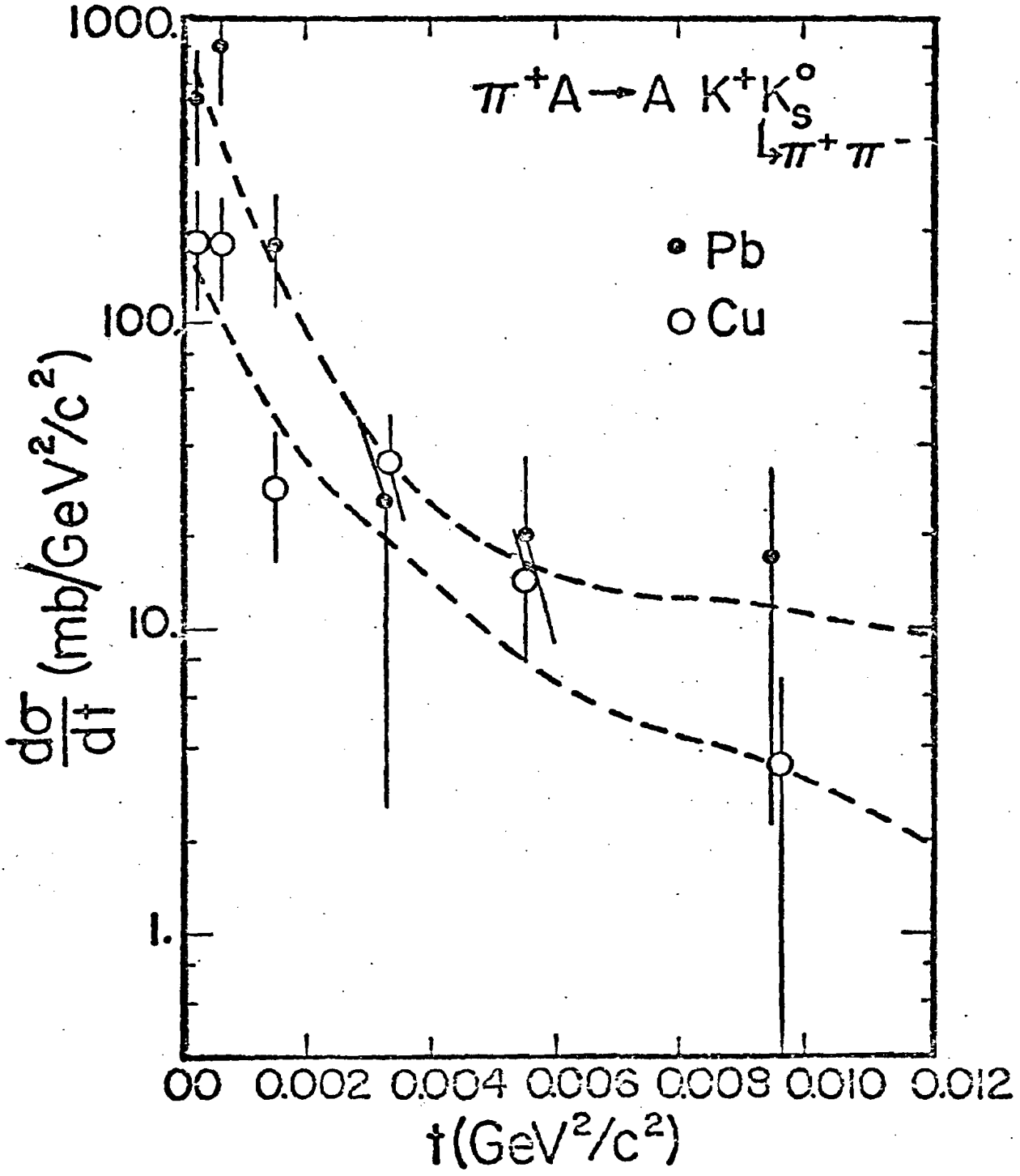
$\pi^+ A \rightarrow A\ K^+ K^0_S$
$\hookrightarrow \pi^+ \pi^-$
Pb
Cu
1000.
100.
10.
1.
$\frac{d\sigma}{dt}$ (mb/GeV^2/c^2)
00
0.002
0.004
0.006
0.008
0.010
0.012
t(GeV^2/c^2)

Figure 59

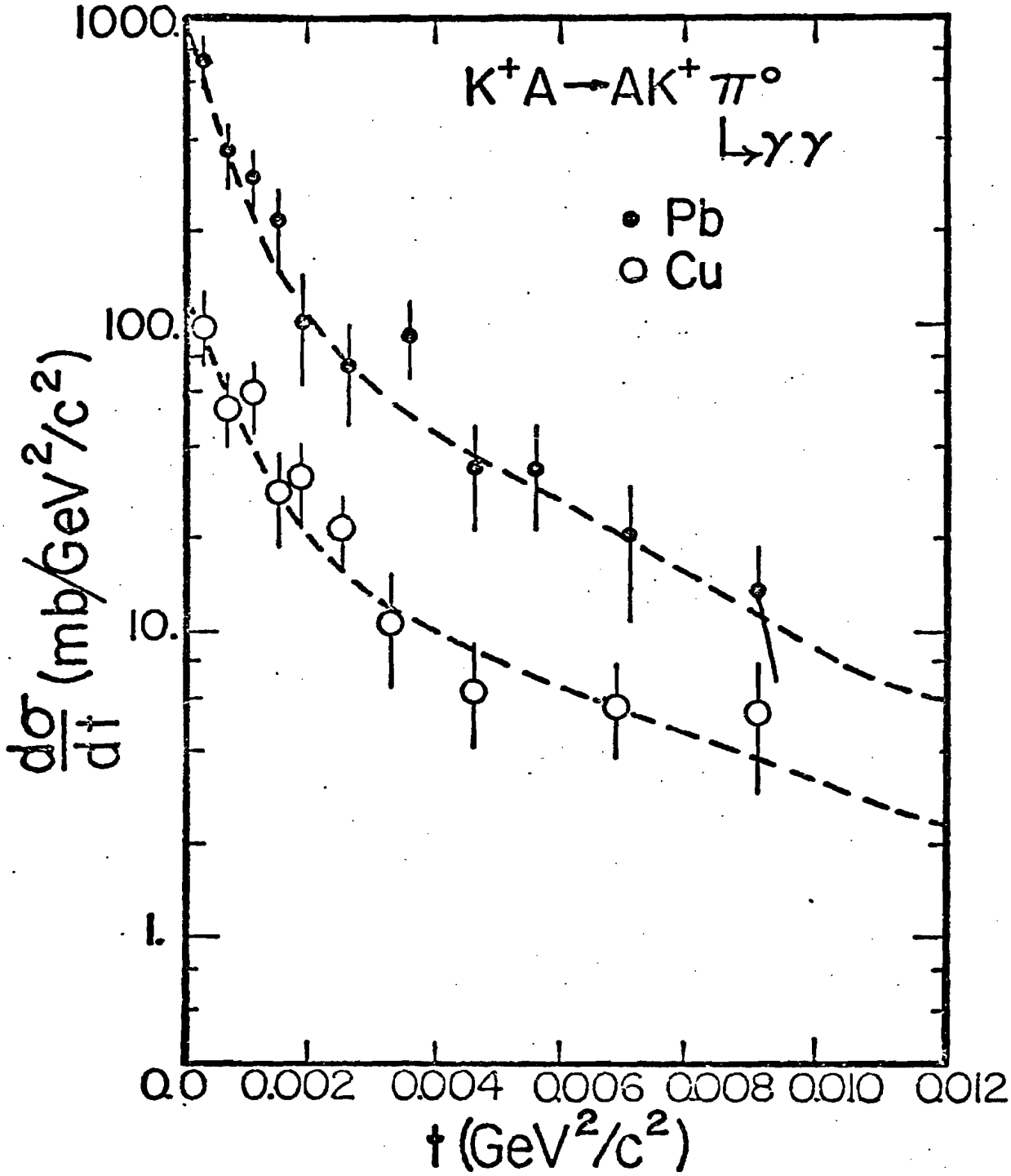
1000.
100.
10.
1.
0.0
0.002
0.004
0.006
0.008
0.010
0.012
$K^+A \to AK^+\pi^0$
$\hookrightarrow \gamma\gamma$
Pb
Cu
$\frac{d\sigma}{dt}$ (mb/GeV^2/c^2)
t (GeV^2/c^2)

Figure 60

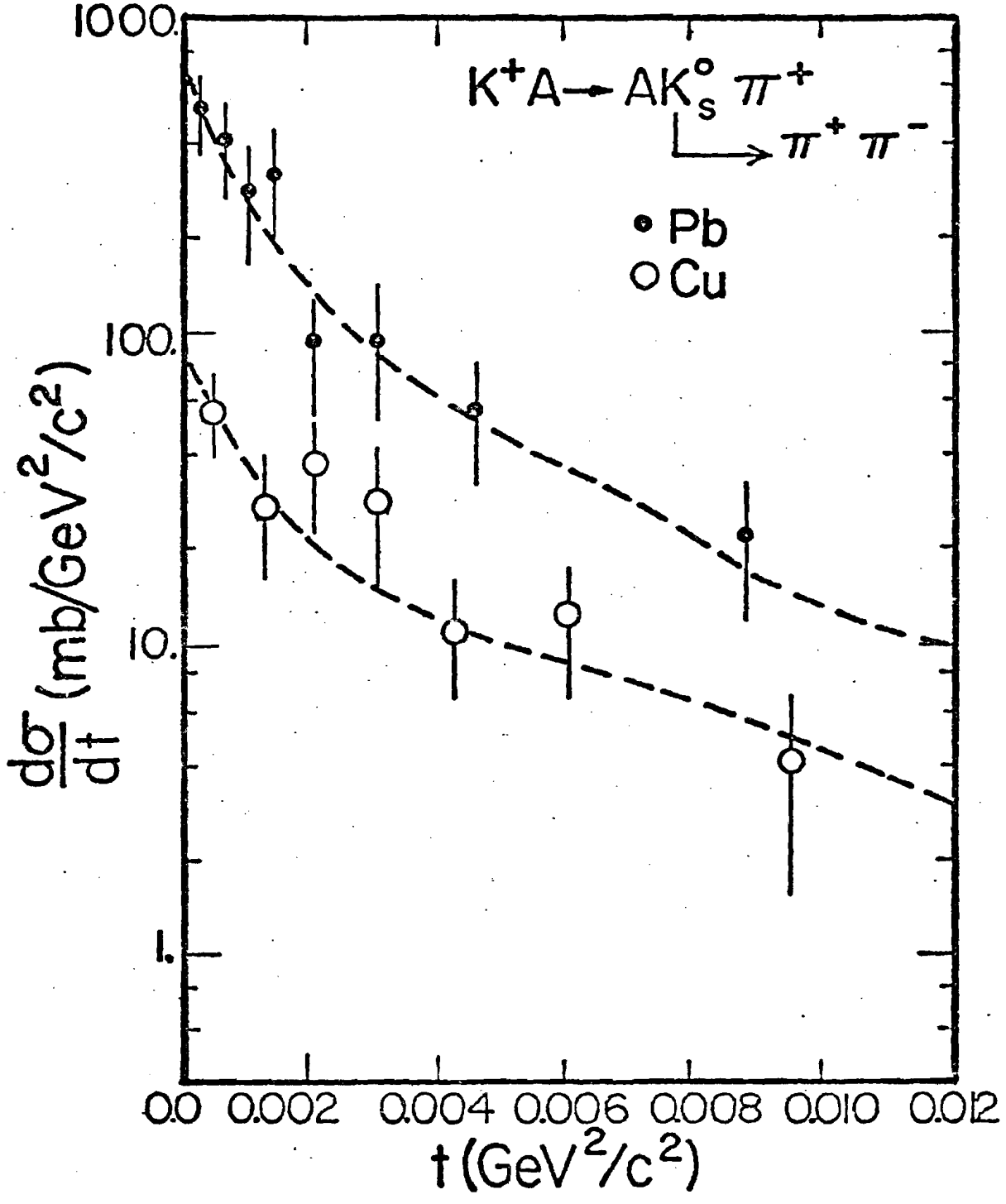
1000.
100.
10.
1.
$K^+A \rightarrow AK^0_s \pi^+$
$\rightarrow \pi^+ \pi^-$
• Pb
○ Cu
$\frac{d\sigma}{dt}$ (mb/GeV^2/c^2)
0.0
0.002
0.004
0.006
0.008
0.010
0.012
t (GeV^2/c^2)

Figure 61

TABLE Va
Results of Parameterization of A_2^+ Data

Reaction Type	Target	t-Range $(Gev/c)^2$	Γ (Kev)	$C_s \left[\frac{mb}{Gev^4}\right]$	ϕ (Degree)	χ^2/dof
a) $\pi^+A \to A\pi^+\eta$	Cu	0.010	286 ± 52	3.1 ± 0.7	109 ± 19	4.3/6
b) $\pi^+A \to AK^+K_s^0$	Cu	0.008	355 ± 166	0.5 ± 0.8	-29±103	3.4/2
c) $\pi^+A \to AK^+K_s^0$	Cu	0.008	442 ± 187	0.5 ± 1.3	-63±166	2.2/2
d) $\pi^+A \to A\pi^+\eta$	Pb	0.010	164 ± 67	3.4 ± 1.5	-15 ± 77	2.1/6
e) $\pi^+A \to AK^+K_s^0$	Pb	0.009	247 ± 77	1.5 ± 2.4	-140±40	2.6/2
f) $\pi^+A \to AK^+K_s^0$	Pb	0.009	321 ± 107	5.1 ± 3.0	143±33	4.3/2
Global Fit	Cu+Pb	0.010	246 ± 35	1.9 ± 0.5	-78 ± 21	27/28

a) 71 events in the specified t-range
b) 27 events in the specified t-range
c) Second peak included, 37 events in the specified t-range
d) 73 events in the specified t-range
e) 18 events in the specified t-range
f) Second peak included, 25 events in the specified t-range

TABLE Vb
Results of Parameterization of $K^{*+}(1430)$ Data

Reaction Type	Target	t-Range $(Gev/c)^2$	Γ (Kev)	$C_s \left[\frac{mb}{Gev^4}\right]$	ϕ (Degree)	χ^2/dof
a) $K^+A \to AK^+\pi^0$	Cu	0.010	210 ± 39	0.9 ± 0.7	63 ± 57	5.7/6
b) $K^+A \to AK_s^0\pi^+$	Cu	0.010	146 ± 36	1.1 ±0.4	7 ± 79	3.5/3
c) $K^+A \to AK^+\pi^0$	Pb	0.010	255 ± 40	1.6 ± 0.6	-79 ± 23	4.6/7
d) $K^+A \to AK_s^0\pi^+$	Pb	0.010	196 ± 64	2.2 ± 1.0	-58 ± 50	2.5/4
Global Fit	Cu+Pb	0.010	227 ± 25	1.1 ± 0.3	-68 ± 20	23/32

a) 106 events in the specified t-range
b) 40 events in the specified t-range
c) 149 events in the specified t-range
d) 54 events in the specified t-range

calculated and the three parameters, $\Gamma(a^* \rightarrow a\gamma)$, C_s and ϕ, were varied to achieve the best fit of Equation (7) to the data. The results are summarized in Table V. The uncertainties in these values are the diagonal errors calculated by the fitting program as the change in one parameter which increases the χ^2 by one; during this change the other parameters are reoptimized.

The $K^{*+}(1430)$ radiative decay width values obtained from its decays into $K^+\pi^0$ and $K_s^0\pi^+$ are consistent with each other. Among the A_2^+ results, the $\pi^+Pb \rightarrow Pb\eta\pi^+$ $(\eta \rightarrow \gamma\gamma)$ decay width is low compared to the others. The fit to the data from this reaction also indicates a higher strong production background and this causes the fit to yield a low Coulomb contribution. If we fix the parameter C_s to a value of 1.5 mb/Gev^4, the fitted dacay width becomes 220 Kev with a χ^2 of 5.2/6 (dof)$^{-1}$. This discrepancy could be explained by the statistical fluctuations in one or more points in the t-distribution (Figure 58) of this reaction.

In the analysis of the data on Reaction (13) the mass cut was chosen narrower to exclude the peak with higher mass. If the lead and the copper data are combined, this peak contains 30 events with $t \leqslant 0.010$ (Gev/c)^2 and 22 of these events have $t \leqslant 0.003$ (Gev/c)^2. This is an indication to the Coulomb production of the events in this high mass

peak. We also fitted the data including this second peak. The resultant radiative decay width values $\Gamma(A_2^+ \to \pi^+\gamma)$ are also listed in Table Va and are about 30% higher.

The data on Reaction (12b) were not sufficient to yield a value for the decay width $\Gamma(A_2^+ \to \pi^+\gamma)$, but the upper limit we could get was consistent with the values listed in Table V.

E. CONCLUSIONS

We have presented the results of the analysis on the first Primakoff productions of the A_2^+ and $K^{*+}(1430)$ mesons. The obtained widths are in both cases slightly lower than the theoretical predictions given in Reference 6, but within experimental errors and theoretical uncertainties the deviation is not substantial.

To check the stability of the solutions, we varied the ranges of t used in the fits. We also included a background term of the form $B_0 \exp(-B_1 t)$, where B_0 and B_1 are constants. In all cases, the fluctuations in the fitting results, with acceptable χ^2 values, were within the statistical errors. Fits were performed using different t-resolution (Δ) values. A 20% change in Δ produced a ~5% change in the fitted values of the radiative decay widths. In the global

fits, we assumed that C_S and ϕ were independent of target material.

We quote a value, $\Gamma(A_2^+ \to \pi^+\gamma) = 246 +/- 50$ Kev, for the radiative decay width of A_2^+, and a value, $\Gamma(K^{*+}(1430) \to K^+\gamma) = 227 +/- 45$ Kev, for the radiative decay width of $K^{*+}(1430)$. These values are obtained from the global fits and are similar to the weighted average of all the fits on individual modes and targets. The uncertainties include a ~10% error due to t resolution and a ~10% error estimated for the overall normalization which can be caused by some reaction independent effects. The radiative decay width of A_2^+ that we quote is somewhat lower than the results of previous measurements. For instance, an application of one pion-exchange model to a photoproduction of A_2 in $\pi^{\mp}\eta$ decay mode yields a value $\Gamma(A_2 \to \pi\gamma) = 450 +/- 110$ Kev [41]. The values for C_S and ϕ are not well determined but are consistent with the the expectations based on strong production experiments[42]. Varying ϕ between -90° and 90° keeps the radiative decay width values within their uncertainty ranges quoted above.

Although the evidence discussed earlier suggests that the events in the high mass peak are not just a result of a statistical fluctuation, the low statistics limits our ability to claim anything conclusive. Assuming that these

events belong to a state with a mass M =1440 Mev/c^2, we can quote a value of about 30 Kev for (2J+1)x(Radiative decay width)xBranching Ratio to K^+K^0 of this state if we neglect the strong production of this state.

REFERENCES

1. M. Gell-Mann, Phys. Lett. 8, 214 (1964), G.Zweig, CERN Rep. 8419/TH (1964); G. Zweig, Symmetries in Elementary Particle Physics, ed A. Zichichi, (Academic Press, New York) p. 192 (1965).

2. The SU(3) predictions of these decays were investigated by S. Okubo, Phys. Lett. 4, 14 (1963); S. L. Glashow, Phys. Rew. Lett. 11, 48 (1963); K. Tanaka, Phys. Rev. 133, B1509 (1964).

3. C. Becchi and G. Morpurgo, Phys Rev. 140B, 687 (1965); Y. Anisovitch et al, Phys. Lett. 16, 194 (1965); W. Thirring, Phys. Lett. 16, 335 (1965); L. Soloviev, Phys. Lett. 16, 345 (1965), R. VanRoyen and V. F. Weisskopf, Nuovo Cimento A50, 617 (1967).

4. For comparison of theory and experiment see P. J. O'Donnel, Can. J. Phys. 55, 1301 (1977); A. N. Kamal, Phys. Rev. D18, 3512 (1978); B. J. Edwards and A. N. Kamal, SLAC-PUB-2303 (1979). For a review of experimental situation see E. H. Thorndike, V International Conference on Experimental Meson Spectroscopy, E. Von Goeler and R. Weinstein Eds., p.345 (1977).

5. D. Berg et al, Phys. Rev. Lett. 44, 706 (1980); D. Berg et al, Phys. Lett. 98B, 119 (1981); T. Ohshima, Phys. Rev. D22, 707 (1980).

6. J. Babcock and J. Rosner, Phys. Rev. D14, 1286 (1976); J. Babcock and J. Rosner, Preprint (1979).

7. J. Rosner, Phys. Reports 11C, 189 (1974), First paper in Reference 6.

8. M. A. B. Beg, P. C. DeCelles and R. B. Marr, Phys. Rev. 124, 622 (1961); S. M. Berman and S. D. Drell, Phys. Rev. 133, B791 (1964); A. Halprin, C. M. Andersen and H. Primakoff, Phys. Rev. 152, 1295 (1966); Y. Nagashima and J. Rosen, University of Rochester Report No. UR-875-295, 1969 (unpublished); N. Jurisic and L. Stodolsky, Phys. Rev. D3, 724 (1971); M. Gourdin, Nucl. Phys. B32, 415 (1971); G. Berlad et al, Ann. of Phys. 75, 461 (1973).

9. For detailed discussion of coherent processes, see H. H. Bingham, in Proc. Topical Seminar on Interactions of Elementary Particles with Nuclei, Trieste, 1970 p.37 (INFN, Trieste, 1971); T. Ferbel, Lecture presented at the First Workshop on

Ultra-Relativistic Nuclear Collisions, LBL (1979), University of Rochester Report UR-704.

10. The low-lying excited state can be a collective state of vibrational of rotational nucleon states in a heavy nucleus. Therefore, not all nucleons contribute equally. If one adds many such states they cancel each other due to their random phases.

11. A. S. Goldhaber and M. Goldhaber, Preludes in Theoretical Physics (North Holland Publishing Company, Amsterdam, 1966), A. de Shalit, A. H. Feshbach and L. Van Hove, eds.

12. A. Halprin, C. M. Andersen and H. Primakoff in Reference 8.

13. H. Primakoff, Phys. Rev. 81, 899 (1951).

14. See, for example, M. Gourdin in Reference 8 and L. Strawczynski, PhD Thesis, University Of Rochester Report UR-457 (1974).

15. D. R. O. Morrison, Phys. Lett. 22, 528 (1966); C. B. Chiu, Annual Review of Nuclear Science 22, p.255 (1972), E. Segre, ed. (Annual Reviews Inc. Palo Alto, California).

16. L. Stodolsky, Phys. Rev. 144, 1145 (1966).

17. A. N. Kamal and G. L. Kane, Phys. Rev. Lett. 43, 551 (1979).

18. K. S. Kolbig and B. Margolis, Nucl. Phys. B6, 85 (1968); G. Fäldt et al, Nucl. Phys. B41, 125 (1972); G. Fäldt, Nucl. Phys. B43, 591 (1972); C. Bemporad et al, Nucl. Phys. B51, 1 (1973). See also L. Strawczynski in Reference 14.

19. We have used the values x=0.053 for π^+-nucleon and x=0.071 for K^+-nucleon scattering given by L. A. Fajardo et al, FERMILAB-PUB-80/27-EXP 7120.069 (1980). The π^+-nucleon cross section, σ =24.5 mb, and K^+-nucleon cross section, σ =20.0, were obtained from the Review of Particle Properties, Rev. Mod. Phys. 52, No 2, Part II (April 1980).

20. B. Hahn, D. G. Ravenhall and R.Hofstadter, Phys. Rev. 101, 1131 (1956).

22. A detailed source of information on the M-1 beam line is provided in the M-1 Users' Guide, S. Ecklund, Fermilab Report TM-743.2833, May 1977.

22. A. Jonckheere et al, Nucl. Inst and Meth. 180, 25 (1981).

23. The K1 and K2 counters were designed by T. F. Kycia. A description of their operation may be found in an appendix of Reference 21.

24. This counter, designed by S. M. Pruss, is similar to a prototype counter described in D. D. Yovanovitch et al, ANL Report ANL/HEP-7104 (1972).

25. For construction and operation of the drift chambers, see T. C. Jensen, PhD Thesis, University of Rochester report UR-747 (1980).

26. W. J. Willis and V. Radeka, Nucl. Inst. and Meth. 120, 221 (1974); G. Knies and D. Neuffer, Nucl. Inst. and Meth. 120, 1, (1974)); J. Engler et al, Nucl. Inst. and Meth. 120, 157 (1974); D. Hitlin et al., Nucl. Inst. and Meth. 137, 225 (1976); C. Cerri and F. Sergiampietri, Nucl. Inst. and Meth. 141, 207 (1977); J. H. Cobb et al, Nucl. Inst. and Meth. 158, 93 (1979).

27. D. W. Swan, Proc. Phys. Soc. 83, 659 (1964); J. Engler et al, in Reference 26; W. Hofmann et al, Nucl. Inst. and Meth. 135, 151 (1976).

28. T. F. Droege, F. Lobkowicz and Y. Fukushima, Fermilab Report TM-746 2500.000, (October 1977).

29. C. R. Kerns, Fermilab Report TM-819 2510.000, (October 1978).

30. A. E. Brenner, T. F. Droege and R. G. Martin, Fermilab Report TM-537 2340.000 (December 1974).

31. For a more detailed description, see C. Chandlee, PhD Thesis, University of Rochester 1981, (unpublished).

32. Yung-Su Tsai, Rev. of Mod. Phys. 46, 815 (1974).

33. A. S. Carroll et al, Phys. Lett. 80B, 319 (1979); J. C. Allaby et al, Sov. Journal of Nucl. Phys. 12, 295 (1971).

34. A. S. Carroll et al, Phys. Rev. Lett. 33, 962 (1974).

35. W. Beusch et al, Phys. Lett. 25B, 357 (1967); J. Barlow et al, Nuova Cimento 50A, 701 (1967); K. J. Foley et al, Phys. Rev. Lett. 26, 413 (1971);

36. See, for example, G. Berlad et al in Reference 8.

37. J. D. Jackson, Nuovo Cimento 34, 1644 (1964).

38. W. Beusch et al, and K. J. Foley et al in Reference 35; V. Chabaud et al, Nucl. Phys. B145, 349 (1978); A. D. Martin et al, Nucl. Phys. B134, 392 (1978).

39. F. James and M. Ross, MINUIT, CERN Computer 7600 Interim Program Library (1971).

40. See, for example, T. Ohshima, "Coulomb Cross Section and Resonance Width", University of Rochester Internal Report.

41. E. N. May et al, Phys. Rev. D16, 1983 (1977); Y. Eisenberg et al, Phys. Rev. D5, 15 (1972).

42. In addition to Reference 38 see, F. Schweingruber et al, Phys. Rev. 166, 1317 (1968); V. Gordon Lind et al, Nucl. Phys. B14, 1 (1969); K. W. J. Barnham et al, Nucl. Phys. B28, 171 (1971); M. Aguilar-Benitez, R. L. Eisner and J. B. Kinson, Phys. Rev. D4, 2583 (1971); B. Hyams et al, Nucl. Phys. B146, 303 (1978); V. Chabaud et al, CERN Report CERN-EP/79-159 (December 1979).